QUANTITATIVE OPTICAL STUDIES OF OXIDATIVE STRESS IN RODENT MODELS OF EYE AND LUNG INJURIES

by

Zahra Ghanian

A Dissertation Submitted in

Partial Fulfillment of the

Requirements for the Degree of

Doctor of Philosophy

in Engineering

at

The University of Wisconsin-Milwaukee

December 2016

ABSTRACT

QUANTITATIVE OPTICAL STUDIES OF OXIDATIVE STRESS
IN RODENT MODELS OF EYE AND LUNG INJURIES

by

Zahra Ghanian

The University of Wisconsin-Milwaukee, 2016
Under the Supervision of Professor Mahsa Ranji

Optical imaging techniques have emerged as essential tools for reliable assessment of organ structure, biochemistry, and metabolic function. The recognition of metabolic markers for disease diagnosis has rekindled significant interest in the development of optical methods to measure the metabolism of the organ.

The objective of my research was to employ optical imaging tools and to implement signal and image processing techniques capable of quantifying cellular metabolism for the diagnosis of diseases in human organs such as eyes and lungs. To accomplish this goal, three different tools, cryoimager, fluorescent microscope, and optical coherence tomography system were utilized to study the physiological metabolic markers and early structural changes due to injury *in vitro*, *ex vivo,* and at cryogenic temperatures.

Cryogenic studies of eye injuries in animal models were performed using a fluorescence cryoimager to monitor two endogenous mitochondrial fluorophores, NADH (nicotinamide adenine dinucleotide) and FAD (flavin adenine dinucleotide). The mitochondrial redox ratio (NADH/ FAD), which is correlated with oxidative stress level, is an optical biomarker. The spatial distribution of mitochondrial redox ratio in injured eyes with different durations of the disease was delineated. This spatiotemporal information was helpful to investigate the heterogeneity of the ocular oxidative stress in the eyes during diseases and its association with retinopathy. To study

the metabolism of the eye tissue, the retinal layer was targeted, which required high resolution imaging of the eye as well as developing a segmentation algorithm to quantitatively monitor and measure the metabolic redox state of the retina. To achieve a high signal to noise ratio in fluorescence image acquisition, the imaging was performed at cryogenic temperatures, which increased the quantum yield of the intrinsic fluorophores.

Microscopy studies of cells were accomplished by using an inverted fluorescence microscope. Fixed slides of the retina tissue as well as exogenous fluorophores in live lung cells were imaged using fluorescent and time-lapse microscopy. Image processing techniques were developed to quantify subtle changes in the morphological parameters of the retinal vasculature network for the early detection of the injury. This implemented image cytometry tool was capable of segmenting vascular cells, and calculating vasculature features including: area, caliber, branch points, fractal dimension, and acellular capillaries, and classifying the healthy and injured retinas. Using time-lapse microscopy, the dynamics of cellular ROS (Reactive Oxygen Species) concentration was quantified and modeled in ROS-mediated lung injuries. A new methodology and an experimental protocol were designed to quantify changes of oxidative stress in different stress conditions and to localize the site of ROS in an uncoupled state of pulmonary artery endothelial cells (PAECs).

Ex vivo studies of lung were conducted using a spectral-domain optical coherence tomography (SD-OCT) system and 3D scanned images of the lung were acquired. An image segmentation algorithm was developed to study the dynamics of structural changes in the lung alveoli in real time. Quantifying the structural dynamics provided information to diagnose pulmonary diseases and to evaluate the severity of the lung injury. The implemented software was

able to quantify and present the changes in alveoli compliance in lung injury models, including edema.

In conclusion, optical instrumentation, combined with signal and image processing techniques, provides quantitative physiological and structural information reflecting disease progression due to oxidative stress. This tool provides a unique capability to identify early points of intervention, which play a vital role in the early detection of eye and lung injuries. The future goal of this research is to translate optical imaging to clinical settings, and to transfer the instruments developed for animal models to the bedside for patient diagnosis.

© Copyright by Zahra Ghanian, 2016
All Rights Reserved

To Dad and Mom, for their endless love

TABLE OF CONTENTS

List of figures ..... **ix**

List of tables ..... **xii**

List of abbreviations ..... **xiii**

Acknowledgments ..... **xv**

1 Introduction and Background **2**

1.1 Author Major Contributions 3

1.2 Biological background 11
1.2.1 Cell physiology and metabolism 11
1.2.2 Oxidative stress 13

1.3 Fluorescence 14
1.3.1 Principles of fluorescence 14
1.3.2 Intrinsic mitochondrial fluorophores 17
1.3.3 Florescence imaging techniques 18

1.4 Rodent injury models and diseases 20

2 Optical cryoimaging of oxidative stress in eye diseases **26**

2.1 Tissue Preparation 27
2.1.1 Akita/+, diabetic retinopathy, mice eyes 28
2.1.2 Retinitis pigmentosa, rat eyes 28
2.1.3 Endoglin transgenic mice eyes, HHT-1 29
2.1.4 Oxygen induced ischemic retinopathy, OIR, mice eyes 29
2.1.5 Freezing Protocol and Embedding 29

2.2 Imaging and Image Processing 31
2.2.1 Optical cryoimaging system 31
2.2.2 Version two of the cryoimager for eye imaging 33
2.2.3 Image Processing 37

2.3 Results 41

2.4 Discussion and conclusion 48

3 Microscopy studies of retina and lung cells **55**

3.1 Microscopy of retinal injuries 56
3.1.1 Injury model 58
3.1.2 Microscope slide preparation 59
3.1.3 Fluorescence microscopy 59
3.1.4 Image processing 60
3.1.5 Injury classification 67

3.1.6 Results 68
3.1.7 Discussion and conclusion on the retina study 73
3.2 Time lapse microscopy of live lung cells *in vitro* 78
3.2.1 Live cell preparation 80
3.2.2 Time-lapse microscopy 81
3.2.3 Experimental procedure 84
3.2.4 Image and signal processing 85
3.2.5 Quantification of superoxide dynamics 88
3.2.6 Statistical analysis 89
3.2.7 Results 89
3.2.8 Discussion and conclusion on lung cells *in vitro* studies 101
3.3 Summary 110
4. *Ex vivo* studies of lung in animal model 112
4.1. Tissue Preparation 113
4.1.1. Rat lungs 113
4.1.2. Pulmonary alveolar edema 114
4.2. Pulmonary compliance experiment 114
4.3. OCT instrument 115
4.4. Imaging and image processing 117
4.4.1. Imaging and image acquisition 117
4.4.2. Image processing 118
4.5. Results 125
4.5.1. Alveolar structure segmentation 125
4.5.2. Alveolar compliance results 126
4.6. Conclusion 128
5. Conclusion and future direction 131
5.1 Cryoimaging 131
5.2 Image cytometry 132
5.3 *In vitro* time lapse microscopy 133
5.4 *Ex vivo* OCT imaging 134
6. References 136
7. Appendix: Curriculum Vitae 163

LIST OF FIGURES

Figure 1-1: Cell, mitochondrion and their organelles 12

Figure 1-2: Simplified block diagram of the electron transport chain 13

Figure 1-3: Jablonski Diagram of Fluorescence 15

Figure 1-4: Stokes shift 16

Figure 1-5: Excitation and emission spectra of NADH and FAD. 17

Figure 2-1: Schematic of cryoimager 32

Figure 2-2: Version two of the cryoimager 34

Figure 2-3: Anatomy and a 2D cross section image of a rat or mouse eye 37

Figure 2-4: A schematic illustration of the image processing steps to obtain the 3D representation and histogram of the eye redox from the input fluorescent images 38

Figure 2-5: Images of FAD, NADH, and RR (FAD Redox; NADH / FAD) for one representative eye (10 months, Eng+/-) 40

Figure 2-6*:* Increased oxidative stress in diabetic eyes from 3 weeks (non-diabetic) and 6 months (diabetic) old Akita/+ mice 42

Figure 2-7: Representative max projected NADH, FAD and RR images for eyes from normal and transgenic groups 43

Figure 2-8: Representative histogram and bar graph plot for eyes from P23H transgenic retina vs. SD Normal retina 44

Figure 2-9: Representative 3-D reconstructions of an eye from each of the three age groups (P21, 6W, 10M) and their related histograms 46

Figure 2-10: Representative 3-D reconstructions of eyes from P17 Eng+/+ mice and P17 Eng+/- mice during OIR and related histogram 47

Figure 2-11: Bar graph plot comparing the mean values of the histograms of 3D rendered images from Eng +/- eyes and their respective controls in three different ages in normal ambient and OIR conditions 47

Figure 3-1: High resolution microscopy images of a typical mouse retinal vasculature trypsin digest 61

Figure 3-2: Cell segmentation procedure 63

Figure 3-3: Acellular capillary detection 65

Figure 3-4: Comparing five unique features in a diabetic retina versus a normal retina from 11 month-old mice 69

Figure 3-5: Results of the classification using SVM method in retinas from 73

Figure 3-6: Cell images in bright-field, blue (Hoechst) fluorescence, green (Mito-tracker green) and red (Mito-SOX red) fluorescence 82

Figure 3-7: A schematic illustration of the methodology used to obtain the MitoSOX fluorescent intensity profiles of the cells from the input fluorescent images 86

Figure 3-8: Representative raw frames from image stack of time-lapse microscopy showing dynamic $O_2^{\bullet-}$ production in 3 experiments …..... 91

Figure 3-9: Dynamic fluorescence intensity profiles over time of cells in the presence or absence of the uncoupler (PCP) or the mitochondrial ETC complex inhibitors (ROT, AA, or KCN) 93

Figure 3-10: Summary bar graphs show the slope of the fluorescence intensity profiles right after the agent administration..... 94

Figure 3-11: Mean ± SE of fluorescent intensity profiles of $O_2^{\bullet-}$ production over time in PAECs treated with PCP in addition with one of the ETC inhibitors 95

Figure 3-12: Representative fluorescent intensity profiles in untreated cells (control) and PCP treated cells in the absence and presence of the superoxide scavenger MitoTempol over time... 97

Figure 3-13: Representative dynamic fluorescence intensity profiles over time in the untreated cells and the treated cells treated with Tempol and MitoTempol..... 98

Figure 3-14: Bar graph plot showing the means and standard errors of the slope ratio of the red fluorescence intensity profile (t=30 min) for NFL and HTFL groups..... 100

Figure 3-15: Bar graph plot showing the means and standard errors of the slope ratio of the red fluorescence intensity profile at t=30 min for hypoxia and IR groups 101

Figure 4-1: Experimental setup for the compliance experiments..... 114

Figure 4-2: Schematic of the spectral domain OCT 116

Figure 4-3: Images of the scanner head during *ex-vivo* experiments on the normal and edemic lungs attached to the Langendorff perfusion system..... 117

Figure 4-4: Extraction of the alveolar sacs from the raw image produced by the SD-OCT system 118

Figure 4-5: 3D reconstructed image of the lung alveoli 119

Figure 4-6: Flowchart of the alveoli segmentation procedure 120

Figure 4-7: Output of the segmentation algorithm in different stages..... 122

Figure 4-8: (a) Bilevel LOG filter in blue color (b) top view of filter C) two different side views of the implemented filter..... 123

Figure 4-9: Average quality 2D image of lung alveoli at a depth of 75 μm from 450 g five months old rat captured and reconstructed by SD-OCT in the ventilated pressure of 5 torr 125

Figure 4-10: A: Histograms of alveoli diameter (μm) at three pressures: 2.5 torr, 5 torr, 6.5 torr. B: Linear curve fitting of alveoli volume versus pressure 126

Figure 4-11: 2D images of alveoli from *ex vivo* rat lung captured and reconstructed by SD-OCT at a depth of 83 μm and a ventilated representative pressure of 8.1 torr 128

Figure 4-12: Alveolar expiration compliance of edemic and normal rat lungs 128

LIST OF TABLES

Table 2-1: The thickness of different layers in the back of the mouse eye 40

Table 3-1: Accuracy of the cell count and cell type determinations 70

Table 3-2: Performance of the SVM classifier for different groups under study. 72

LIST OF ABBREVIATIONS

3W - 3 Weeks

6W - 6 Weeks

6M - 6 Months

11M - 11 Months

AA - Antimycin A

ADP - Adenosine Diphosphate

ATP - Adenosine Triphosphate

BCL-2 -B Cell Lymphoma Gene

CCD - Charged Coupled Device

DNA - Deoxyribose Nucleic Acid

DMEM- Dulbecco's Modified Eagle's Medium

DR - Diabetic Retinopathy

EC - Endothelial Cell

ETC - Electron Transport Chain

Eng - Endoglin gene

$FADH_2$ - Flavin Adenine Dinucleotide

FOV – Field of View

GUI - Graphical User Interface

HBSS - Hank's Balanced Salt Solution

HHT - Hereditary Hemorrhagic Telangiectasia

H&E - Hematoxylin and Eosin

HTFL - Hypertensive Fetal Lamb

IR - Ischemia Reperfusion

KCN - Potassium Cyanide

LN_2 - Liquid Nitrogen

MTG- Mito-Tracker Green

NADH - Nicotinamide Adenine Dinucleotide

NADPH - Nicotinamide Adenine Dinucleotide Phosphate

NAD(P)H - Combination of NADH and NADPH

NFL - Normotensive Fetal Lamb

OCT - Optical Coherence Tomography

OIR - Oxygen Ischemic Retinopathy

OS - Oxidative Stress

P21 - Postnatal Day 21

PAEC - Pulmonary Artery Endothelial Cell

PBS - Phosphate Buffered Saline

PC - Pericyte

PCP - Pentachlorophenol

PPHN - Persistent Pulmonary Hypertension of Newborn

ROT - Rotenone

ROS - Reactive Oxygen Species

RR - Redox Ratio

SD - Spectral Domain

SD - Sprauge Dawley

ACKNOWLEDGMENTS

I take this opportunity to express my sincere appreciation and gratitude to my advisor, Dr. Mahsa Ranji, for her help and support and opportunities she provided me throughout my doctoral studies. I truly appreciate all she has done for me as a supervisor.

I would like to thank Dr. Pashaei and Dr. Audi for their collaboration in *Ex vivo* studies. Thanks also to the wonderful people of BIST lab, including Farid Atri, without whom data collection would have not been possible.

I acknowledge our other collaborators, Professors Camara and Kondouri from Medical College of Wisconsin, and Professors Sheibani and Sorenson from University of Wisconsin-Madison. The biological aspects of this research would have not been advanced without their insightful comments. I would also like to thank Annie Eis, Nasim Jamali and Maxwell Alexander for their help in cell culture. I acknowledge James Wagner, who recovered my experimental data from a crashed hard drive. I thank all members of the Biophotonics Lab specially Jeff Sugar and Mette La Cour for their help editing my thesis.

I like to thank my dissertation committee, Professor Nasiri, Professor Sheibani, Dr. Sung, and Dr. Hu for agreeing to serve as my committee and for their insightful contributions.

I would like to finally express my deepest gratitude to my husband Saber Shahin for his patience and support, and to my sisters for their encouragement.

Chapter 1

Introduction and Background

1 Introduction and Background

Biophotonics is a relatively new field at the intersection of science and technology that has the potential to revolutionize medicine as we know it. The rapid development of optical imaging technology has yielded powerful tools for the study of disease on all scales, from single cells to tissue materials and whole organs.

Among optical imaging systems, fluorescence imaging techniques provide the capability of monitoring the metabolic health of cells, tissue, and organs. Auto fluorescent mitochondrial proteins, and Reactive Oxygen Species (ROS), are used as indicators for mitochondrial function, and are monitored by applying *in vitro* approaches. Organs can also be monitored in the cryogenic temperature or *ex vivo* as well as *in vivo*. The knowledge of the absorption and fluorescence characteristics of the auto fluorescent proteins within the body and biological samples is key. This knowledge allows us to determine the concentrations of these fluorophores correlated to the mitochondrial redox state and oxidative stress level. Monitoring the metabolic state of cells with low mitochondrial density requires exogenous fluorophores to probe the mitochondrial ROS production rate, which is correlated with oxidative stress. The development of the fluorescent imaging and image processing techniques including cryo fluorescence imaging and fluorescent microscopy to study metabolism in live cells and organs will be described in the following sections.

Optical Coherence Tomography (OCT) is another imaging system that was utilized in this study. This imaging technique has the ability to visualize the tissue without the need to remove or excise portions of a specimen. This technique enables cross-sectional real time imaging of the internal microstructure in biological systems by measuring backscattered light. Utilizing a spectral domain OCT to monitor and study the structural dynamics in organs will be presented. Moreover,

the development of an image processing software to quantify the morphological changes for the diagnosis purposes will be explained.

The overall aim of the research presented here is developing biomedical fluorescence imaging techniques and employing optical imaging instruments to provide critical information about the health of the biological sample. This information bridges molecular structure and physiological function, which is the most important process in understanding, treatment, and prevention of disease.

1.1 Author Major Contributions

My first contribution is the modification and implementation of a cryo fluorescence imager to increase lateral resolution of this optoelectronic device to visualize the morphology and biochemistry of mouse eyes in 3D and to distinguish different structures of eyes. The cryoimager monitors the relative concentration of two intrinsic mitochondrial fluorophores, namely NADH and FAD. To obtain high resolution fluorescence images of the small mouse eye samples, the detection path of the system was modified and the working distance between the sample and lens was decreased to obtain a stronger signal. In addition, a high-resolution zoom lens with less aberration as well as a smaller optical filter wheel was used between the lens and camera to improve the magnification. The new setup was completed by resolving non-homogeneity illumination problem.

The modified cryoimager provided high resolution fluorescence images of 2mm mouse eyes in 3D which enabled me to distinguish between different layers of eye including sclera, choroid, and retina. The thickness of these layers is ranging from 10 microns to 200 microns and can be detected based on the fluorescence intensity levels. I have developed an image processing algorithm which analyzes two *z*-stacks of raw images of eye in both NADH and FAD channels to

evaluate metabolic redox state (correlated with redox ratio, FAD/NADH) in the retina 3D volume quantitatively and statistically.

The new set up of the cryoimager combined with aforementioned image processing tool provide a package to quantitatively measure the metabolic state of the retina in the onset and progression of different diseases in rodent models. Using this package, I have studied a severe vascular dysplasia (HHT-1 or Endoglin+/-) with the aim of investigating spatial and temporal changes of physiological information in the eye due to this disease. I quantitatively evaluated cellular redox state and oxidative stress (OS) in retina at three stages of this disease (3 weeks, 6 weeks and 10 months).

I have also developed and implemented a second-generation cytometry tool based around a first-generation software developed in Biophotonics Lab. Our cytometry GUI is a multi-parameter quantification method which quantifies retinal vascular injuries in microscopic images of clinically relevant eye diseases, including diabetic retinopathy. The method I have developed extracts five unique features of retinal vasculature, such as the number of endothelial cells versus pericytes, the number of ghost capillaries, vasculature area, and fractal dimension. The gold standard is the manual evaluation of all these parameters under the microscope, which is a tedious task and prone to error. Using this multi-parameter analysis method, I have studied not only early structural changes in retinal vasculature due to diabetic retinopathy (DR) and Bcl-2 deficiency, but also the effect of disease progression on vasculature morphology. Quantification using this method will be helpful in evaluating physiological and pathological retinopathy in a high throughput and reproducible manner.

In addition to eyes, lungs were another organ of interest and focus of my research. One of the aims of my lung studies was to evaluate structural changes in lungs due to injury for the purpose

of real-time disease diagnosis. To satisfy this need, I have developed a fast image processing algorithm to detect alveolar walls and quantify dynamics of alveoli morphological changes in lung in rodent models of edema injury. This method extracts and statistically quantifies four parameters, including diameter and area of each alveolus, total number of alveolar sacs, and alveoli expiration compliance. This experimental study was conducted *ex vivo* using SD-OCT to capture real-time cross sectional images of alveolar structure in a ventilated and buffer perfused isolated rat lung.

My research has also focused on developing a novel model that accounts for the dynamics of the metabolism and oxidative stress (OS) in live cells. Oxidative stress is extensively involved in pathologies of various diseases. However, the spatiotemporal dynamics of OS are not well understood. Using fluorescence time lapse microscopy, I quantified and modeled the dynamics of OS concentration in lung injuries. My work led to design of a new methodology and an experimental protocol to quantify the changes of OS in different stress conditions, and even localize the site of OS in an uncoupled state of pulmonary artery endothelial cells (PAECs). The results demonstrated that mitochondrial respiratory chain uncoupling and inhibiting involves the exponential up-regulation of the superoxide level, leading to more mitochondrial damage. The method I developed is also able to partition the OS production from different mitochondrial complex sites and provides a way to identify the source of OS production. This study sets the stage for applying our methods to study different injuries *in vitro*.

As a side project, I have also been working on a computational image processing algorithm to solve an inverse problem for fluorescence lifetime tomography in turbid media. This algorithm was part of a Diffuse Optical Tomography project to confirm targeting the Rhodopsin channel for functional brain imaging. The algorithm I developed was based upon conjugate gradient method for least squares and provided the spatial images of fluorophore concentrations as well as lifetime

of fluorophores. The developed technique resulted in 100% localization accuracy and gave quantifications which were accurate within 15% of the true values for known strongly scattering phantoms with sparse fluorophore distributions.

Conducting all of these experimental studies required the assembly of the required tools, and designing experimental protocols to study the metabolism in the cryogenic, *ex vivo*, *in vivo* and *in vitro* regimes. For each regime used in this study, unique treatment and preparation of the tissues, as well as proper imaging and acquisition methods are required. Lungs and eyes, PAEC cells and retina microscope slides were provided by the VA hospital, the Medical College of Wisconsin, and University of Wisconsin-Madison. SD-OCT system was designed and implemented by our collaborators in the BIST lab, University of Wisconsin-Milwaukee.

Journal Publications and Conference Papers

J1) **Zahra Ghanian**, Ganesh Kondouri, Amadou Camara, and Mahsa Ranji," Quantitative Optical Studies of Mitochondrial Superoxide in Pulmonary Artery Endothelial Cells", submitted to Biophysical Journal.

J2) **Zahra Ghanian**, Kevin Staniszewski, Christine M. Sorenson, Nader Sheibani, and Mahsa Ranji," Quantitative assessment of retinopathy using multi-parameter image analysis", Journal of Medical Signals & Sensors, Vol. 6, No 2, April 2016.

J3) Fahimeh Salehpour, **Zahra Ghanian**, Chun Yang, Nadezhda Zheleznova, Theresa Kurth, Ranjan Dash, Allen Cowley, Mahsa Ranji, " Effects of p67phox on the mitochondrial oxidative state in the kidney of Dahl salt-sensitive rats: optical fluorescence 3-D cryoimaging", American Journal of Physiology-Renal Physiology, Vol. 309, No. 4, August 2015.

J4) **Zahra Ghanian**, S. Maleki, H. Reiland, D. E. Butz, G. Chiellini, F. Assadi-Porter, and Mahsa Ranji, "Optical imaging of mitochondrial redox state in rodent models with 3-iodothyronamine", Journal of Experimental Biology and Medicine, Vol. 239, No. 2, February 2014.

J5) **Zahra Ghanian**, S. Maleki, C.M. Sorenson, N. Sheibani and M. Ranji, "Optical Imaging of Mitochondrial Redox State in Rodent Model of Hereditary Hemorrhagic Telangiectasia-1 (HHT1)", Journal of Biophotonics, Vol. 7, No. 10, October 2014.

J6) S. Maleki, S. Gopalakrishnan, **Zahra Ghanian**, R. Sepehr, H. Schmitt, Janis Eells, Mahsa Ranji, "Optical Imaging of Mitochondrial Redox State in Rodent Model of Retinitis Pigmentosa ", J Biomed Opt, Dec 13 2012.

J7) **Zahra Ghanian**, A. Abdipour, A. Ghorbani, “Nonlinear Analysis, Design and Implementation of a VCO in S Frequency Band”, Springer Journal on Analog Integrated Circuits and Signal Processing Volume 49, Number 2, Pages: 213- 223. http://www.springerlink.com/content/t62457508484/, October 2006.

J8) **Zahra Ghanian**, A. Abdipour and M. Hakkak, “Design, Graphical Optimization and Nonlinear Analysis of Power Amplifier in Ka Frequency Band”, Science-Research Journal of Modarres, No.7, Pages: 35-51, May 2002.

C1) Shima Mehrvar, **Zahra Ghanian,** Ganesh Kondouri, Amadou S. Camara, and Mahsa Ranji, " Time-lapse microscopy of lung endothelial cells under hypoxia ", SPIE Photonics West Conference, Feb 2017.

C2) **Zahra Ghanian**, Ganesh Kondouri, and Mahsa Ranji, "Time lapse fluorescence microscopy of Reactive Oxygen Species (ROS) performed *in vitro* demonstrates a major role for complex IV in ROS generation ", BMES Southeast Conference, October 23, 2015.

C3) **Zahra Ghanian**, Ganesh Kondouri, and Mahsa Ranji, "Time lapse microscopy of oxidative stress in lung endothelial cells", Proc. SPIE 9531-3, May 25, 2015.

C4) **Zahra Ghanian**, Ganesh Kondouri, and Mahsa Ranji, "Optical Studies of Oxidative Stress in Persistent Pulmonary Hypertension Cells", OSA, April 2, 2015.

C5) **Zahra Ghanian**, Annie Eis, Ganesh Kondouri, and Mahsa Ranji, "Optical Studies of Oxidative Stress in Pulmonary Artery Endothelial Cells", Proc. SPIE 9328, Imaging, Manipulation, and Analysis of Biomolecules, Cells, and Tissues XIII, 932807, March 2, 2015.

C6) Mahsa Ranji, **Zahra Ghanian**, Farid Atry, Seth Frye, Ramin Pashaei, and Said Audi, "Optical instrumentation and Image Cytometry of Lung and Eye Injuries: Studies in the Rodent Model", Proc. Biomedical Optics, BIOMED.BT3A.58, Miami, Florida, April 2014.

C7) **Zahra Ghanian**, Kevin Staniszewski, Christine M. Sorenson, Nader Sheibani, and Mahsa Ranji, " Cytometric Analysis of Retinopathies in Retinal Trypsin Digests", Proc. SPIE. 8947, Imaging, Manipulation, and Analysis of Biomolecules, Cells, and Tissues XII, 89471Y., March 04, 2014.

C8) Micheal Rogowski, **Zahra Ghanian**, Ebru Selen, S. Maleki, Z. Bolandnazar, F. Assadi-Porter, M. Ranji, "Metabolomics and optical imaging show tissue specific mitochondrial oxidative stress as early biomarkers of polycistic ovary syndrome," 5th Texas Tech Annual Biological Sciences Symposium (TTABSS), Texas, March 2014.

C9) **Zahra Ghanian**, M. MasoudiMotlagh, S. Maleki, Z. Bolandnazar, F. Assadi-Porter, M. Ranji, "Optical Redox Imaging of Metabolic Dysfunction in Polycystic Ovary Syndrome," BMES Annual conference, Seattle, Oct 2013.

C10) **Zahra Ghanian**, C.M. Sorenson, N. Sheibani, M. Ranji, "Optical Imaging of Cellular Redox State Related to Retinopathy Dysfunction in Endoglin Heterozygous (Eng+/-) Mice," UWM CEAS Research Day, April 2013.

C11) **Zahra Ghanian**, C.M. Sorenson, N. Sheibani and M. Ranji, "Optical Imaging of Cellular Redox State in Endoglin Heterozygous (Eng+/-) Mice", IEEE Sponsored Conferences & Symposia, Feb 2013.

C12) **Zahra Ghanian**, S. Maleki, S. Golpalakrishnan, R. Sepehr, J. Eells, M. Ranji, " Optical Imaging of Oxidative Stress in Retinitis Pigmentosa (RP) in Rodent Model", Proc.

SPIE 8591, Optical Diagnostics and Sensing XIII: Toward Point-of-Care Diagnostics, 85910S, February 25, 2013.

C13) **Zahra Ghanian**, Christine Sorenson, Nader Sheibani, M. Ranji, "Optical Imaging of Oxidative Stress in Diabetic Retinopathy", BMES Oct 2012.

1.2 Biological background

1.2.1 Cell physiology and metabolism

All known living organisms are composed of cells [3]. Cells are the structural and functional units of life. A generalized structure of the animal cell is shown in figure 1-1(a) [4]. Many injuries and diseases can be traced back to irregularities in the behavior within the cell [5]. Early detection and treatment of such injuries could lead to a significantly lower rate of permanent damage and help in reducing further therapy's costs.

Although all sub-cellular organelles are essential for the organism to remain healthy and viable, the mitochondrion (see figure 1-1(b)) [6, 7] plays the most critical role for metabolic processes [8]. The mitochondria are responsible for the chemical reactions resulting in providing energy for the cells and are necessary for sustaining life in a biological organism [9].

The metabolic process is generally achieved through a series of reactions referred to as aerobic respiration [10]. In this process, a chain of the mitochondrial coenzymes is oxidized resulting in adenosine triphosphate (ATP), which is the unit of energy for the cells. The amount of energy that can be supplied for the cell is positively correlated to the amount of oxygen present in the mitochondria, and an irregular amount of oxygen in the cell and its surrounding environment (oxidative stress) leads to perturbation to cell functions and eventually cell death. The majority of energy in the cell is produced this way via the electron transport chain [8], which is represented in figure 1-2 [11].

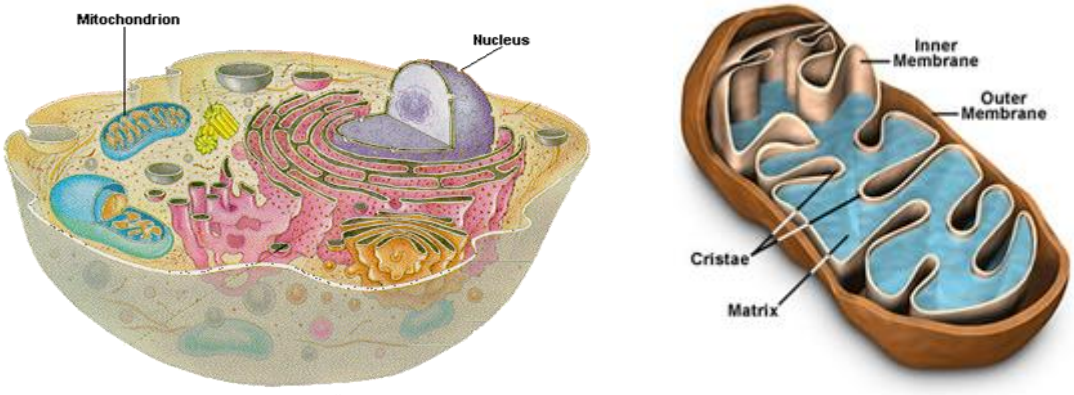

(a) (b)

Figure 1-1: (a) Cell structure including its organelles with the nucleus and mitochondria pointed out [9], (b) Mitochondrion and its organelles. [18].

The electron transport chain is a complex system of chemical reactions that take place in the inner mitochondrial membrane and is used to create a proton gradient across the membrane by pumping excess hydrogen ions into the mitochondria's "intermembrane space" [12]. In the electron transport chain, two coenzymes, nicotinamide adenine dinucleotide (NADH) [13] and flavin adenine dinucleotide ($FADH_2$) [14], are oxidized through a series of protein complexes resulting in a release of protons, which are pumped into the intermembrane space using a portion of the energy released, thus creating a proton gradient.

Finally, ATP is generated by the release of these protons to the intermembrane space through ATP synthase [8] in conjunction with adenosine diphosphate (ADP) and inorganic phosphate. A change in the oxidation state of these two cofactors, or in other words, a change in the concentration of the oxidized form, is a direct marker of a change in tissue oxidation status and metabolism [15].

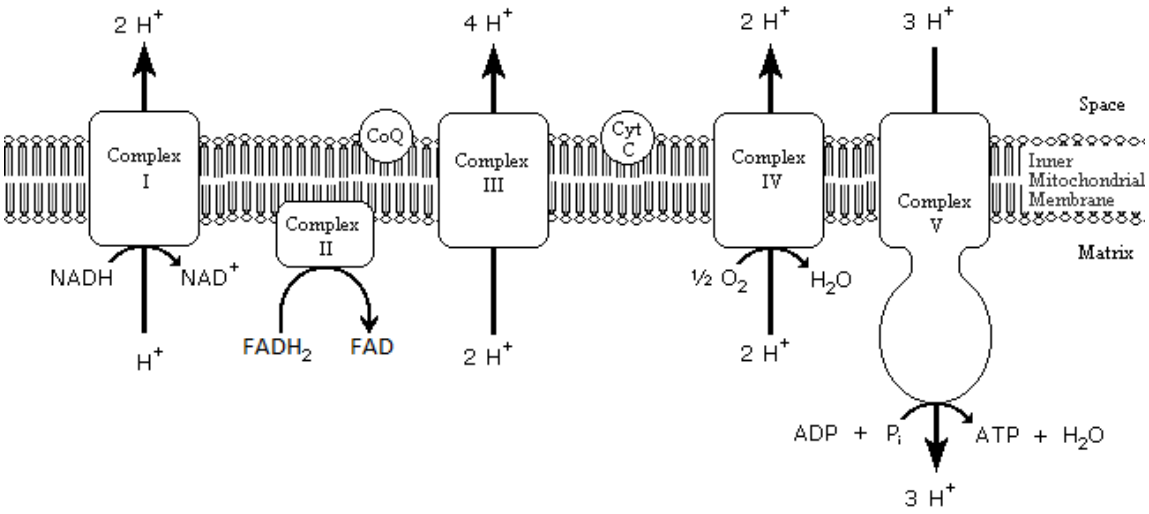

Figure 1-2: Simplified block diagram of the electron transport chain.

1.2.2 Oxidative stress

ROS are chemically reactive molecules containing oxygen and play a vital role in cell signaling, redox regulating, and, when in excess, leading to oxidative stress that is extensively involved in pathologies of various diseases. The production of ROS is an inevitable consequence of physiological aerobic metabolism. Incomplete processing of oxygen and release of free electrons result in the production of mitochondrial ROS. It has been shown, however, that mitochondria produce ROS at a rate higher than their scavenging capacity, resulting in incomplete metabolism of approximately 1–3% of the consumed oxygen [16, 17]. The byproducts of incomplete oxygen metabolism are superoxide ($\bullet O_2^-$), hydrogen peroxide (H_2O_2), and hydroxyl radical ($OH\bullet$). Oxidative stress, which is often due to an irregularity in the amount of oxygen introduced to the mitochondria, represents an imbalance between production and consumption of ROS. An excessive amount of ROS or the production of peroxides and free radicals, can cause

damage to any and all parts of a cell [18]. This is especially important given that a variety of diseases can disrupt the balance of oxygen flow into and around cells, causing improper function of the mitochondria, and thus an increased rate of cell death via apoptosis or necrosis [19]. A slight increase in oxidative stress leads to mitophagy, in which the mitochondria degrades, but the cell manages to recycle the nutrients released. However, as oxidative stress increases, the cells begin to undergo apoptosis, or programmed cell death, or in extreme cases, necrosis, which is abnormal cell death. In many cases, the amount of oxygen available to a cell can accurately represent the health of the cell and to be used as a diagnostic tool. This is especially true in cases related to mitochondrial dysfunction or diseases related to oxidative stress. In these cases, the oxidation state, or redox state of the tissue serves as a sensitive and reliable measure for the evaluation of cell behavior [20].

1.3 Fluorescence

1.3.1 Principles of fluorescence

Fluorescence optical imaging techniques have the potential to investigate tissue's health in real time, in a non-destructive manner, and in intact organs, both *in vivo* and *ex vivo* [21-27]. These techniques can also monitor metabolic state in diseases of clinically important disorders such as cardiopulmonary injuries, and diabetic retinopathy. Using the fluorescent signals of intrinsic fluorophores present in the cell, it is possible to determine the oxidation status of the cell. In these studies, fluorescence imaging is used to study organ specific bioenergetics [1, 28, 29], mainly eye [1] and lung [30, 31].

A fluorophore is a chemical compound, which can emit photons with specific wavelengths, when excited with specific higher-energy photons [32]. The basic principle of fluorescence is shown in a Jablonski diagram in figure 1-3.

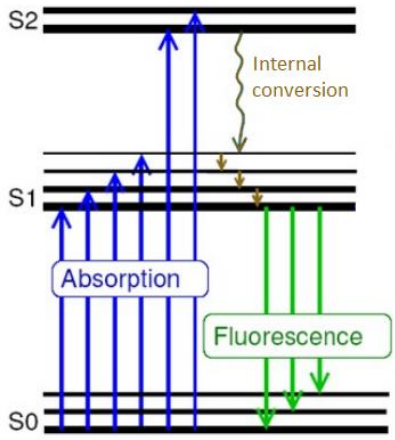

Figure 1-3: Jablonski Diagram of Fluorescence. Fluorescence as a result of molecule excitation. Blue lines indicate excitation, gold lines relaxation, and green lines emission of fluorescence [4].

First, the molecules of fluorophores are in an initial energy state, resting state S_0. Once the resting molecule is exposed to a source of energy, it absorbs the energy from the incident source and goes to an excited energy state (S_1, or S_2). Once there, a portion of the energy is lost to lattice vibrations and other avenues prior to the release of a photon and relaxation to the initial energy state. In the transition back to the ground state, there is a probability, termed the fluorescence quantum yield, of emitting photons of lower energy than the excitation photons. These emitted photons, can be collected by a photoelectric device to quantify the amount of energy released [33].

For intrinsically fluorescent molecules, there is a narrow range of photon energies, which can cause this excitation, corresponding to the allowable energy states of the molecule. Since the energy of a photon is inversely proportional to its wavelength, or directly proportional to the frequency, this means that only a specific range of wavelengths can be used to excite a given molecule. In addition, because the emitted photon has an energy equal to the energy released when the molecule transitions back to its ground state, the wavelength of this light has a narrow band.

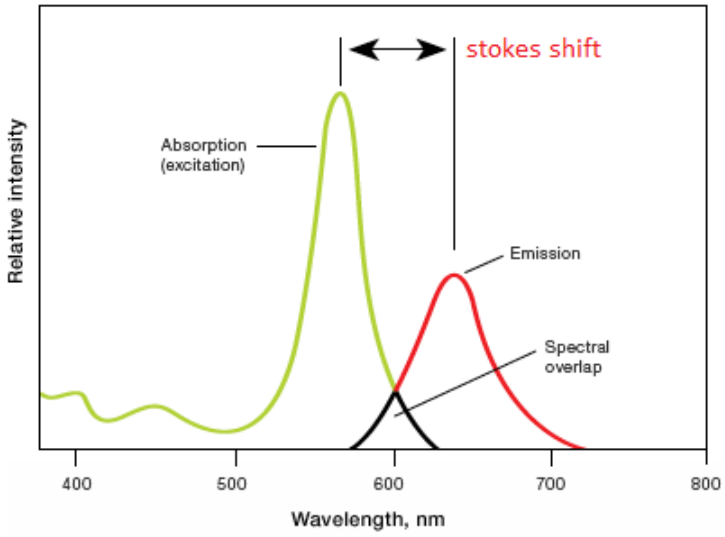

Figure 1-4: Stokes shift.

Finally, since the molecule lost some energy along other pathways, the emitted photon has a lower energy, and therefore longer wavelength compare to the excitation light. This phenomenon is known as ***Stokes shift***, and is shown in figure 1-4 [34, 35]. Thus, the excitation (absorption) and emission spectra for each molecule are different. This phenomenon can be exploited through the use of optical filters or dichroic mirrors to separate the excitation and emission light. This way, only the emitted fluorescence signal will reach the detector. The narrow spectra of both the excitation and emission light is actually beneficial, since multiple molecules can be monitored sequentially, provided that their fluorescence spectra are not completely overlapping [20].

The probability of emitting a fluorescent photon after absorption of an excitation photon, termed the fluorescence ***quantum yield***. This probability is a convenient measurement of the efficiency of the fluorescence process. It is defined as the ratio of the number of photons emitted to the number of photons absorbed [34, 35].

1.3.2 Intrinsic mitochondrial fluorophores

Intrinsic fluorophores are naturally occurring fluorophores. There are several cellular intrinsic flourophores within tissues including NADH, flavins, tryptophan, collagen, and porphyrins, which are useful to measure the functional and structural capacity of the tissue. Two of these fluorophores, NADH and FAD (one of the flavins), are of particular interest since they play an essential role in the metabolic pathway of mitochondria. These two flourophores originate from first and second complex sites of the electron transport chain [8] and can be used as markers of cellular metabolic state. The spectra of these auto-fluorescent coenzymes are shown in figure 1-5 [36, 37].

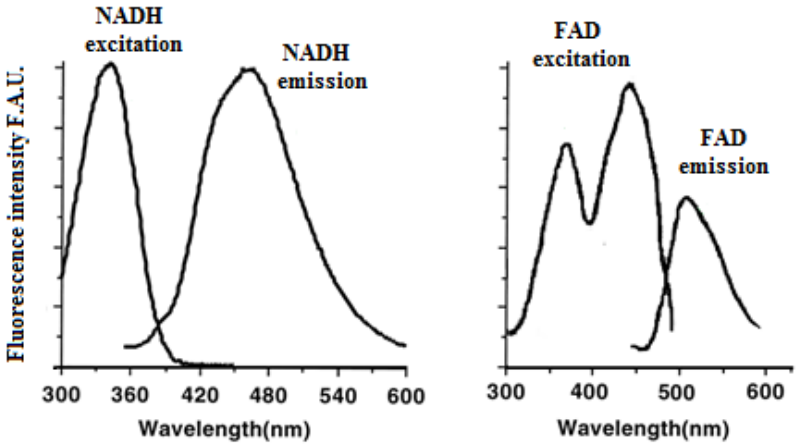

Figure 1-5: Excitation and emission spectra of NADH and FAD.

NADH is primarily fluorescent in the reduced biochemical state, whereas FAD only fluoresces in the oxidized form. Therefore, the ratio of the concentration of these two fluorophores, called the mitochondrial redox ratio, can show the oxidative state of the metabolism within the tissue [38]. This ratio is beneficial as a quantitative marker of tissue metabolism, which is independent of the number of mitochondria. Since NADH and FAD (the oxidized form of $FADH_2$)

are autofluorescent, they can be monitored without exogenous labels by noninvasive optical fluorescence techniques [24].

NADH and FAD can be excited by filtering a white light such as light from a mercury arc lamp at their excitation wavelengths. NADH has a maximum in its excitation spectrum at around 340 nm and an emission maximum at 460 nm, and FAD has its excitation maximum at 448 nm and a maximum in the emission spectrum at 520 nm. The overlap between NADH emission and FAD excitation requires that the two fluorophores be excited and detected sequentially, but the fact that the emission spectra do not overlap with each other allows for selective detection of fluorescence between the two fluorophores. Hence, by detecting the fluorescence of each of these fluorophores, one can obtain a measure of the oxidation state of cells within an organ.

Although redox ratio is independent of the number of mitochondria, each of NADH and FAD fluorescent signals are dependent on the concentration of mitochondria. These signals are also affected by the presence of interfering factors such as other endogenous fluorophores with the same excitation/emission spectra (namely NADPH and collagen). This factor can be effectively canceled out using redox calculations. As for the interfering fluorophores, since they are not involved in the mitochondrial electron transport chain, their fluorescence does not interfere with NADH and FAD fluorescent signals (see chapter 2 for more details). As a result, the changes in the measured redox ratio are due to changes in the mitochondrial redox state, and are not impacted by the other endogenous fluorophores present in the tissue [28].

1.3.3 Florescence imaging techniques

Fluorescence optical techniques provide quantitative physiological and structural information reflecting disease progression. Furthermore, these techniques have been shown to possess a high sensitivity and specificity for discriminating between diseased and healthy tissue

[39]. Optical imaging of the intrinsic fluorophores namely, NADH and FAD, have been widely used as indicators of tissue metabolism in injury due to hypoxia [22, 40], hyperoxia [30, 41], ischemia-reperfusion [22, 40], diabetes [42] and also as indicators for the response of different treatments such as photodynamic therapy [43], and cancer therapy [44-46].

Various groups have used optical monitoring of cancer tissue in different diseases. Mycek et al. have used an optical technique in studies of pancreatic cancer in clinical practice [47]. Ramanujam et al. have shown the ability of endogenous redox imaging to differentiate normal, precancerous, and cancerous squamous epithelial tissues by multiphoton microscopy [48] [39]. Mayevsky's group has used NADH spectroscopy and blood oxygenation in brain tumor metabolism studies *in vivo* [49-51]. Kortum's group examined optical imaging for diagnosis of cervical cancer [52], and Vo-Dinh et al. investigated an optical fluorescence technique for esophageal cancer and dysplasia diagnosis [53]. Georgakoudi et al. have worked on endogenous redox ratio in human epithelial cell apoptosis studies [54].

Our group has recently studied different organs including lungs and hearts in the injury models such as ischemia-reperfusion and hyperoxia [22, 30], as well as retina in diabetic retinopathy [1, 55] and retinitis pigmentosa models [148].

Overall, we have used optical biopsy, cryoimaging, fluorescence spectroscopy and microscopy to monitor metabolic state in diseases of clinically important disorders [1, 28, 30] [22, 30] as well as the effect of the metabolic therapy on heart and kidney [28]. The future goal of our research is to translate optical imaging to clinical avenues, and to transfer the instruments developed for animal models to bedside for patient diagnosis.

1.4 Rodent injury models and diseases

ROS has been implicated in the pathogenesis of many acute and chronic ocular disorders. ROS has important impact during angiogenesis, and their aberrant production is linked to retinopathy of prematurity and diabetic retinopathy [56, 57]. Diabetes plays crucial role in regulation of apoptosis and vascular function of retina and pathogenesis of diabetic retinopathy. Diabetes is a systematic disease, which can eventually lead to blindness [58-62]. Diabetic retinopathy affects up to 80 percent of all patients who have had diabetes for 15 years or more [63]. Despite these intimidating statistics, much of the damage could be reduced if there was *early detection* and proper treatment. Hyperglycemia or high blood sugar is a condition in which an excessive amount of glucose circulates in the blood plasma. Excess generation of highly reactive free radicals, largely due to hyperglycemia, causes oxidative stress, which further exacerbates the development and progression of diabetes and its complications [62-64]. Two rodent models of retinopathies were investigated in this study including, Akita/+ (diabetes), and Bcl-2 deficient (Bcl-2-/-) mice.

The ***B Cell Lymphoma Gene (BCL-2)*** *gene* plays an essential role during eye development and lack of bcl-2 (Bcl-2-/- mice) enhances apoptosis affecting eye development and growth [64-70]. The bcl-2 expression regulates angiogenesis, and its deficiency is associated with decreased number of vascular cells and vascular density in the retina [68, 70]. Bcl-2 is important for maintaining mitochondrial oxidative homeostasis [71, 72]. In addition, bcl-2 expression is significantly decreased during diabetes [73], thus, its absence causes a more oxidized state in tissue and, as such, the mitochondria is more oxidized in bcl-2-/- mice as compared with their controls. As an anti-apoptotic protein whose expression decreases significantly during diabetes, bcl2 is of direct interest for this study.

*The **Akita** mouse*, which has a mutation in the insulin 2 gene, is a model for diabetes. Akita diabetic mice develop type 1 diabetes as early as 4 weeks of age and show normal survival until 6 months of age, but then show a dramatic decrease in survival with almost no survivors from 12 months of age. Enzymatic and non-enzymatic sources contribute to ROS observed in the diabetic retinas [74-76], including mitochondrial respiration chain deficiencies. Using our optical imaging techniques, we have studied morphological alternations as well as changes in metabolic state and oxidative stress in retina from this model by our optical imaging techniques.

***Endoglin heterozygote** mice* is another model of injury in our study. Endoglin (Eng)/CD105 is a type I membrane glycoprotein, which is highly expressed in vascular endothelial cells (EC). Loss-of-function mutations in the human endoglin gene cause a dominant vascular dysplasia known as Hereditary Hemorrhagic Telangiectasia, HHT-1. HHT disease-causing genes encode proteins that modulate transforming growth factor (TGF)-β superfamily signaling in vascular endothelial cells. It has been shown that heterozygous mutations in Endoglin (Eng) and Activin receptor-like kinase 1 (Alk1) cause HHT-1 and HHT-2, respectively [77-83]. Both of these genes are expressed predominantly in endothelial cells [84, 85]. HHT-1 is associated with frequent nose bleeds, telangiectases, mucosa, and arteriovenous malformations in lung, liver, and brain [77, 86]. Ocular involvement has been reported in patients with hereditary hemorrhagic telangiectasia. Intraocular vascular lesions, including retinal telangiectasia, arteriovenous malformation in the retina, and abnormal choroidal vascular changes were reported [87-91]. Sudden visual loss has been described because of ocular involvement [91], bleeding from kidney and urinary vascular malformations are other complications reported in HHT patients [92, 93]. Here, the Eng-related hereditary haemorrhagic telangiectasia, HHT-1, is investigated.

Oxygen-induced ischemic retinopathy (OIR) in a mouse is a highly reproducible model of angiogenesis *in vivo,* and recapitulates the human retinopathy of prematurity condition [94]. In this model, postnatal day 7 (P7) mice are exposed to 75% oxygen for 5 days. During this time, the developing retinal vasculature is highly sensitive to high levels of oxygen. The high oxygen impedes further growth of blood vessels and causes obliteration of the existing vessels. At postnatal day 12, the mice are returned to room air (20% oxygen) for 5 days. During this stage, the lack of sufficient blood vessels causes the retina to become ischemic [94], up-regulating VEGF (Vascular Endothelial Growth Factor) expression and inducing angiogenesis. Unfortunately, these vessels are fragile and leaky, sprout into the vitreous, and hemorrhage, causing further damage to the retina. We have recently shown that endoglin haplo-insufficiency results in attenuation of retinal neovascularization during OIR [95]. Reactive oxygen species (ROS) play an important role during angiogenesis, and their aberrant production is linked to retinopathy [1, 56, 57]. In fact, antioxidants inhibit microvascular degeneration in models of diabetes and OIR [57, 96, 97]. The cellular mechanisms, which modulate intracellular oxidative state, however, are not fully characterized [98]. We recently showed that Eng+/- retinal EC are more resistant to oxidative challenge compared to Eng+/+ cells [95]. However, how these changes in vascular EC oxidative state translate to the organ specific alterations and the underlying mechanisms, need further investigation.

Heterozygous P23H-1 transgenic rat is an animal model for an injury called retinitis pigmentosa (RP). RP is a large, genetically heterogeneous group of inherited retinal degenerations characterized by progressive and neurodegenerative photoreceptor apoptosis [99, 100]. Oxidative stress (OS) and mitochondrial dysfunction contribute to photoreceptor cell loss in retinal degenerative disorders. Irreversible loss of rod photoreceptors is the outcome of abnormal

physiology associated with mutated or absent gene products and leads to blindness in many retinal degenerative disorders, including retinitis pigmentosa (RP) [101]. Considerable evidence supports a key role for mitochondrial dysfunction and oxidative damage in the pathogenesis of progressive photoreceptor cell death by apoptosis in RP both *in vitro* [102, 103] and *in vivo* [103-105]. We investigated the metabolic state of the retina in a rodent model of retinitis pigmentosa (RP) using a fluorescence cryoimaging technique.

There is an increasing evidence that reactive oxygen species (ROS) participate in diverse lung injuries [106-111]. *Persistent pulmonary hypertension of newborn (PPHN)*, which is associated with impaired pulmonary vasodilation at birth, is also affected by oxidative stress [112-114]. However, the regulation of mitochondrial superoxide during birth transition which lead to impaired angiogenesis is unclear [114-122] and subject of our study. In our injury model, PPHN is induced by fetal ductal constriction performed at 128 ± 2 days of gestation (term=144 days) [119]. After 8 days of ductal constriction, fetal lungs of lamb were harvested for the isolation of pulmonary artery endothelial cell (PAEC). We investigated if PPHN induces elevated ROS levels in endothelial cells. In the next step, it is intended to model the *in situ* cell injuries namely *hyperoxia* (exposure to elevated oxygen) and *hypoxia* (exposure to reduced oxygen level).

Hyperoxia, is a common and necessary therapy for adult and pediatric patients with acute respiratory distress syndrome (ARDS) to restore blood oxygen tension (PO_2) to a level that sustains vital organ metabolic requirements [123, 124]. However, sustained exposure to high oxygen concentrations (> 50%) causes lung oxygen toxicity injury. This injury, which is the result of enhanced production of ROS, i.e. oxidative stress, may further impair lung function and contribute to the very dysfunction that it is intended to alleviate [125, 126].

Monitoring the behavior of PAECs under long hypoxic conditions followed by normal condition and then hyperoxic treatment is advantageous, since it is a hypoxia injury model happening to the fetus at birth transition following initiation of respiration and then hyperoxic treatment. Furthermore, *Hypoxic* condition followed by normal oxygen condition is a model of *Ischemia-reperfusion* (IR) injury. IR is commonly encountered clinically in conditions such as lung transplantation, necrotizing pneumonias, or crush injury to the chest [127]. Approximately 1,500 lung transplants are successfully performed each year in the US [128] with many times that number lost due to prohibitive ischemic times.

Pulmonary alveolar edema is another lung injury associated with oxidative stress [129-137]. In this injury normally 'tight' alveolar epithelial intercellular junctions suddenly become freely permeable to proteins. Edema can be caused by a variety of factors, including conditions that affect osmotic pressure, such as hypotonic fluid overload, which allows the movement of water into the intracellular space, or hypoproteinemia, which decreases the concentration of plasma proteins and permits the passage of fluid out of the blood vessels into the tissue spaces. Conditions that increase capillary permeability, such as inflammation; and conditions that cause increased capillary pressure, such as pulmonary artery hypertension which is considered as an essential pathophysiologic factor [138, 139].

In all these ROS-mediated injuries, we have studied the effects and consequences of the damage on the electron transport chain. We monitored either the metabolic activities or structural alternations in these clinically important disorders and injuries using optical imaging tools with the future goal of translation to clinical avenues.

Chapter 2

Optical cryoimaging of oxidative stress in eye diseases

2 Optical cryoimaging of oxidative stress in eye diseases

Two auto-fluorescent coenzymes in the mitochondria, NADH and FAD, are imaged to measure the cellular redox state of organs. Cellular redox state is a quantitative marker to examine oxidative state of the tissue and estimate the amount of mitochondrial damage due to injury. Monitoring of NADH and FAD fluorescence are widely performed using optical fluorescence techniques to probe tissue redox state and energy homeostasis in organs such as the heart [1, 25], brain [27], kidney [1, 28, 29], liver [140], skeletal muscle [141], cervix [142], and colon [47]. However, using this method to measure redox state of the eye has not been previously reported. In this study, optical cryoimaging technique with high sensitivity and specificity for discriminating between diseased and non-diseased tissue is employed to measure ocular and retinal metabolic state.

Our cryoimaging system measures the metabolic state of organs by capturing higher fluorescence quantum yield of fluorophores as compared to room-temperature imaging techniques [38, 143, 144]. Stronger quantum yield leads to stronger fluorescence signal and higher signal to noise ratio. This property helps to detect metabolic changes in the early stage of the injury. Cryoimager also provides the snapshot of metabolism at the freezing time of the tissue and preserves the metabolic state of the organ. Furthermore, this system is able to acquire fluorescent images of fluorophores with different wavelengths including NADH, FAD, as well as bright field. Analyzing the captured images, one can demonstrate 3D spatial distribution of NADH, FAD, and redox fluorescence intensities in tissue. The 3D volumetric demonstration of the redox ratio is helpful to study the effect of the injury on both oxidation state and specific structure of the organs spatially.

In this chapter, a detailed description is given regarding the use of the cryoimager in eyes affected by different retinopathic injuries of clinically important disorders such as diabetic retinopathy, retinitis pigmentosa, Hereditary Hemorrhagic Telangiectasia (HHT-1) and Oxygen Ischemic Retinopathy (OIR). Mitochondrial redox state is measured in the eyes as a biomarker of oxidative stress level for diagnostic purposes. Moreover, the temporal and spatial distribution of oxidative stress in injured eye with different duration of disease is investigated. Furthermore, the metabolism of the retinal layer is also targeted which requires high resolution imaging of the eye. It should be noted that imaging is performed in cryogenic temperatures to achieve the strongest fluorescence signals. Due to strong fluorescence signals, cryo redox imaging serves as a diagnostic tool for *ex vivo* and *in vivo* studies of the organ metabolism. The results of this chapter provide a basis to apply optical fluorescent techniques to quantify the effects of different injuries on eye mitochondrial RR *ex vivo* and eventually *in vivo*.

2.1 Tissue Preparation

All animal experiments were conducted in accordance with the Association for Research in Vision and Ophthalmology Statement for the Use of Animals in Ophthalmic and Vision Research and were approved by the Institutional Animal Care Committee of the University of Wisconsin School of Medicine and Public Health.

Eyes from mice, as well as neonatal rats were used in the cryogenic studies of eye bioenergetics. A brief description of our eye tissue preparation protocols follows.

2.1.1 Akita/+, diabetic retinopathy, mice eyes

Akita/+ male mice were maintained and screened as previously described [145], at the University of Wisconsin-Madison. Briefly, Ins2Akita heterozygous (Akita/+) male mice were obtained from Jackson Laboratories. The colony was maintained by breeding C57BL/6J inbred females with Ins2Akita heterozygous males. Control animals were C57BL/6J male littermates. In all diabetic mice, diabetes was left untreated. Genomic DNA was prepared from tail biopsies and the transgenic Akita/+ mice were identified by PCR screening utilizing the following primers: 5′-TGCTGATGCC CTGGCCTGCT-3′ and 5′-TGGTCCCACATATGC ACATG-3′. The amplified fragments were digested with FNU 4 HI as recommended by Jackson Laboratories. The eyes were harvested from male Akita/+ mice with different duration of diabetes, 3 week (3W) and 6 month (6M). The Akita/+ mice develop diabetes by 4 weeks of age.

2.1.2 Retinitis pigmentosa, rat eyes

Albino SD normal and heterozygous P23H-1 transgenic rats, the offspring of P23H-1 homozygotes (Retinal Degeneration Rat Model Resource, UCSF) and SD normal albino rats (Harlan Laboratories, Madison) were fed ad libitum and maintained in a temperature and humidity-controlled environment under dim cyclic light, 12-h light/12-h dark cycle, with an average illuminance of 5 to 10 lux inside the cage. Once animals reached postnatal day 30 (P30), they were divided into two groups. The heterozygous P23H-1 rats were the model of retinal degeneration and SD normal albino rats were used as non-dystrophic controls. SD normal and P23H-1 transgenic rats were euthanized at P30.

2.1.3 Endoglin transgenic mice eyes, HHT-1

Endoglin heterozygous (Eng +/-) mice were provided by Dr. Dean Lee (University of Utah, St Lake City, UT) and the mice were screened as previously described [146]. The Eng +/- mice were identified by PCR analysis of DNA isolated from tail biopsies. The PCR primer sequences were as follow: Endoglin-forward: 5'-CACAGCTGTA ATCT CAGCACTTG-3', and Endoglin-reverse: 5'-GATTGGATCCATTGTGGTAGCTG-3'.

For the cryoimaging studies, eyes were then extracted from a total of 3 groups of mice in different ages, Eng+/- and Eng+/+ mice in 21 postnatal day (P21), 6 week (6W), and 10 month (10M).

2.1.4 Oxygen induced ischemic retinopathy, OIR, mice eyes

To prepare the oxygen-induced ischemic retinopathy eyes, the 7-day-old (P7) pups and mothers were placed in an airtight incubator and exposed to an atmosphere of 75 ± 0.5% oxygen for 5 days. Incubator temperature was maintained at 23 ± 2 °C, and oxygen was continuously monitored with a PROOX model 110 oxygen controller (Reming Bioinstruments Co., Redfield, NY). Mice were then brought to room air for 5 days [147]. After sacrificing a total of 2 groups of mice Eng+/- OIR and Eng+/+ OIR in 17 postnatal day (P17), eyes were extracted for the cryogenic studies.

2.1.5 Freezing Protocol and Embedding

Before fluorescence imaging, the extracted tissue was frozen and embedded as previously described [148]. A brief description of each step of this process follows.

Freezing: To preserve the metabolic state of the eye, fresh eye tissue was quickly frozen after harvesting in a chilled isopentane (methylbutane, Fisher Scientific, IL). The tissue was immersed in isopentane for one minute and then in liquid nitrogen (LN_2, -196^{o}C) for hours

followed by long-term storage at ultralow freezer (-80^{o}C). For fluorescence cryo-imaging, the frozen tissue was embedded in a customized black mounting medium and placed on a chilled aluminum plate to keep the tissue in place for freezing and slicing. This black mounting medium is not fluorescent in the NADH and FAD emission wavelengths and provides a good contrast between the fluorescent signals emitted from tissue and the background.

Mounting medium: The mounting medium was prepared in the Biophotonics Lab (UWM), using Polyvinyl Alcohol (PVA, Grade 71-30, PVOH7130, Chemical Store Inc., Clifton, NJ), distilled water and Indian ink. To make one liter of the embedding medium, 80g of PVA was added to 920g of boiling distilled water and stirred until the PVA completely dissolves. The liquid is heated to 300 ^{o}F for 1.5 hours. The solution should be stirred while boiling until the liquid becomes transparent and dense. Prior to adding Indian ink, the temperature of the solution should be turned down (250^{o}F) to stop boiling. Enough amount of ink should be added and mixed thoroughly to make the entire solution black. Heating at (250^{o}F) will continue for 30 minutes, and then the solution was allowed to cool down to room temperature. The mixture was stored in the refrigerator until needed. One day before use, the mixture was placed on the rotary motor rock tumbler to mix and warm up to room temperature.

Embedding: The embedding process began with freezing the base medium, embedding the eye horizontally and then fixing its position by adding more black medium around the tissue. Horizontal embedding of the eye is advantageous since the axis of the camera in front of the embedded eye will be perpendicular to the optical axis of the eye, and hence each z-slice includes a cross section of all different structures of the eye. After embedding, the tissue was stored in an ultralow freezer (-80^{o}C) for at most 24h prior to imaging. Before starting the experiment, the sample stand was installed on the sample carriage in the cryoimager such that the surface of the

black medium was parallel to the cryoimager microtome. Each injury group of eyes was imaged along with its corresponding control group within two days.

2.2 Imaging and Image Processing

2.2.1 Optical cryoimaging system

The custom-made cryoimager, described and used in this chapter (figure 2-1), sequentially slices the frozen tissue and acquire fluorescent images in up to five channels from each slice [149]. It was first developed and used in studying organ blood flow in small laboratory animals using microspheres [150]. The instrument determines regional blood flow by using the locations of fluorescent microspheres deposited in perfused rat hearts. The cryoimager excites and captures the images of the emission from the endogenous coenzymes, NADH and FAD. Each pixel of the captured images shows the intensity level of the fluorescent signal emitted from corresponding point of the biological sample. This information is translated to the concentration of the NADH and FAD coenzymes showing the metabolic states of the tissue under study.

Rapid freezing of organs in liquid nitrogen temperatures preserves the tissue's metabolic state [149] and provides the snapshot of metabolism at the time of freezing. Low temperature fluorescence imaging (cryoimaging) is advantageous since it provides stronger fluorescence quantum yield of NADH and FAD fluorophores as compared to room temperature [50, 144, 150] and so a higher signal to noise ratio. Cryogenic studies provide the strongest signals and the highest signal to noise ratio. Moreover, cryoimager provides 3D spatial distribution of tissue NADH and FAD fluorescence intensities [38, 143, 144]. 3D spatial distribution of NADH and FAD concentration in tissue indicates the metabolism of the tissue and show which part of the tissue is mostly affected by different injuries.

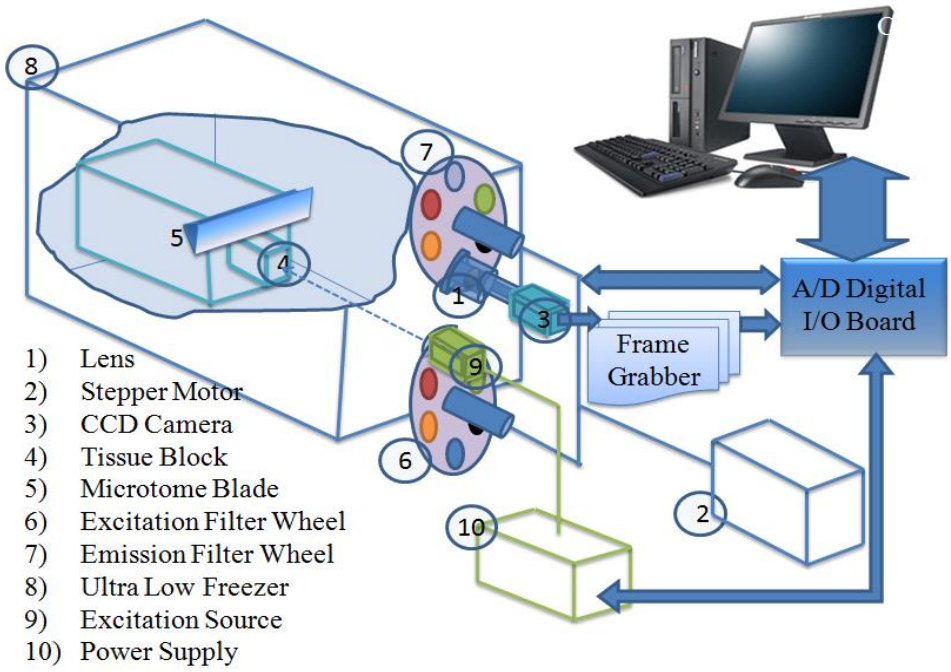

Figure 2-1: Schematic of cryoimager. This device sequentially slices the tissue and captures images of the tissue surface after each slicing in as many as 5 channels. The images are then displayed and saved to a computer for further processing and 3D renderings of the tissue.

The cryoimager consists of a cryo freezer, a cryo-microtome embedded inside the cryo freezer, and the optical parts and a workstation (Dell Computer) placed outside the cryo freezer. The optical components of the cryoimager are as follows: Rolera CCD camera (Rolera (QImaging, em-C^2 Rolera, 8μm pixel), a cold mirror, a reflecting mirror, a mercury arc lamp (200W, Oriel), an excitation (EX) filter wheel (provides up to five excitation wavelengths), and an emission (EM) filter wheel with synchronized rotation to EX wheel. Fluorescence images are captured using the digital camera (1004×1002-pixel array) with an either 200-mm Nikkor lens (Nikon, Tokyo, Japan) or Optem Zoom lens system (125C 12.5:1 Micro-Inspection, Qioptiq). Two motorized filter wheels (excitation and emission filters) are mounted in front of the light source and camera, respectively. The motor-driven microtome sequentially slices frozen tissue at the desired slice thickness while filtered light from the lamp excites fluorophores in the exposed surface of the

tissue. The microtome is housed in the cryo freezer, which maintains the sample at -40^{o}C during sample slicing and image acquisition. A LabVIEW (8.6 National Instruments) [151] program controls the microtome motor and two filter wheels as well as image capturing, display, and acquisition.

The excitation band pass filter used for NADH is 350nm (80nm bandwidth, UV Pass Blacklite, HD Dichroic, Los Angeles, CA) and for FAD is 437nm (20nm bandwidth, 440QV21, Omega Optical, Brattleboro, VT). The emission filter for NADH is 460nm (50nm bandwidth, D460/50M, Chroma, Bellows Falls, VT) and for FAD is 537nm (50nm bandwidth, QMAX EM 510-560, Omega Optical, Brattleboro, VT). At each slice, the camera captures fluorescence images of the tissue with a pixel size of 8μm. Lateral resolution of the cryoimager can be adjusted to 4-12 microns depending on the lens used in the setup. The axial resolution of the system is defined by the slice thickness and can be as small as 10μm. For this study, a resolution of 10μm was used in the z-direction, which resulted in around 250 z-slices per mice eye. Images are acquired with exposure times of 5-6 seconds for FAD and 2-3 seconds for NADH. Considering the time needed for rotating the filter wheels, as well as moving and slicing the sample, the whole imaging of a mouse eye takes 2.5 hours.

2.2.2 Version two of the cryoimager for eye imaging

In order to improve the performance of the system for the eye imaging and achieve high quality eye image, the following changes were made (figure 2-2). 1) Using Optem zoom lens with high magnification and low aberration instead of the canon lens. Optem Zoom lens system is capable of magnifying the image up to 6.5X without any auxiliary lens. With an auxiliary lens of 2X, it would magnify up to 13.0X without changing the main tube of the lens [13]. Choosing zoom lens is advantageous in another aspect as well. Zoom lens has an achromatic lens system with a

very small focal shift. The lens mechanism has a long tube, meaning the focal length is increased to reduce the focal shift, which results in less chromatic aberration. 2) Using small emission filter wheel containing filters with 1-inch diameter: Optem zoom lens has a large focal length with a slim body in respect to the Canon lens. Therefore, a small filter wheel is used in between the camera and the lens. 3) Changing the position of the filter wheel: in the traditional setup of the system, Canon lens was placed between filter wheel and camera. In the new setup, placing the filter wheel in between the lens and the camera gives us the freedom to move the lens closer to the sample, and collect more light before it dissipates.

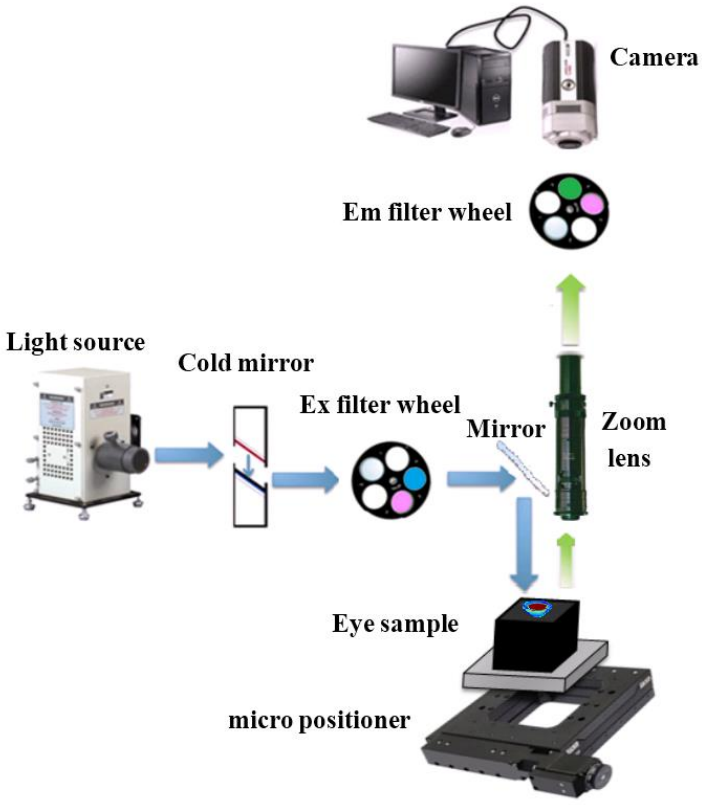

Figure 2-2: Version two of the cryoimager.

Before starting the experiment and imaging the eye samples, a piece of standard grid paper was placed on the surface of the embedded tissue to find the focal plane of the lens to capture in-focus images and determine the resolution of the system. The number of pixels within a known distance on both the x- and y-axis (of the grid image) was counted to get the number of microns per pixel in the horizontal and vertical directions to find the lateral resolution of the system. Knowing the magnification of the zoom lens and the pixel size of the camera, one can estimate the resolution of the imaging system (Image pixel size = camera pixel size / lens magnification). However, coherency of the light source and aberration caused by other optical elements in the light path affect the resolution as well. Therefore, standard grid paper in our imaging system gives a better estimate of the lateral resolution. For the eye imaging, replacing the Canon lens by the zoom lens improved the resolution of the cryoimager by a factor of 3.

A calibration method was also designed to partially correct for day-to-day variation of light intensity, and non-uniformity of the illumination pattern. A uniform fluorescent flat acrylic plate, which is highly resistant to photobleaching, was placed on top of the tissue block and imaged in all channels to acquire the illumination pattern. Changes in the fluorescence intensity of the standard plates in both the NADH and FAD channels accounts for day-to-day light intensity changes in both channels. The dark current image was also captured with the lamp shutter closed and the camera lens covered. This image is used for background subtraction. Acquisition of the tissue sections then followed calibration.

When the tissue has been completely imaged, each individual slice first has the dark image subtracted from it. The resulting image is then corrected for the non-uniformity of the illumination pattern by dividing by the image of the flat field plate captured in the same channel. Since the exposure time for flat field plates is not the same as exposure time for the tissue, this method can

only partially correct for the light variation over time. Therefore, great care was taken when imaging to ensure that all imaging parameters were constant between images. Furthermore, the injury samples with corresponding controls were embedded all together at the same day and imaged at the same day, as well.

Although the mercury arc lamp provides intense broadband light, it suffers from non-homogeneity of the illumination pattern. In order to couple the generated light to the cold mirror and excitation filter wheel, a condenser was used which deteriorates the homogeneity of the illumination pattern. To improve the homogeneity, the condensing factor was decreased by adjusting the knobs of the condenser. Using neutral density (ND) filters in the excitation path also improves the homogeneity of the light, but also reduces the intensity of the excitation light. To compensate for a lower intensity level, longer exposure times were set for the imaging.

The modified cryoimager make it possible to distinguish the different structures of a small organ like mice eye including retinal layer, sclera, choroid, vitreous, lens, and anterior chamber from both NADH and FAD images (Figure 2-3). However, discriminating the sub-structure and different layers of retina is not possible by cryoimager unless we use staining and there is no method currently available for tag-free structure (molecular and cellular level) imaging.

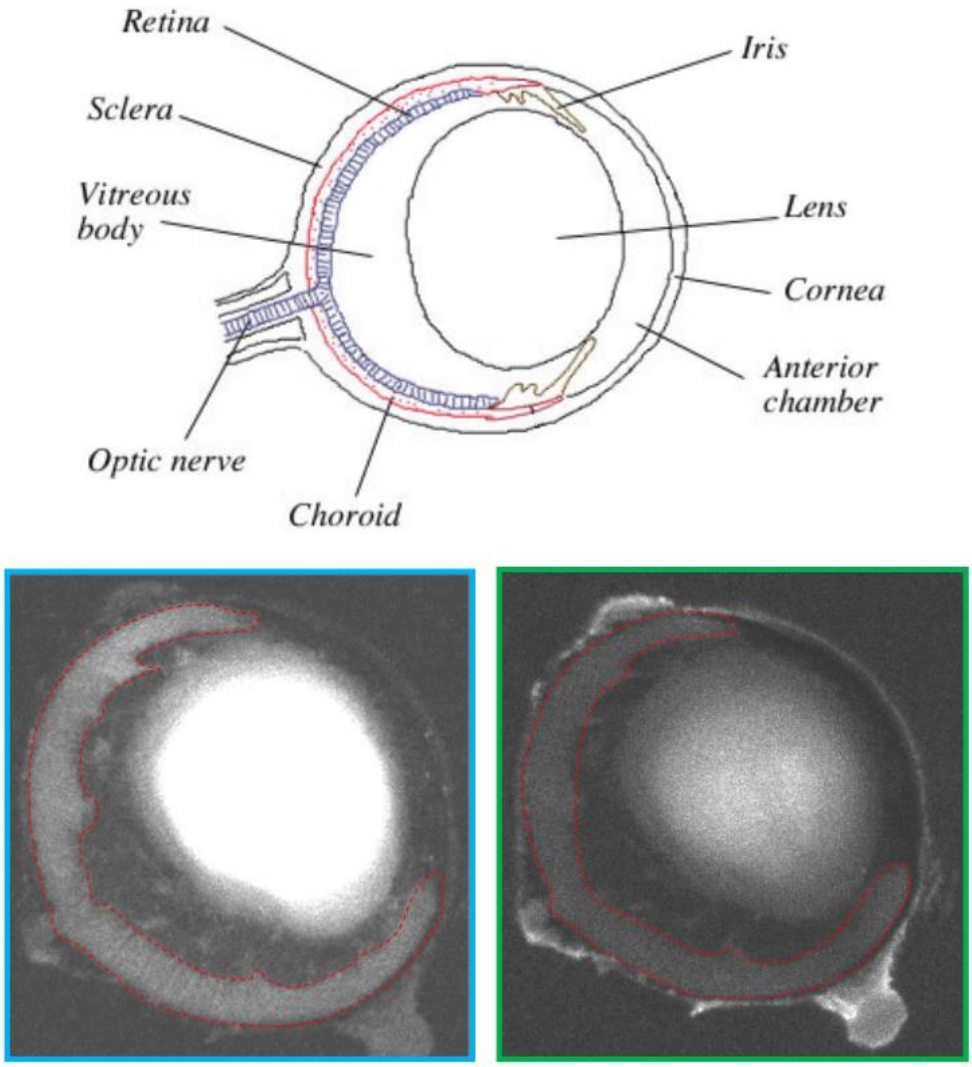

Figure 2-3: Top: anatomy of a rat or mouse eye (lateral view). Bottom: A 2D cross section image of mice eye in Left- NADH fluorescent channel, and right- FAD fluorescent channel. Retinal layer was highlighted with the red dash lines in both images.

2.2.3 Image Processing

Figure 2-4 demonstrates the steps of the image processing program for the calculation of the redox value, and 3D representation of the redox. After image acquisition, FAD and NADH autofluorescence images from each eye (containing 250 slices) were processed offline using MATLAB (r2015a, The MathWorks, Inc., Natick, MA). The preprocessing step includes background subtraction, and shadow correction.

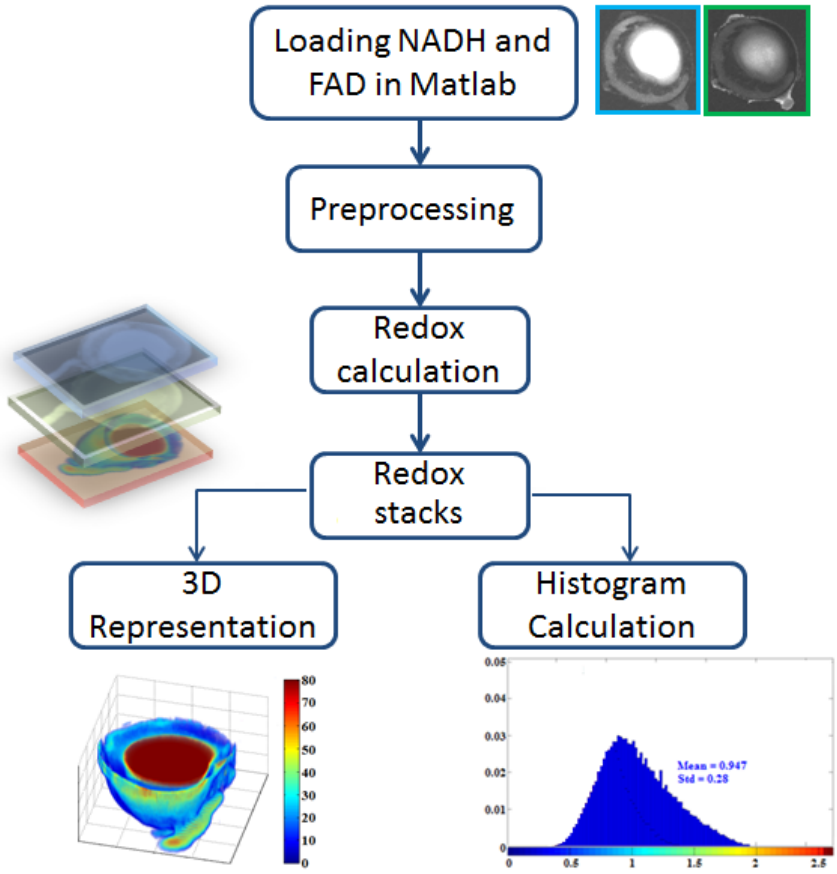

Figure 2-4: A schematic illustration of the image processing steps to obtain the 3D representation and histogram of the eye redox from the input fluorescent images.

The composite images were then created using all the image slices for each eye, for both NADH and FAD signals. The ratio of NADH and FAD (RR) [152, 153], was calculated voxel by voxel, according to equation (2-1).

$$\text{Redox Ratio} = RR = NADH / FAD \qquad (2\text{-}1)$$

The 3D representation of Redox for each eye was then calculated using z-stacks of images in FAD and NADH channels. In this method, NADH fluorescence images are divided by the corresponding FAD images, pixel by pixel, to calculate the NADH redox ratio for each slice of the tissue sample. These slides are used to construct the redox stack. The 3-D volume redox of the organ was constructed and the corresponding histograms were plotted.

The histograms of Redox in each group, diseased and normal were created, and the mean (first moment) of these histograms were calculated for quantitative comparison between normal and diseased groups. A histogram of the whole volume of each eye is plotted and the mean was calculated according to equation (2-2).

$$Mean = \frac{1}{N_x \times N_y \times N_z} \sum_{i=1}^{N_x} \sum_{j=1}^{N_y} \sum_{k=1}^{Nz} eye_Volume(i, j, k) \qquad (2\text{-}2)$$

Where N_x, N_y and N_z are the number of voxels in x, y and z directions, respectively. The voxel size in x, y and z direction is 10μm. Due to background subtraction, black mounting medium (background) was excluded in the calculation of the histogram mean value.

The retina is the target layer to investigate the effect of retinopathy on tissue metabolism. Due to high metabolic activity of retinal layer in the eye, which is reflected by the large number of mitochondria in photoreceptor cells [154], retina has the main contribution in the metabolism and RR signal. Therefore, the sphere-like retinal shell (figure 2-5) was segmented using the method described by Penna et al. [155].

For the segmentation, the approximate thickness of the retinal layer (table 2-1) and the homogenous intensity distribution of the retinal layer were also used. As shown in figure 2-3 Retinal intensity changes between the vitreous and lens intensity levels in both NADH and FAD channels. Therefore, the intensity-based band pass filter is useful to further segment and smooth the segmented retinal shell. It worthwhile to note that the lens of the eye functions as a UV filter (300-400nm) to protect retina from UV-induced photo-damage [156, 157]. Therefore, lens absorbs most of the photons that would excite the NADH (whose peak excitation is 365nm), and are transmitted through the cornea and aqueous humor [158]. Therefore, it shows the highest intensity level in the fluorescence images among all the structures in the eye.

Table 2-1: The thickness of different layers in the back of the mouse eye, as well as the number of the cryoimager slides to expect the corresponding layer.

	Retinal layer [159]	Choroidal layer	Sclera layer [160]
Thickness (micron)	140-220	70-80	9-20
# of 10-micron slides	14-22	7-8	1-2

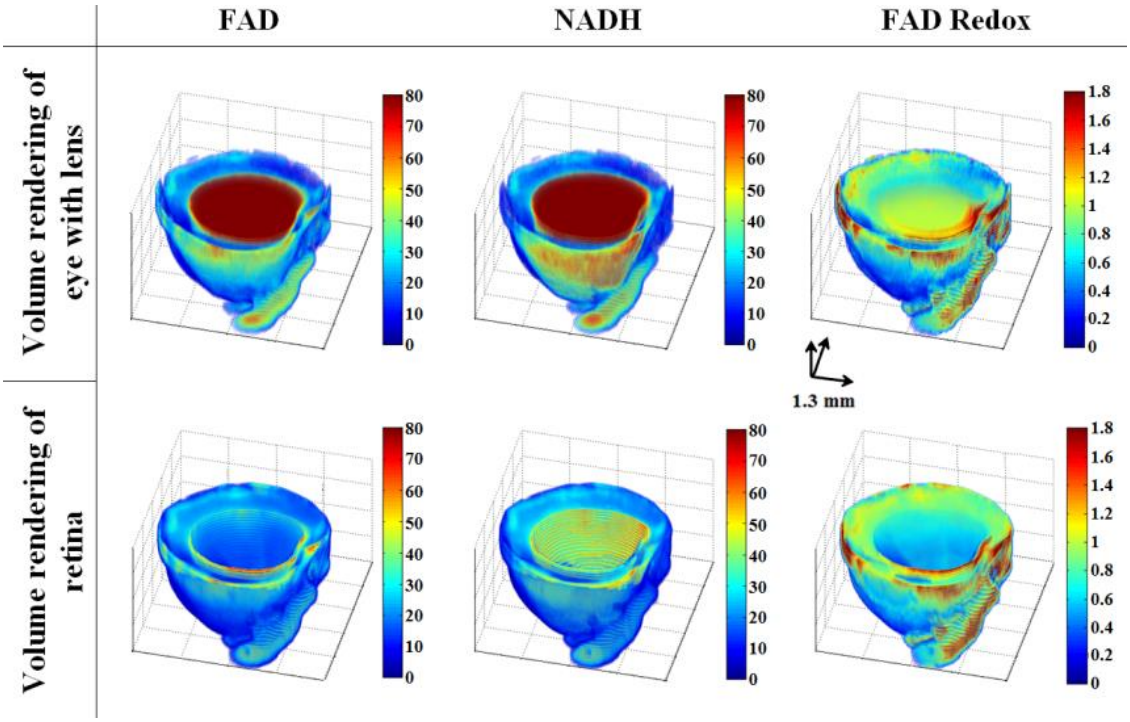

Figure 2-5: Images of FAD, NADH, and RR (FAD Redox; NADH / FAD) for one representative eye (10 months, Eng+/-). The top panel is the result of volume rendering of half of the eye (back of the eye which includes retinal layer) with the lens and the bottom panel is the volume rendering of the retinal shell with the connected optic nerve [1].

In addition to whole volume method explained above, there is another presentation method called maximum projection method. This method calculates the maximum intensities along the z axis of the composite images (3-D volume in NADH, FAD, and redox ratio). Maximum projection method is advantageous since it emphasizes the differences in the components. This method can reveal details, which are hidden in the whole volume method. The other advantage of this method

is less computationally intensive compared to whole volume method. The advantage of the whole volume method is that every single voxel of the images is used in redox calculations. This is beneficial in homogeneous tissue like retina and not the whole eye. Therefore, to compare the redox of the whole eye, which is a structured organ the maximum projection method was employed. However, for the redox quantification of the retinal layer the whole volume method was preferred.

For statistical analysis, the mean values of redox ratio (calculated from the redox histogram) was carried out for each group of diseased and normal eyes using a two-tailed Student's t-test with $P < 0.05$ as the criterion for statistical significance.

2.3 Results

Mice eyes suffering from diabetes with different durations of disease, 3 weeks and 6 months, are compared and the result is presented in figure 2-6. The top panel of the figure represents the max projection results of the NADH, FAD, and redox ratio (RR) images and the bottom panel demonstrates the histogram of these max projected images. For each histogram, the mean value was calculated as described in the image processing section. In this panel, the counts of each bin have been normalized to the total number of pixels in the eye. As a result of this normalization, the value of each bin corresponds to the percent of voxels in the eye with intensities falling within the given range. Therefore, the histogram can be considered as a scaled probability density function of mitochondrial redox ratio intensities for an eye. The mean values of these histograms for Akita/+ mice demonstrated decreased RR (increased oxidative stress, OS) in eyes from 3-week-old male Akita/+ mice (control, non-diabetic) to 6-month-old (the earliest time that

significant retinopathy is observed in Akita/+ mice retinal vasculature). A comparison between RRs of these diabetic eyes showed a 30% decrease with progression of disease from 3-weeks to 6-months of diabetes indicating increased OS. It should also be noted that 3 weeks' samples are non-diabetic, since male Akita/+ mice develop diabetes by 4 weeks of age.

Figure 2-7 displays, maximum projection images of NADH, FAD, and NADH RR for a representative eye in P23H transgenic and Sprauge Dawley (SD) normal rats. The images show a significant decrease in the mean NADH RR of eyes from diseased versus SD normal eye. The eyes in the SD normal group (first column in figure 2-7) show a lower concentration of FAD and a higher concentration of NADH compared to diseased group (second column in figure 2-7). Thus, the NADH RR is higher (more reduced) in eyes from SD normal rat eye compared to the eyes

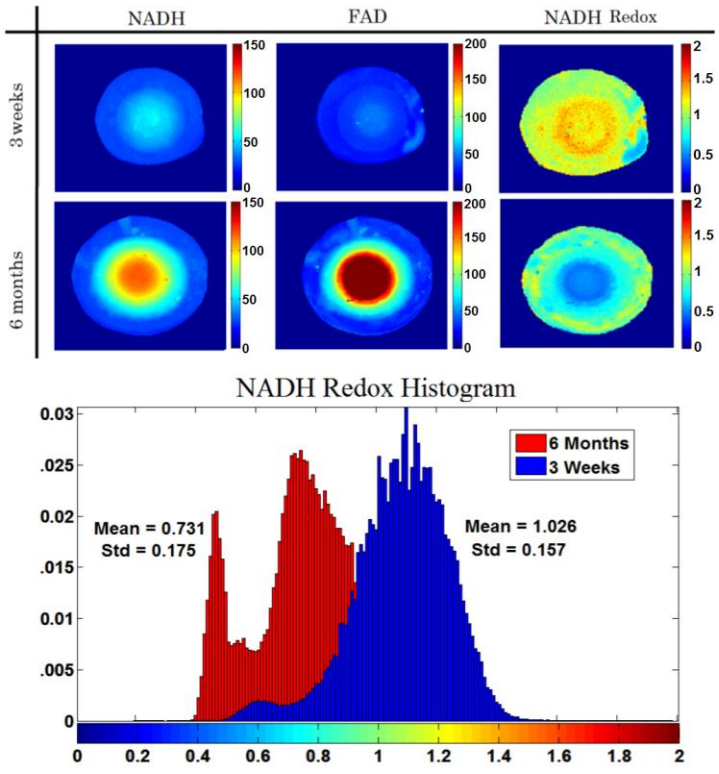

Figure 2-6*:* Increased oxidative stress in diabetic eyes from 3 weeks (non-diabetic) and 6 months (diabetic) old Akita/+ mice. Top: The maximum projected fluorescence images of NADH, FAD, and RR of eyes from 3-week (top row) and 6- month (bottom row) old mice. Bottom: Histograms of RR in eyes of 3-week-old and 6-month-old male Akita/+ mice. Note a decrease in the mean RR in eyes of diabetic mice due to diabetes progression and increased oxidative stress.

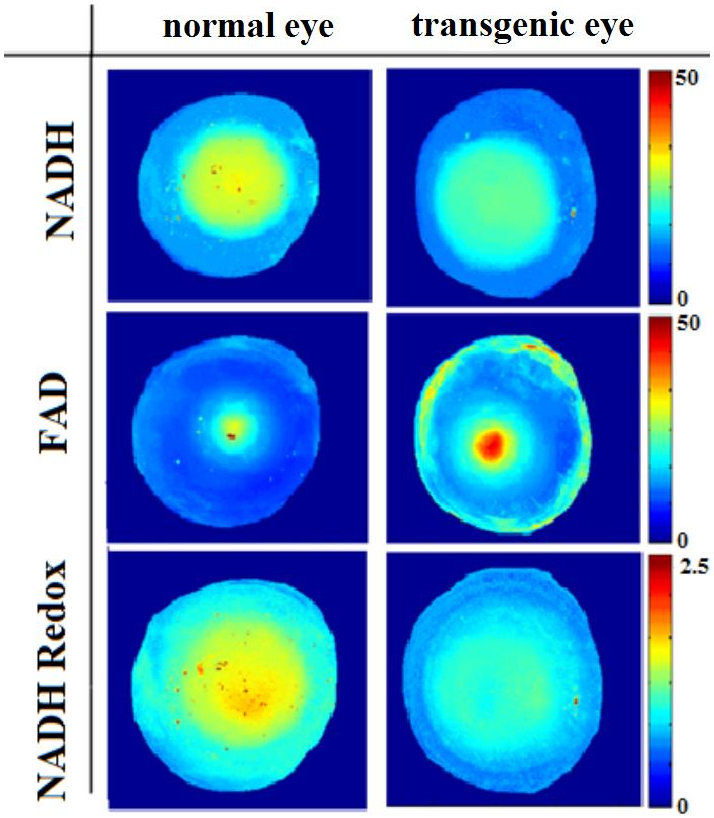

Figure 2-7: Representative max projected NADH, FAD and RR images for eyes from normal and transgenic groups [148].

from transgenic rats (more oxidized) due to oxidative stress. P23H transgenic rats consistently demonstrated increased OS as shown in figure 2-7 by a decreased NADH RR.

Top panel of the figure 2-8 shows the RR histograms of a representative eye in each of the SD normal and diseased groups. In the diseased group, the RR indicates a more oxidized biochemical state with a mean value of 0.821 compared with a higher mean value of 1.079 in SD normal eyes. There is a shift in histograms from the redox of the normal eye to more oxidized state of the P23H transgenic eye and the RR histogram shows a 24% oxidation in the respiratory chain in this group due to increased OS. The bottom panel of the figure 2-8 compares the mean values of the histograms (mean ± SEM, standard error over the number of samples) of max projected

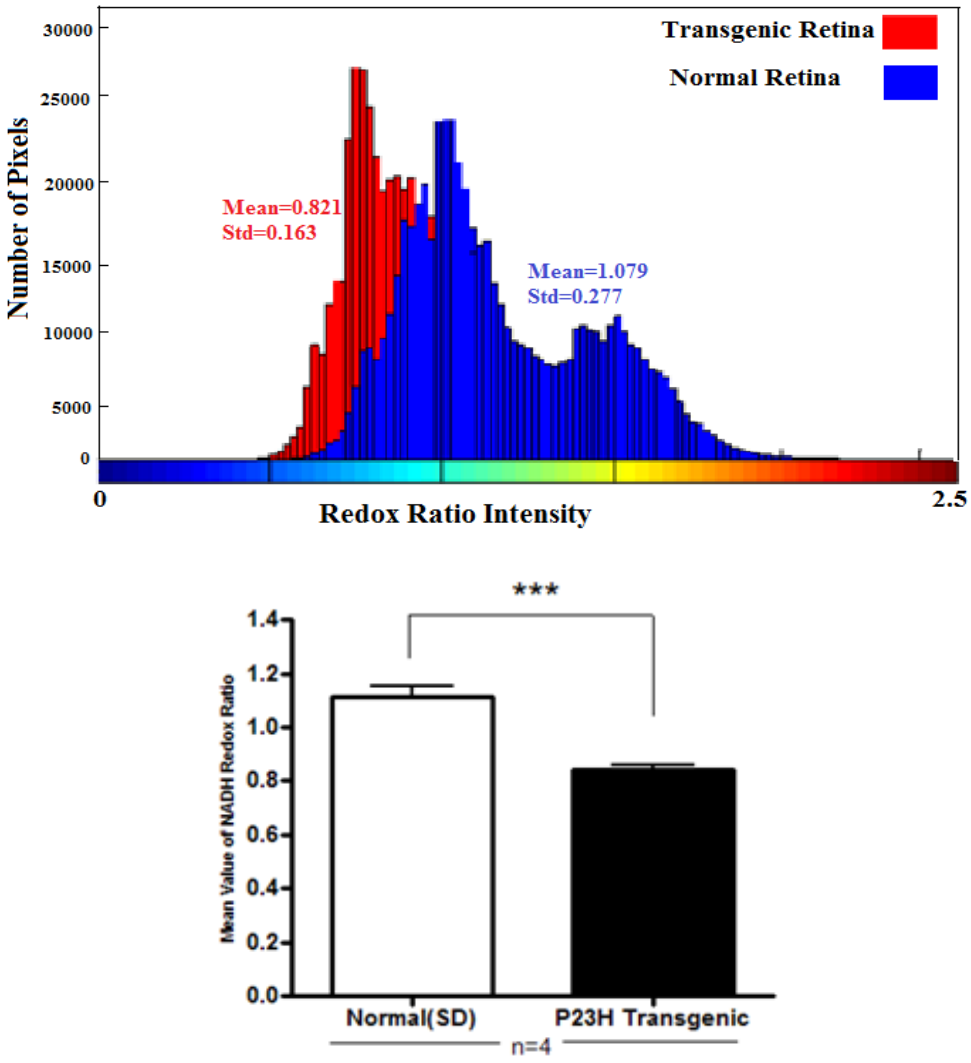

Figure 2-8 [148]: Top: representative histogram for eyes from normal and diseased groups comparing redox ratio intensity between P23H transgenic retina vs. SD Normal retina. Oxidative stress causes more oxidation in the NADH redox histogram. Bottom: bar graph plot comparing the mean values of the histograms of max projected images from SD and P23H transgenic rat eyes. The results show a significant difference between normal and diseased eyes (****P* <.001). Error bars: SEM; *P* values were obtained from unpaired Student's t- test.

images from SD normal and diseased groups. The results show a significant difference (p <0.001) between P23H transgenic eyes versus the SD normal eyes (n=4 in each group) [148].

The effect of the endoglin gene deletion, age and OIR was studied on the eye metabolism. Mitochondrial redox state (FAD RR = FAD/NADH) was determined in eyes from Eng +/- mice and control littermates at postnatal day 21, 6 weeks, and 10 months of age, as well as eyes from

Eng +/- OIR mice and control littermates at postnatal day 17. FAD RR detects changes in the oxidation state of the mitochondrial respiratory chain and can be used as a quantitative marker to evaluate the oxidative stress in diseased and normal eye.

Figure 2-9 shows 3D volume rendering of FAD, NADH, and FAD RR, as well as the FAD RR histogram from a representative retina in each group of (P21, 6W, 10M) Eng+/- mice in comparison with corresponding controls. As described in the image processing section, retinas of mice were segmented from the fluorescent images of eyes captured by cryoimager. As Figure 2-9 shows, retinas from Eng +/- mice exhibit a significant decrease in the mean FAD RR in all three age groups compared to Eng +/+ mice. To better compare the intensity of the FAD RR 3-D rendered images in Eng +/+ and Eng +/- groups, the histograms of FAD RR for each set of retinas were plotted. These histograms display the result in which, in the Eng +/- group, the FAD RR indicates a more oxidized biochemical state compared to Eng +/+. The results presented in the histogram indicate that the mean FAD RR of retina from 6 week-old Eng +/- mice showed a more significant decrease compared with control mice (Eng +/+). There is a blue shift in histograms from Eng +/- versus the Eng +/+ retina. The histogram shows 23%, 33%, and 30% change in P21, 6W, and 10M retinas, respectively.

We also compared the FAD RR in the retina during OIR in Eng+/- and Eng+/+ mice. Figures 2-10 displays the 3-D rendering of FAD and NADH fluorescence signals, and FAD RR as well as the FAD RR histogram from a representative retina of each of the Eng+/- and Eng+/+ mice during OIR. The images show a remarkable decrease in FAD signal and therefore a substantial decrease in the FAD RR of both organ, retina from P17 Eng +/- OIR compared to Eng +/+ OIR.

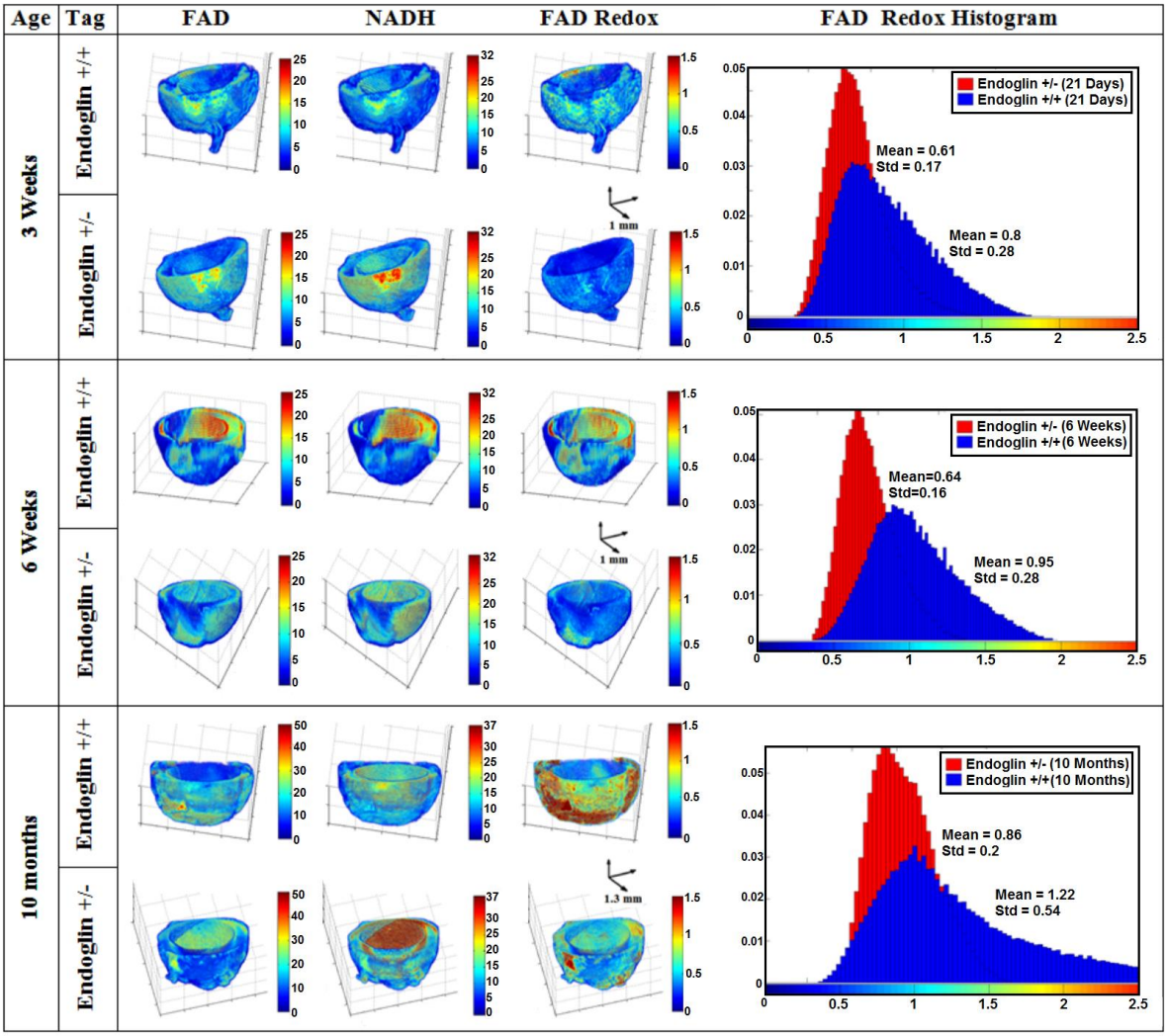

Figure 2-9: Representative 3-D reconstructions of an eye from each of the three groups (P21, 6W, 10M) and their related histograms. From left to right, images shown are FAD, NADH, and FAD redox ratio (FAD RR). The histogram shows 23%, 33%, and 30% change in the mean FAD RR in P21, 6W, and 10M eyes [1].

The presented histograms demonstrate 29%, and 41% change in the mean FAD RR and also 58% and 37% change in the deviation of FAD RR in P17 retina of Eng+/- mice compared to Eng+/+ mice during OIR.

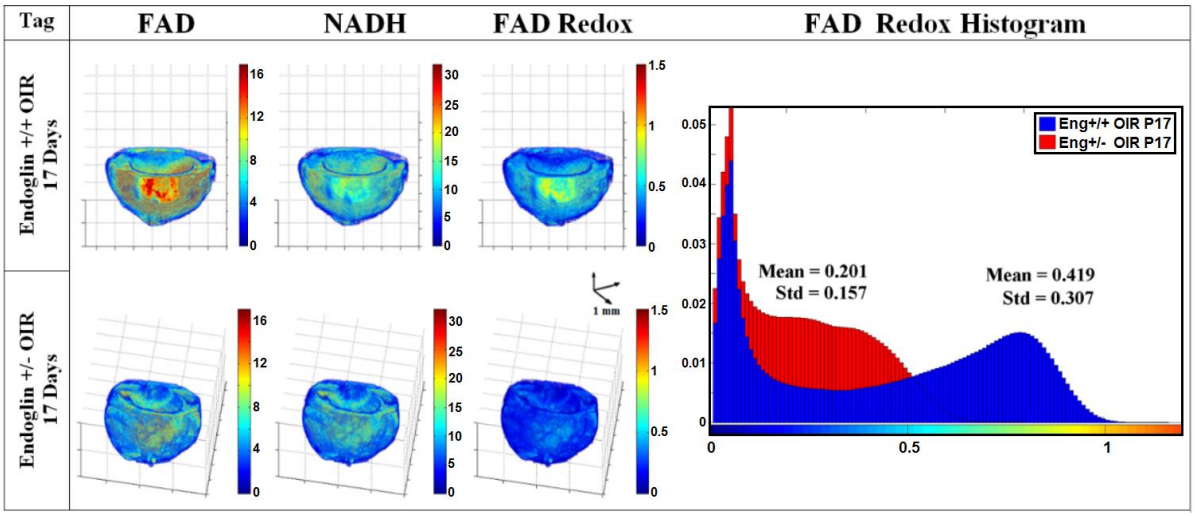

Figure 2-10: Representative 3-D reconstructions of eyes from P17 Eng+/+ mice (first panel) and P17 Eng+/- mice (second panel) during OIR and related histogram (bottom panel). From left to right, images shown are FAD, NADH, and FAD redox ratio (FAD RR). The histogram shows 41% and 37% change in the mean and deviation of FAD RR [1].

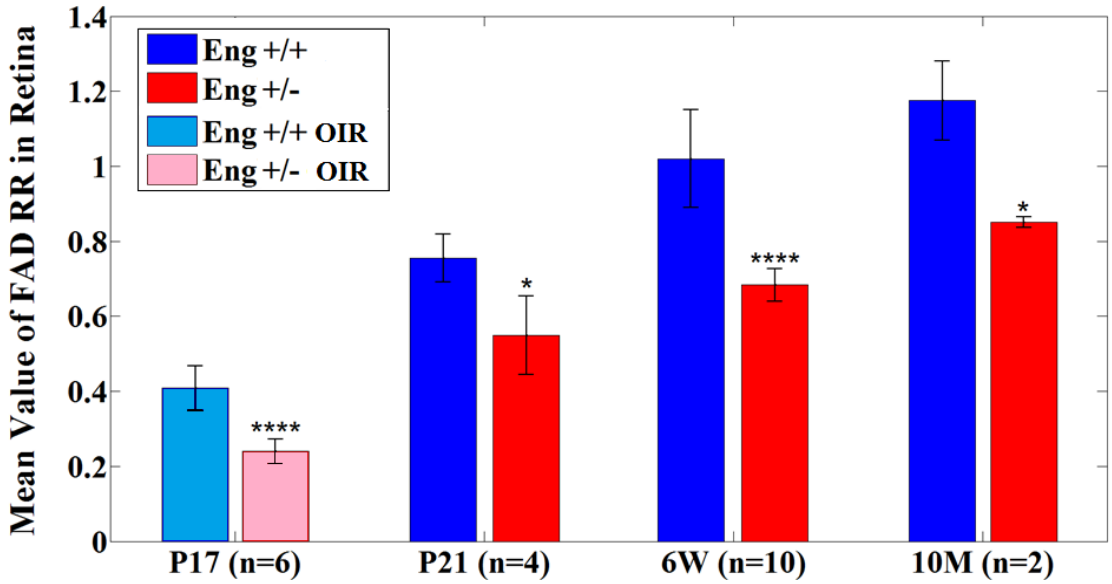

Figure 2-11: Bar graph plot comparing the mean values of the histograms of 3D rendered images from Eng +/- eyes and their respective controls in three different ages and also from Eng+/- and Eng+/+ eyes at the age of P17 during OIR. The results show a significant difference between retinas from P17, P21, 6W and 10M old Eng +/- and Eng +/+ mice (*p <0.05). The most significant change was demonstrated by 6 weeks old Eng +/- compared to Eng +/+ mice and by 17 days old Eng+/- compared to Eng+/+ mice during OIR (****p <0.0001) [1]. P values were obtained from a two-tailed student's t-test.

To evaluate the statistical significance of the results, four eyes in the P21 groups (Eng +/+ and Eng +/-), ten eyes in the 6W groups and two eyes in the 10M groups were imaged. Also three animals and six eyes from Eng +/+ and Eng +/- mice were studied during OIR. The mean values of the histograms of 3-D rendered images were compared, the results of which are represented in Figures 2-11. This figure displays a significant difference in RR of retinas from Eng +/- mice versus their appropriate control, Eng +/+ mice, in three different ages as well as Eng +/- versus Eng +/+ mice during OIR at the age of P17 [1].

2.4 Discussion and conclusion

Oxidative stress and mitochondrial dysfunction can lead to apoptotic cell death early in the pathology of many diseases [161-168] in different organs. Thus, the measurement of mitochondrial metabolic activity could potentially be an early indicator of organ dysfunction during the disease. Our present method measures fluorescence from both NADH and FAD, allowing calculations of the redox ratio, which has proven to be a powerful diagnostic marker independent of the number of mitochondria [1, 28, 29, 148]. Furthermore, this study demonstrates the ability of cryoimaging to measure RR in a small organ like the eye and even in a thin layer of eye, retina.

Fluorescence redox imaging was performed using the cryoimager to determine the changes in ocular oxidative stress and use data to predict progression of different ROS-mediated diseases including, diabetic retinopathy (DR), retinitis pigmentosa (RP), HHT-1, and OIR. To measure the changes in the oxidative stress, mitochondrial redox state was analyzed in mouse eyes suffering from these diseases. The percentage change in the signals was expected to correlate with the severity of injuries in the tissue (injured vs. normal).

Diabetes regulates of apoptosis and vascular function in the retina and pathogenesis of diabetic retinopathy and can eventually lead to blindness. Diabetic retinopathy affects up to 80 percent of all patients who have had diabetes for 15 years or more. Despite these intimidating statistics, much of the damage could be reduced if there was early detection and proper treatment. We demonstrated that oxidative stress and mitochondrial redox state can be considered as the earliest physiological marker of diabetic retinopathy. The experimental results of our studies suggest that diabetic eyes exhibited higher OS, therefore lower redox ratio with progression of the disease. Akita/+ diabetic mice showed a 30% decrease in RR with progression of disease from 3-weeks to 6-months of diabetes indicating increased OS. Diabetic male Akita/+ mice, spontaneously develops type 1 diabetes, and exhibit many signs of early non-proliferative retinopathies seen in humans with diabetes.

In the presence of DR, the coenzymes NADH and FADH2 accumulate in their oxidized forms (NAD and FAD). We therefore anticipated higher concentrations of FAD and lower concentrations of NADH in the injured retina compared to P21 retina which can be considered as a disease free retina. It can be seen from the maximum projection images that the FAD concentration is higher and NADH concentration is lower. This results in the NADH RR showing a significant decrease in the diabetic eye as compared to the control. The difference in the mean values of the two histograms is the result of a shift in the metabolic state. OS caused by diabetes is the reason for this shift in metabolic levels of the eye tissue and causes the mitochondrial respiratory chain to be more oxidized. The 30% oxidation in the RR that we observed in the diabetic eye implies that substantial mitochondrial OS is a significant early cellular event in DR.

In various forms of retinitis pigmentosa (RP), another ocular disease under this study, rod specific mutations are genetically heterogeneous trigger photoreceptor cell death by apoptosis.

Recent studies suggest that death of cone photoreceptors subsequent to rod cell death are due to increased oxidative and nitrosative stress [169, 170]. The retina is particularly vulnerable to oxidative damage since it is a tissue with one of the highest rates of oxygen consumption in the body and about 90% of tissue oxygen is metabolized within the mitochondria [171]. As reported in induced and inherited retinal degeneration models, photoreceptors die due to OS, mitochondrial dysfunction and apoptosis [172]. There are several potential sources of ROS generation in inherited retinal degenerative diseases that may be either caused or exacerbated by reduced oxygen consumption due to the loss or inactivity of mutant rod photoreceptors. Markers of oxidative damage to proteins, lipids and DNA have been detected in cone photoreceptors in the transgenic pig model of RP that suggesting that as the rod photoreceptors degenerate, there is a reduction in oxygen consumption in the outer retina resulting in hyperoxia in the photoreceptor layer with subsequent increase in oxidative stress, resulting in cone loss [171, 173]. Understanding the biochemical mechanisms involved in cone photoreceptor degeneration is important since cone loss is the major reason for visual loss in RP. The above hypothesis is supported by the fact that photoreceptor depletion-induced hyperoxia is a factor that makes the degeneration process progressive as seen in models of retinal degeneration. Increasing evidence supports the therapeutic efficacy of mitochondrial targeted agents including MITO 4565, TUDCA (tauroursodeoxycholic acid), minocycline and cyclosporine A in various models of retinal and neurodegenerative disorders [172-175].

In the presence of hyperoxia, as seen in RP and other inherited retinal degenerations, the mitochondrial respiratory chain is more oxidized and we expect higher concentrations of FAD and lower concentrations of NADH in the P23H retina compared to SD normal retina. This results in a shift in the histogram of the mitochondrial RR toward left. NADH RR shows a significant

decrease of 24% in the degenerating eye as compared to the SD normal. The 24% oxidation in the NADH RR that we observed in the retina of P23H transgenic rat model suggests that mitochondrial RR is an early cellular marker for early detection of retinal OS and so RP.

We observed an increase in signal intensity in the eye samples from the vitreous in both NADH and FAD channels that needs to be further investigated and explained. Changes in the biochemical composition of vitreous following pathological changes in the retina during the degeneration process may be one of the reasons for those isolated signals. Collagen, elastin, flavins and lipo-pigments (ceroid and lipofuscin) are some of the endogenous tissue fluorophores that has excitation emission spectral overlap with NADH [176, 177]. However unlike NADH, collagen and elastin contribution would not be expected to change with variations in mitochondrial redox state [142, 176]. It has also been shown that upon binding to a protein, the quantum yield of NADH increases four fold [178]. Proteomic changes in the vitreous humor have been reported in micro vascular pathologies including proliferative diabetic retinopathy [179].

To exclude the signals from other parts of the eyes including vitreous, the retinal shell was segmented to study the effect of the diseases on retina health. OS and redox state of retina in the models of injuries (HHT-1, in combination with oxygen induced retinopathy (OIR) condition and normal air condition) were also investigated using fluorescent imaging in cryogenic temperatures. Our studies also suggest that mitochondrial oxidative stress can be also detected in retinal layer of mice eyes in the absence of sufficient endoglin expression (animal model for HHT-1). Retinas demonstrated a decrease in FAD signal and, as a consequence, a decrease in tissue FAD RR. This decrease is due to a deficiency in the endoglin protein (Eng +/-), which makes the tissue more resistant to oxidative challenges, yielding a lower RR (33% in eye) compared to their control (Eng +/+). However, diminished oxidative response may be responsible for mitigation of angiogenesis

in these organ, as we have shown in the eye during OIR [95]. The results from the eye of Eng+/- show same direction shift in RR compared to Eng+/+ at all three ages, including 21 days (P21), 6 weeks, and 10 months. The changes in RR were the lowest at P21 mice, then reached its maximum at 6 weeks, but decreased in the 10 month mice. To gain further insight into the physiological role endoglin plays during vascular development and neovascularization, we compared the RR as a marker of oxidative stress in the eyes of Eng+/- and Eng+/+ mice during OIR. Eng +/- tissue exhibited 41% lower RR compared to the Eng +/+, which means it is less oxidized. The noticeable change of FAD RR in the eye during OIR is consistent with significant up-regulation of endoglin expression in retinal vasculature, and enhanced retinal neovascularization in the Eng +/+ mice. These mice showed higher RR than Eng+/- mice which exhibits little or no neovascularization during OIR [95].

The changes of RR in eyes from Eng+/- in comparison with Eng+/+ presented greater value during OIR compared to normal condition. Due to high oxygen-mediated vessel obliterations, the percentage of RR changes in P17 mice during OIR is even bigger than 6W old mice during normal condition. The histogram of RR in the eyes from Eng +/+ OIR is broader than that of Eng+/- OIR. The standard deviation of FAD RR in the eyes of Eng+/+ was 37% higher than that of Eng+/-. These results correspond to influence of enhanced ocular and renal neovascularization in the Eng +/+ mice during OIR.

The results show a significant difference in the mean redox ratio of eyes with and without endoglin haploinsufficiency in both room air and OIR conditions. As expected, the decrease in the FAD redox ratio of the Eng +/- eyes indicated an overall decrease in oxidative stress.

Our data is more consistent with the notion that some level of reactive oxygen species is essential during angiogenesis, and perhaps other cellular activity. A significant decrease in nitric

oxide (NO) level, consistent with decreased expression of endothelial nitric oxide synthase (eNOS) and inducible NOS (iNOS) in Eng +/- EC, was observed in our previous study [95]. Our study here shows reduced oxidative stress in Eng+/- eyes. This is also consistent with reduced sensitivity Eng+/- EC compared to Eng+/+ when challenged under oxidative stress [95]. Therefore, uncoupling of eNOS is an unlikely possibility since Eng+/- EC express less eNOS and exhibit lower oxidative stress. How endoglin deficiency contributes to reduced level of oxidative stress and eNOS expression/function is beyond the scope of the present study and subject of future investigation.

Cytosolic NADPH, which has the same fluorescence characteristics as NADH, could be contributing to the signal attributed to NADH in this study. However, Chance et al. demonstrated that the fluorescence signal originates mostly from NADH in the mitochondria and the contribution of NADPH - present in cytosol - is very small [180]. The fluorescence signal is mainly from NADH since its quantum yield is much higher than NADPH (1.25 to 2.5), its concentration is 5 times larger than NADPH, and is the only one affected by metabolic perturbations [181-183]. Thus, NAPDH contribution to the NADH signal and the change in the NADH signal due to diseases studied in this thesis was assumed to be small and was ignored.

The current study demonstrates the utility of RR to detect ocular injury and mitochondrial OS under cryo conditions that optimize the quantum yields of NADH and FAD. Moreover, we have developed an experimental *in vitro* protocol to measure mitochondrial OS at 37^{o}C using time lapse microscopy and the results using this system is described in the next chapter.

Chapter 3

Microscopy studies of retina and lung cells

in vitro

3 Microscopy studies of retina and lung cells

The structural and metabolic properties of biological tissues could be affected by diseases. The visualization and quantification of changes in cellular structure and metabolic function helps in early detection and progression monitoring of diseases. *Fluorescence microscopy* allows to study both morphological and metabolic changes in biological samples with cellular and subcellular resolution.

In the first part of this chapter, structural changes of the retinal vasculature due to oxidative stress were studied in microscopic images of clinically relevant eye diseases. A multi-parameter quantification method was implemented to quantify early morphological changes due to oxidative stress and injuries [55]. This method was applied to wholemount retinal trypsin digest images of diabetic Akita/+, and Bcl-2 knocked out mice models [55]. Unique features of retinal vasculature were extracted to monitor early structural changes and retinopathy, as well as quantifying the disease progression. These features include number of vascular cells, population ratios of endothelial cells to pericytes (an indicator of pericyte loss), fractal dimension, vessel coverage, and number of acellular capillaries. Current gold standard method for measuring all of these parameters is the tedious process of manual counting and analysis which is prone to errors. Quantification using the method presented in this chapter will be helpful in evaluating physiological and pathological retinopathy in a high throughput and reproducible manner. Moreover, the implemented software is able to identify diabetic retina and normal retina based on the quantified parameters [55].

In the second part of this chapter, cellular metabolic changes associated with oxidative stress (metabolic and oxygen stress) and injuries (Persistent Pulmonary Hypertension; PPHN) is presented in live lung cells. Utilizing *time-lapse microscopy* in combination with an experimental

protocol I developed for live cell imaging, the dynamics of the reactive oxygen species (ROS) production was assessed in pulmonary artery endothelial cells (PAECs). ROS play a vital role in cell signaling and redox regulation but when present in excess, lead to numerous pathologies. The aim of this *in vitro* study was to assess mitochondrial $O_2^{\bullet-}$ production in PAECs over time using a novel quantitative approach. The rate and sources of $O_2^{\bullet-}$ production were assessed using targeted metabolic modulators of the mitochondrial electron transport chain (ETC) complexes, specifically mitochondrial complexes' uncouplers and inhibitors, and inhibitors of extra-mitochondrial sources of $O_2^{\bullet-}$. After stabilization, the cells were loaded with mitochondrial-targeted hydroethidine (Mito-HE, MitoSOX) to monitor the production of $O_2^{\bullet-}$. Time-lapse fluorescence microscopy was used to monitor the dynamic changes in $O_2^{\bullet-}$ production over time. This novel method can be applied in other studies that examine ROS production from different mitochondrial ETC complexes during ROS-mediated injuries *in vitro*.

This chapter covers both the retina and lung cell fluorescence microscopy in details and discusses the results obtained by the developed methods.

3.1 Microscopy of retinal injuries

Retinopathy involves diverse vascular complexity and other changes in the neuroretina associated with the pathogenesis of many ocular diseases including diabetic retinopathy [63], hypertension [184], and age related macular degeneration [185]. Once the degree of retinopathic injury can be detected, it will be possible to treat and slow down or stop its progression. Therefore, creation of a system with multi-parameter diagnosis of retinal structural changes in their *early stages* is a high priority and helpful to investigate the pathogenesis and progression of retinopathy.

Recent studies have reported image procedures on retinopathies [186-190]. However, none of these methods consider more than one feature to classify the retina as either healthy or injured. For example, there are studies using computer-assisted procedures to measure the caliber of retinal blood vessels as a feature of retinopathy [191-194], and most of these procedures are semi-automatic. In addition, many of these studies analyzed fundus images, which typically lack high resolution details.

High resolution microscopy images of the retinal trypsin digest slides allows for quantifying the clinically relevant features of the retinal vasculature, the majority of which cannot be studied in low resolution fundus images. Wholemount retinal trypsin digest, which is the gold standard method for analyzing the diabetic retinal vasculature [195, 196], makes it possible to study various structural changes such as capillary degeneration, vascular cell apoptosis, and microaneurysms [197]. The first two abnormalities are correlated with changes in retinal vasculature during early stages of diabetes, hypertension [198], and also are seen in mice with Bcl-2 deficiency. The Bcl-2 expression plays an important role in regulating apoptosis and angiogenesis, and its deficiency is associated with decreased number of vascular cells and vascular density in the retina [70].

We have developed a multi-parameter image cytometry tool to quantify the parameters associated with the *early stages* and *progression* of retinopathic injury during diabetes. Using this tool, two different vascular cell types, endothelial cells (EC) and pericytes (PC) can be segmented and the number of each cell type quantified and the ratio of EC to PC (EC/PC ratio) calculated. The presented tool also determines other retinal vascular parameters including the number of acellular capillaries, vessel coverage, and fractal dimension, all of which correlate with progression of diabetic retinopathy [199-201]. To the best of our knowledge, this is the first time that automatic

multi-feature quantification of diabetic retinopathy and vascular changes in retinal trypsin digests has been presented. Our quantification method measures *subtle* retinal vascular changes, which are markers of *early* microvascular dysfunction during diabetes. Such developments will open the door for advanced quantitative assessments, which could substantially contribute to a better understanding of the pathogenesis and prediction of diabetic retinopathy. Moreover, our cytometric tool selects two, three or all of the detected parameters depending on the disease stage, and utilizes classification techniques to separate healthy and injured retina. This tool allows for automated analysis of retinal trypsin digest preparations for high throughput assessment of structural retinopathy changes when needed.

The following sections covers how the samples are prepared, how the experiment is conducted and the obtained results will be discussed.

3.1.1 Injury model

In this study, retinal vascular parameters are compared in diabetic mice (6 months and 11 months of age) and bcl-2 deficient mice (6 weeks of age) with their corresponding wild types. Akita/+ mice (Jackson Laboratory, Bar Harbor, ME) have a mutation in their insulin gene, and the heterozygous male (Akita/+) mice become diabetic by 4 weeks of age. The retinas from these mice show differences in cell distribution and vasculature complexity [145]. They also show the growth of acellular capillaries, which are vessels that contain no cell nuclei, with long-term diabetes. These vessels are very thin and are a common hallmark of non-proliferative diabetic retinopathy.

The germline targeting of the Bcl-2 gene and the generation of mutant mice have been previously described [202]. Litters produced by mating heterozygote mutant mice are genotyped by PCR of genomic DNA extracted from tail biopsies. Bcl-2 -/- mice exhibit decreased retinal vascular density during development of retinal vasculature prior to 6 weeks of age. Decrease in

retinal vascular density is mainly attributed to decreased numbers of endothelial cells and pericytes in the absence of bcl-2 [70].

Retinal trypsin digests from diabetic Akita/+ mice, Bcl-2 deficient (Bcl-2-/-) mice, and wild type (WT) mice were prepared and imaged. These studies were conducted in accordance with the ARVO Statement for the Use of Animals in Ophthalmic and Vision Research, and approved by the Institutional Animal Care and Use Committee of University of Wisconsin School of Medicine and Public Health.

3.1.2 Microscope slide preparation

A total of 14 mice were sacrificed, including three 6 week-old bcl2-/- and their wild type (WT) littermates, two 6 month-old diabetic Akita/+ and their WT littermates, two 11-month-old diabetic Akita/+ and their WT littermates. Retinas (n=28) of these six groups of mice were digested in a solution of trypsin, which carefully leaves retinal vascular network intact while digesting other tissues. Following the digestion, retinal vascular preparations are mounted on charged microscope slides, dried, stained with periodic acid-schiff (PAS) and hematoxylin, and coverslipped for virtualization and quantitative assessments, as previously described [203].

3.1.3 Fluorescence microscopy

A Nikon Ti-E inverted microscope used for the retinal vasculature studies. It includes four fluorescent interchangeable filter cubes in addition to the standard DIC and bright-field channels. It is commonly used to study normal cell processes as well as those of diseases, cell signaling, neurobiology, molecular pathology, and so on in cellular and sub-cellular resolution.

Bright field images were acquired using an overhead halogen lamp, whereas the fluorescent images use a mercury arc lamp, to take advantage of its intense peaks in the ultraviolet range. The images were captured using a charge-coupled device (CCD) camera (Q-imaging, Aqua Exi, 14 bit,

6.45μm per pixel) with exposure time (0.68 μsec/pixel in red channel) set to ensure proper use of the dynamic range of the camera, while avoiding saturation and photo bleaching. The filter set in the blue and red channels filters excitation spectra at 340-380 nm and 528-553 nm, respectively with emission spectra at 435-485nm and 590-650nm, respectively [204].

The retinal trypsin digests were imaged at a magnification of 40× with a scale of 0.16μm per pixel. The images were captured using the Qimaging camera with a field of view (FOV) of 1392 x 1040 pixels. Red fluorescence filter set with excitation at 540 nm (25 nm bandwidth) and the emission at 620 nm (60 nm bandwidth) was used. Images obtained under these settings captured the vasculature network of the retina (Figure 3-1; left image). Besides fluorescence imaging, bright field imaging was performed to capture cell nuclei images (Figure 3-1; right image). Four fields of view were chosen from each group of retina. The fields of view were chosen from the mid-periphery and far-periphery areas of the retinas, one FOV in each quadrant of retina. The acquired images were saved as TIFF files and analyzed in MATLAB (MathWorks, Inc.).

3.1.4 Image processing

This subsection explains how to extract the various investigated parameters from the captured images and go through the details of the developed multi-parameter image processing tool.

- **Cell Detection and Count**

The image processing program detects two vascular cell types, EC and PC from the retinal cell image (Figure 3-2b, left image; captured in bright field). The contours of the cell nucleus in each image are determined using the segmentation algorithms (shown in Figures 3-2a) based on the active contour method.

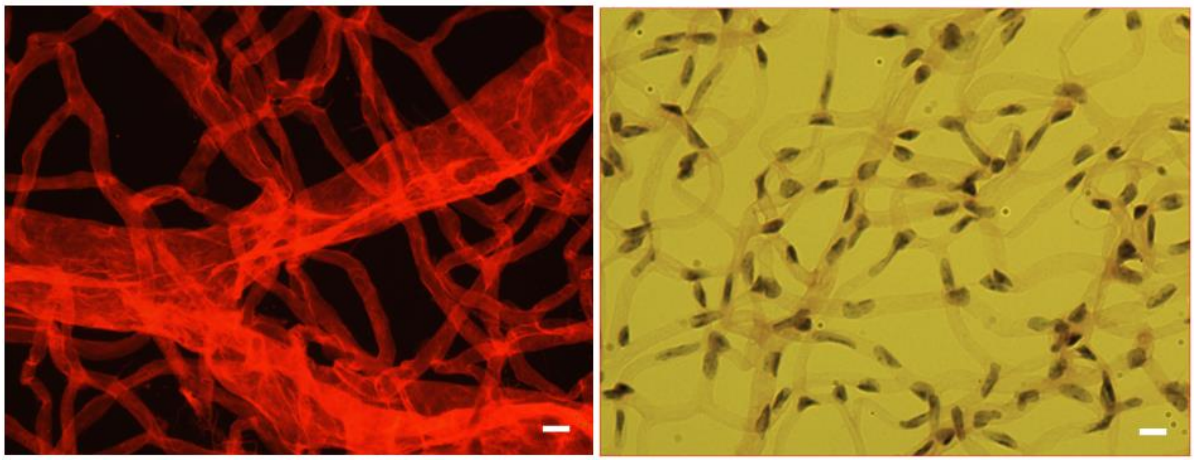

Figure 3-1: High resolution microscopy images of a typical mouse retinal vasculature trypsin digest. Retinal vasculature (left panel) and cell nuclei (right panel) images acquired from different FOVs to detect changes in retinal vasculature and vascular cells (scale bar represents 15 μm).

Active contour technique segments the nuclei of these vascular cells by evolving a level set curve which moves toward the nuclei boundaries by minimizing an energy function. Edge-based active contour is sensitive to the initialization of the level set function (initial image) and hardly stops at the right boundaries of the cell nuclei with non-homogenous intensity and weak edge. Therefore, region based active contour [205, 206] was applied, using the Mumford and Shah segmentation model [205].

To decrease the processing time, level set function was initialized to a binary mask (Figure 3-2b, middle panel, top image) which was resulted from FIR convolution of the original cell image and then adaptive thresholding of the convoluted image (will be discussed later). Using this mask, level set curves converged to the final contour after 100 iterations.

Regular model of active contour can only segment cells whose locations are far away from each other. If the cells are clustered together, this model will fail to segment individual cells. After detecting the boundary of the cell cluster, the front stops moving, no matter how many iteration steps are used, it is impossible to segment individual cells from the group. To improve the segmentation of the clustered cells, the gradient of the cell image (Figure 3-2b, middle panel,

bottom image) was considered as the input image of the active contour program. The gradient image enhances the edges of the cells and decrease the segmentation error due to clustered cells. Last stage of the Figure 3-2b shows the output of the active contour algorithm which is a binary mask containing the borders of the cells.

As mentioned earlier, a spatial finite impulse response (FIR) filter [207] was applied to enhance the object-background contrast [208] of the image and provide a high quality binary mask for the active contour algorithm after adaptive thresholding. For image *g(x,y)*, class *c(x,y)*, and spatial FIR filter *k(x,y)*, the contrast enhancement procedure is:

$$f(x,y) = k(x,y) * g(x,y)$$
$$C(x,y) = \begin{cases} \mathrm{C}_0, & f(x,y) < T \\ \mathrm{C}_1, & f(x,y) \geq \mathrm{T} \end{cases} \quad (3\text{-}1)$$

where * is the convolution operator, *f(x,y)* is the filtered image, C_0, and C_1, represent the two classes of the filtered images, and *T* is the threshold. *T* was initialized using Otsu method [209] to minimize the weighted sum of the intensity variance within each of the pixel classes (C_0, and C_1). Then using adaptive thresholding [210], the threshold level for each pixel is optimized based on the intensity statistics of a local neighborhood surrounding the pixel. Function *C(x,y)*, is a two-category linear classifier implemented as a spatial FIR filter. Given an ideal classified image $i_c(x,y)$ and the input image *g(x,y)*, the optimum FIR filter that maps *g(x,y)* to $i_c(x,y)$ is obtained.

$$e(x,y) = \sum \begin{cases} \left(\mathrm{i}_\mathrm{c}(x,y) - f(x,y)\right)^2, & A < f(x,y) < B \\ 0, & otherwise \end{cases} \quad (3\text{-}2)$$

Where error *e(x,y)* is nonzero only when the filter has not acquired the contrast defined by [*A*, *B*]. Minimization of *e(x,y)* results in a filter *k(x,y)* that yields the best contrast for successive thresholding within [*A*, *B*].

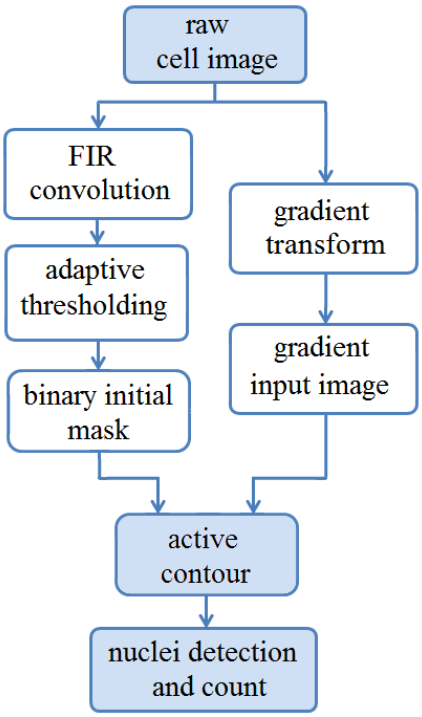

(a)

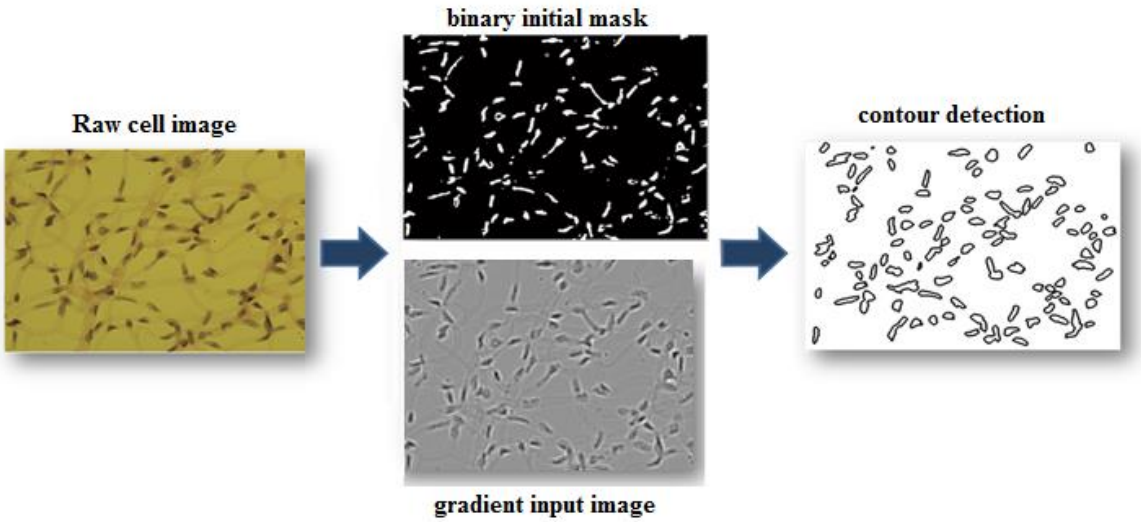

(b)

Figure 3-2: a) Flowchart of the cell segmentation procedure. b) Output of the segmentation algorithm in different stages.

- **Determination of Cell Type and Calculation of the EC/PC Ratio**

Nuclear morphology was used to distinguish between pericytes (PC) and endothelial cells (EC). Pericytes have a round nuclei and protuberant position, whereas endothelial cells have a more elliptical shape. Since pericytes are more round in shape, the ellipticity of the cell is used as a parameter to determine whether a cell is EC or PC. In short, the diameter of the cell was measured for each pixel in the cell border by determining the distance between the pixel and a pixel exactly half way around the border of the cell. The ratio of the largest diameter to the shortest was then stored as the ellipticity of the cell. Cells with ellipticity greater than 2 were categorized as EC, and all other cells were categorized as PC. The threshold value of 2 is found empirically to best correlate with the results of expert analysis.

To evaluate the accuracy of the proposed nuclei segmentation and cell type determination, sixteen FOVs (Field of Views) of four retinas from 11 month-old WT mice were considered that covered over 1000 nuclei. Since there is no ground truth for the segmentation, manual evaluation was used as a benchmark, and we compared the automatic approach to this manual benchmark for accuracy counts (Table 3-1).

- **Acellular Capillary Detection and Count**

The number of acellular capillaries is another parameter of interest. These are also referred to as ghost vessels that are a sign of later non-proliferative complications of diabetes. Acellular capillaries are those blood vessels, which have no cell nuclei and lack perfusion, and as a result have smaller widths than healthy capillaries (Figure 3-3a; white arrow). The program measures the caliber of the vasculature using binary image (Figure 3-3b) and marks areas, which have a width less than 40% of the average width of vessels in the retina (Figure 3-3d). Using morphological tools, the connection of the pixels in the marked areas in a small neighborhood was

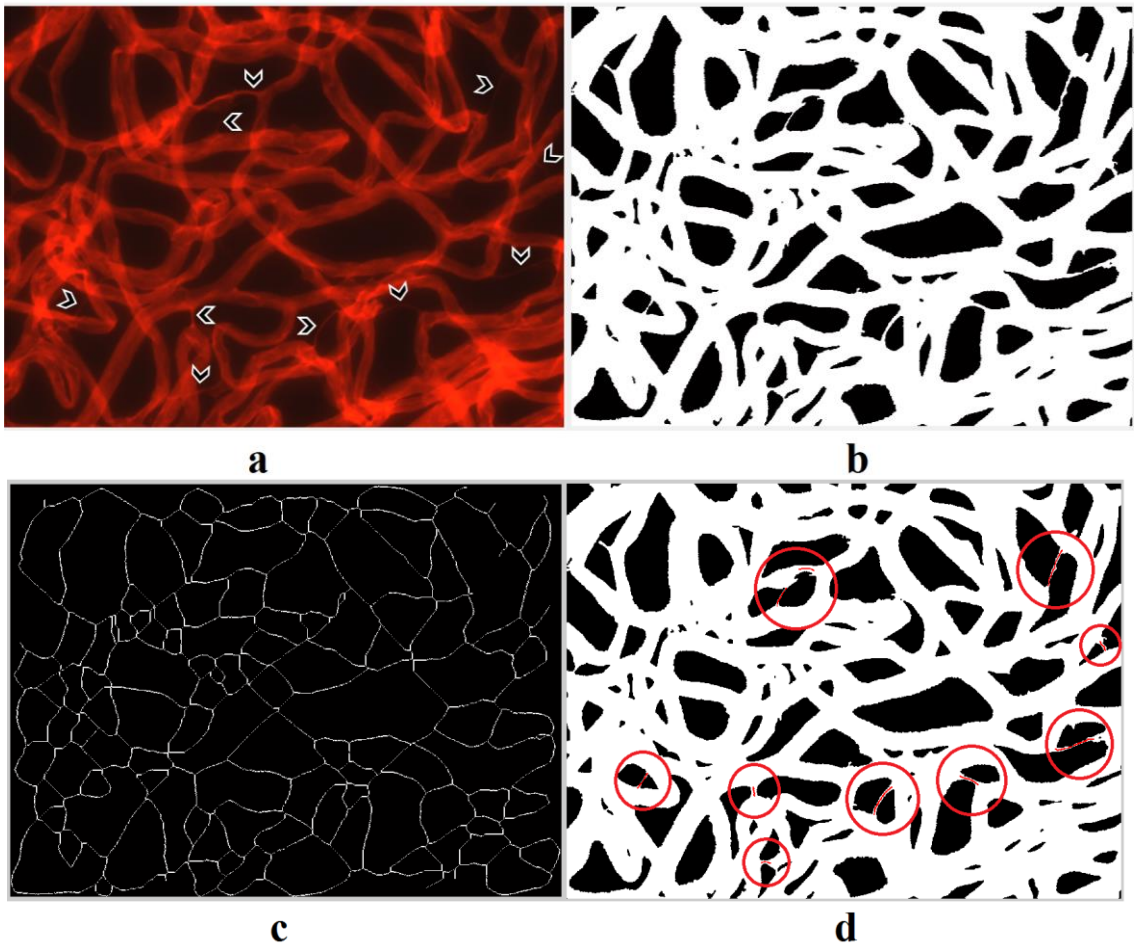

Figure 3-3: Acellular capillary detection: a) vasculature image, b) binary image of vasculature, c) morphological thinning of vasculature used to determine vessel caliber, d) marked connected areas with a width less than 40% of the average vessel's caliber

then investigated. Capillaries with a diameter smaller than 20% of adjacent capillaries were identified as strands or touching vessels and were not counted.

To determine the vessel caliber, defined as the average width of vessels, the total area of the vasculature from the original binary image was divided by the total length of the vessel. The total vessel length was determined using the morphologically thinned vasculature. A skeleton-based method [211] was applied to achieve the thinned vasculature image. In this image, the entire vasculature was reduced to a cross-sectional width of 1 pixel (Figure 3-3c). Thus, the total number of pixels representing the vasculature is equal to the total length of all vessels within the retina.

The performance of the acellular capillary detection algorithm is dependent on the quality of the binary image containing the retina vasculature and acellular capillaries. This binary image is implemented by dynamic local thresholding. The threshold level was initialized applying mixture models method [212] and then fine-tuned locally for each 32×32 neighborhood within the image to detect very thin acellular capillaries.

- **Determination of Fractal Dimension**

Fractal dimension of the retinal vasculature is another parameter quantified using a technique known as the box-counting method [213-216]. In this method, the vasculature image was first divided into a number of smaller "boxes". Then, the number of boxes which contain part of the vasculature was determined. This process was then repeated with boxes of different sizes. If the structure is in fact fractal, an exponential relation is expected between the box size (ε) and the number of boxes required to cover the entire structure (*N*). Equation 3-3 shows this relationship:

$$N = C\varepsilon^{-D_f} \tag{3-3}$$

where *C* is a constant of no consequence in this context, and D_f is the fractal dimension of the structure. The fractal dimension is found by solving equation 3 to obtain an expression involving a logarithm with base ε. However, while equation 3-3 will work for a true fractal, physical structures do not exhibit fractal behavior on all scales. Thus, the limit of the equation 3-3 must be taken as the box size approaches zero. To do this effectively, L'Hopital's rule can be used to determine the limit of the equation based upon the equation's derivative. The fractal dimension can then be found by determining the slope of the log-log plot of *N* against ε (equation 3-4).

$$D_f = -\lim_{\varepsilon \to 0} \log \frac{N}{\varepsilon} = -\frac{\partial(\log \frac{N}{\varepsilon})}{\partial \varepsilon} \tag{3-4}$$

- **Vessel Coverage**

One of the markers of late-stage retinopathy is a denser vasculature. Total vessel coverage is determined for each field of view by the total number of pixels representing the vasculature in the binary image.

3.1.5 Injury classification

The quantified parameters of the cell and vasculature images of the retinas were used to classify retinas as normal or injured. Classification was performed using a nonlinear classifier, support vector machine (SVM). SVM classifier attempts to maximize the margin of error and allows for better generalization of the results [217]. This Kernel-based classifier uses radial basis functions and the kernel trick to project the data into a high dimensional space for easier separation. Gaussian radial basis function was used in the current study to map the training data set into kernel space where a maximal separating hyperplane was constructed.

The accuracy, sensitivity and specificity of the classification are calculated through the following equations:

$$\text{Accuracy} = \frac{TP+TN}{TP+TN+FP+FN}$$
$$\text{Sensitivity} = \frac{TP}{TP+FN} \qquad (3\text{-}5)$$
$$\text{Specificity} = \frac{TN}{TN+FP}$$

where TP and FN are the number of diabetic retinas classified as diabetic or normal, respectively. Similarly, TN and FP are the number of normal retina detected as normal or diabetic. FN and FP were determined using the leave-one-out cross-validation method [218]. In this method, one data point is withheld from the system during its training phase, and then the point is classified using the newly trained system.

3.1.6 Results

In the present study, we have established an image analysis tool to assess and quantify the structural changes in the retinal vasculature either at the early stage of the disease or as the injury progresses. To determine the effect of diabetes and germline deletion of Bcl-2 on the retinal vasculature, five parameters were quantified in retinas from Bcl2 -/- mice and their control littermates at 6 weeks of age, as well as retinas from Akita/+ mice and control littermates at 6 and 11 months of age. The results of this method demonstrated a 26.43%, 16.6%, and 25.7% fewer number of cells and 12.38%, 14.97%, and 17.8% lower vessel coverage in the three aforementioned groups of the diseased retina compared to the corresponding controls. Both groups of diabetic retinas at 6 and 11 months of age showed higher EC/PC ratio compared to their controls (38.7% and 33%, respectively) and only 11 months old diabetic retinas showed significantly larger number of acellular capillaries (126.3%) and higher fractal dimension (1.1%) compared to the control. The details of the results for the 11 month-old diabetic retinas, developing changes in the five features, is provided in figure 3-4.

All the quantified parameters were statistically investigated using two tailed Student's *t*-test (n=16 FOVs for each group). A p value < 0.05 was considered significant.

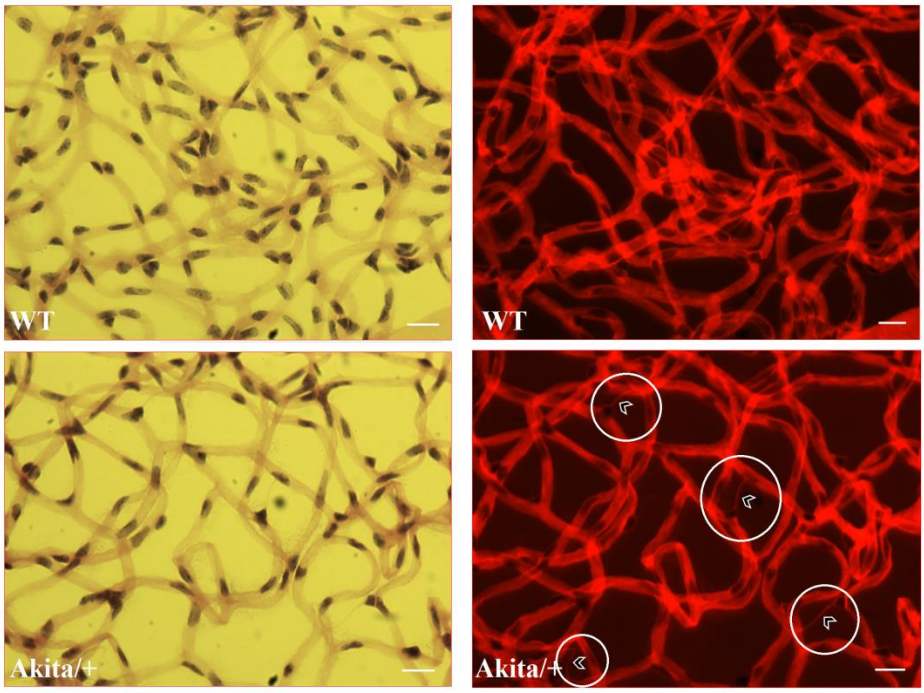

a

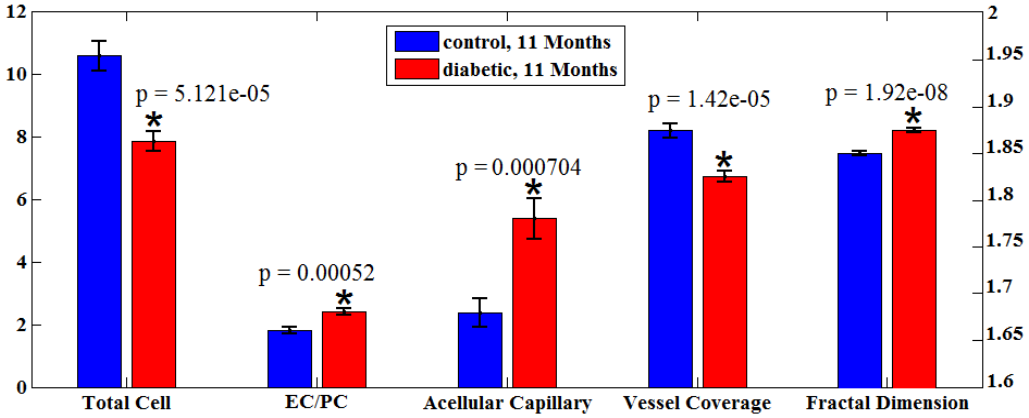

b

Figure 3-4: a) Left: cell images represent that an 11 month-old diabetic retina has a fewer number of cells compared to the normal retina at the same age. Right: vasculature images demonstrate lower vessel coverage and larger number of acellular capillaries (shown by arrows) in a diabetic retina as compared to control (scale bars represent 20μm). b) Bar graph plot comparing five unique features in a diabetic retina versus a normal retina from 11 month-old mice. Bar graphs show the mean values and standard errors of each feature detected in retinas. Diabetic retinopathy resulted in *significant* decrease statistically in the total number of vascular cells, and vessel coverage while increase *significantly* the EC/PC ratio, number of acellular capillaries and fractal dimension. Please note that the total number of cells and vessel coverage were scaled by 10^{-1} and 10^{-5}, respectively. For showing the difference between the fractal dimensions of the two groups, this parameter was presented with different y axis on the right. The number of the fields of view in each group of retina is 16.

- **Injured Retinas Have Fewer Number of Cells**

The retinas from diabetic mice contained fewer cells compared to the wild type normal mice of the same age (Figure 3-4a; left panel). For instance, the 11-month age group images from mid-periphery and far-periphery areas of retina (sixteen FOVs) contained a mean number of 78.5 cells in diabetic mice and 105.6 in the wild type mice (p = 5.1205e-05). The first two bars in Figure 4b represent the mean and standard errors of the cell counts scaled by 10-1 within each group. The higher mean values in the wild type groups showed that the diabetes caused vascular cell death in the retina. Please note that cell segmentation algorithm resulted in an accuracy of 91.4% compared to manual cell count (Table 3-1).

- **Diabetic Eyes Have a Higher EC/PC ratio**

One of the hallmarks of early *diabetic retinopathy* is loss of PC. With progression of the disease, retinal vessels lose *PC, leading to vascular dysfunction such as increased permeability and loss of EC.* Thus, loss of PC results in a higher EC/PC ratio in diabetic retinas compared with retinas from wild type mice. The images showed a mean EC/PC ratio of 2.4053 for diabetic 11 month-old mice and 1.8084 for the wild type mice (p = 5.1772e-04). As expected, the mean values were lower in wild type groups than those in the diabetic groups. Figure 4b shows the mean and standard errors of the EC/PC ratios within each 11 month-old group. PC determination algorithm resulted in 87.87% accuracy in the EC/PC ratio on average compared to manual evaluation (Table 3-1).

Table 3-1: Accuracy of the cell count and cell type determinations for 16 FOVs of images from four 11 month-old WT mice.

Approaches	EC count	PC count	Cell count	E/P	Cell count accuracy	E/P accuracy
manual	1161	688	1849	1.69	100%	90%
proposed	1071	619	1690	1.73	91.4%	87.87%

- **Diabetic Retinas Have a Larger Number of Acellular Capillaries**

Acellular capillaries in the retina arise from chronic exposure to hyperglycemia, have no cell nuclei and exhibit a very small width. The results from the vasculature images (from mid-periphery and far-periphery areas of retina) showed a significant difference between the number of acellular capillaries in the wild type and Akita/+ 11 month-old mice (Figure 3-4a; right panel). The mean acellular capillary number were 2.375 and 5.375 for wild type and Akita/+ mice, respectively (p = 7.0414e-04). Figure 3-4b displays the mean value and standard errors of the number of acellular capillaries.

- **Injured Retinas Have Lower Vessel Coverage**

Our results indicated that the total area of the vasculature in the retinas from diseased mice was smaller compared to wild type mice (Figure 3-4a; right panel). The mean values of the number of pixels representing the vasculature were 672050 and 817790 for diabetic and wild type non-diabetic 11 month-old mice, respectively (p = 1.4214e-05). Figure 4b shows the mean and standard error of the vasculature area scaled by 10^{-5} for each group.

- **Diabetic Retinas Exhibit Greater Fractal Dimension**

Our studies reveal a difference between the fractal dimensions measured in the retinal images of diabetic and non-diabetic 11 month-old mice. The mean values of the fractal dimension were 1.8733 and 1.8499 for diabetic and non-diabetic mice, respectively (p = 1.9167e-08). Figure 3-4b shows the mean and standard error of these samples, illustrating a significant difference between the two groups. These results suggest that greater retinal fractal dimension, representing increased geometric complexity of the retinal vasculature as a sign of chronic diabetic retinopathy.

- **Classification of Retinal Images Resulted in 85% Accuracy**

Table 3-2 provides classification results with different feature combinations. Features were selected based on the type and duration of the disease. Left panel in figure 3-5 shows the distribution of two features (cell count and vessel coverage) as an example of the classification using SVM classifiers. Crosses correspond to Bcl-2 deficient retinas and stars are related to normal retinas (control). The hyperplane on the top right corner is one of the classifiers that indicates the decision boundary between the two groups. This classification resulted in 85.4% accuracy, 94.8% sensitivity, and 77.5% specificity. The right panel in figure 3-5 represents the SVM classifier using three features including cell count, vessel coverage, and EC/PC ratio. The surface between yellow (diabetic) and blue (normal) regions is one of the classifiers, which makes the decision boundary between the two groups. Using these three features yielded in classification with 85.3% accuracy, 88.8% sensitivity, and 81.7% specificity.

Table 3-2: Performance of the SVM classifier for different groups under study.

Disease	**Age**	**Features**	**accuracy**	**sensitivity**	**specificity**
Bcl-2 deficiency	6 weeks	cell count, vessel coverage	85.4	94.8	77.5
Diabetes, Akita/+	6 months	cell count, vessel coverage, EC/PC	85.3	88.8	81.7
	11 months	cell count, vessel coverage, EC/PC, acellular capillary count, fractal dimension	75	71.7	81.7

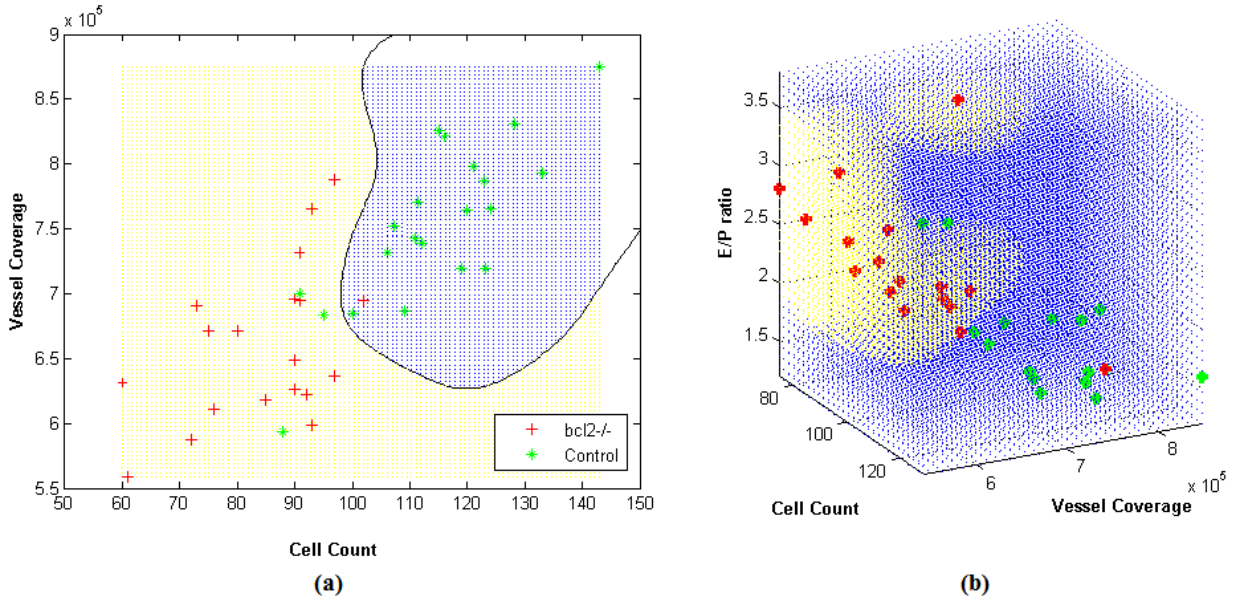

Figure 3-5: Results of the classification using SVM method in retinas from a) 6 weeks bcl2-/- deficient and WT mice considering two features: cell count and vessel coverage b) 6 months diabetic Akita/+ and WT mice with three features: cell count, vessel coverage, and EC/PC ratio; Red crosses correspond to injured retinas and green stars are related to control. The boundary between yellow (injured) and blue (normal) regions is one of the classifiers.

3.1.7 Discussion and conclusion on the retina study

We have developed a novel multi-parameter quantification method to evaluate the health of retinal vasculature. This method employs image processing algorithms to detect the retinal parameters of interest including vessel coverage, acellular capillary count, fractal dimension, and vascular cell count and cell type. To validate the use of the proposed method, we compared the accuracy of the nuclei segmentation and cell type determinations with manual evaluations. Accuracy counts were divided into two categories: EC counts and PC counts. Based on these two counts, the total cell count and EC/PC ratios were evaluated and shown in Table 3-1. The total number of nuclei identified by each method was not the same. Overall, nuclei segmentation algorithm resulted in an accuracy of 91.4% compared to *manual* cell counting. The main source of error in the cell count was under-segmentation problem occurred due to overlapping cell nuclei.

Segmentation of images containing touching and overlapping cell nuclei is a challenge in cell segmentation [219, 220], and further investigation is needed to further reduce this error.

It should be also noted that EC counts and PC counts assessed by each method were not the same. For computer-based approach, the most common error is the under-segmentation, while for manual segmentation, the discrepancy on whether to identify certain nuclei as EC or PC play a much larger role in accuracy rate. The inconsistency between the manual evaluations of cell type provides an idea of how well one could expect to do in comparison to the chosen standard. If two experienced biologists can only agree on 90% of the cell type results, then it is likely that any claim of above 90% for automatic cell type detection is just accidental. Our results suggest that performance of the proposed method for determining the cell type is comparable to manual evaluation. Considering the manual segmentation accuracy of around 90%, which is only 2.13% better than automatic segmentation method, our results reflect the overall difficulty of the problem and indicate good performance for the automatic method.

The presented multi-parameter quantification method is able to analyze and monitor vasculature complexity in rodent models of diabetic retinopathy and Bcl-2 deficiency. Cell apoptosis [221-225], loss of pericytes [226-230], and lower vessel coverage are used to assess early signs of non-proliferative diabetic retinopathy. However, increased number of acellular capillaries [201, 228] and higher fractal dimension [231-234] were later complications and become more numerous with progression of diabetes. Diabetic retinopathy is a progressive disease and goes through all of these changes in a timely manner. Loss of pericytes is an early event, which is followed by vascular dysfunction, loss of EC, formation of acellular capillaries and microaneurysms, ischemia, and ultimately neovascularization that is the latest stage of the disease and is normally not seen in rodents. Our multi-parameter method selects these features based on

the duration of diabetes as a significantly dominant marker for detection of diabetic retinopathy. The duration of diabetes has a significant impact on the parameters indicated above. Thus, for animals with longest duration of diabetes all these changes are significant marker of diabetic retinopathy. Therefore, with longer duration of diabetes in 11 month-old groups all the features can be used to quantify the retinal changes and train the classifier. Figure 3-4 demonstrates that 11 month-old diabetic retinas have a lower cell density and vessel coverage but a greater EC/PC ratio, higher number of acellular capillaries, and larger fractal dimension.

The fractal dimension, which is a useful measure of the complexity present in the retinal vasculature, determines the self-similarity of the vessel structure. As retinopathy progresses, new and smaller blood vessels begin to grow out of the existing larger vessels, with similar characteristics to the larger vessels, showing that the vessel structure is in fact fractal. Our measured fractal dimension is close to the reported fractal dimension of a diffusion limited aggregation process (~1.7) [231-234]. In addition, there is a correlation between retinal complexity and fractal dimension. This correlation occurs because of the properties of fractal dimensions, which increases as the new vessels grow in with the same properties as the existing larger vessels. Our studies showed that greater retinal fractal dimension represents increased geometric complexity of the retinal vasculature associated with diabetic retinopathy. Since significant increases in acellular capillary formation and fractal dimension are usually observed after 6 months of diabetes [222, 228, 235], these parameters are not appropriate to quantify injury in the 6 month-old diabetic groups. Thus, only cell count, vessel coverage, and EC/PC ratios were used for classification (Figure 3-5b).

In addition to diabetic retinopathy, another type of retinopathy induced by Bcl-2 deficiency was studied. Vascular cell count and retinal vascular density were selected as the markers for the *early* diagnosis of this type of retinopathy [70]. The cell count is an important indicator of retinopathy, as it is directly related to the *early* loss and *later* growth of new blood vessels. Thus, we expect the concentration of vascular cells in the retina and also vascular density to be two precursors of retinopathic injury at the early stages. At 6 weeks of age, Bcl2-/- and healthy retinas were classified (Figure 3-5a) with 85% accuracy showing that these two features are significantly effective, and our multi-parameter method is sensitive to quantify the *early* structural changes of retina with Bcl-2 deficiency.

In conclusion, we have studied morphological details of retina including cell count, vessel coverage, and the EC/PC ratios which were associated with loss of the pericytes as the earliest sign of diabetic retinopathy [229]. Other quantifiable morphological features such as acellular capillaries and fractal dimension correlated with progression of diabetic retinopathy [232], were also investigated. The current multi-feature method has the capability to detect and quantify the structural changes in the vasculature of retina at the *early stages* of the disease, and provides an opportunity to get a comprehensive view of retinal vasculature at the cellular level. Therefore, with new advancements in new imaging modalities with cellular resolution it will be possible to utilize the method developed here for quantitative evaluation of retinal vasculature with significant accuracy. This knowledge will be instrumental in development of new treatment modality to stop the development and progression of the disease and save vision. With the addition of more features, we hope to create a system capable of detecting and classifying even small changes in the retinal vasculature, allowing for the earliest detection of the injury. Our system can also be used to assess

the impact of various gene mutations, deletions, and over expression on retinal vascular development and function in a high-throughput and reproducible manner.

3.2 Time lapse microscopy of live lung cells *in vitro*

This section is dedicated to live cell studies, using fluorescence microscopy to assess reactive oxygen species (ROS) in PAECs due to the metabolic modulation, injury, and oxygen tension.

ROS are biologically important molecules. They are involved in signaling, but when present in excess (oxidative stress), they exert deleterious effects on cell structure and function. There is an increasing evidence that reactive oxygen species (ROS) participate in diverse lung injuries [106-111] including persistent pulmonary hypertension of newborn (PPHN) [112, 113] and hypoxia, which are the subjects of current study. Understanding and discerning the role of ROS depends on the ability to measure and quantify the dynamics of mitochondrial ROS production in normal and stress conditions. A variety of metabolic modulators of mitochondria, such as ETC uncoupler and inhibitor, as well as oxygen stress conditions (hypoxia, and ischemia reperfusion) lead to altered mitochondrial ROS production [111-113, 236].

ROS are produced in mitochondria and from non-mitochondrial sources, including the NADPH oxidase system and uncoupled endothelial nitric oxide synthase. Mitochondrial ROS are generated primarily during electron transfer along the electron transport chain (ETC) complex proteins. Of all the cellular sources of ROS, electron leakage from the ETC to O2 (dioxygen) is responsible for a steady flux of superoxide $O_2^{\bullet-}$ anions, which makes mitochondria the major site of the primordial ROS production [204, 237-239]. Under physiological conditions, small amounts of ROS are generated due to partial reduction of O2 into $O_2^{\bullet-}$ anion [16, 17, 239, 240]. The major areas for electron leak leading to $O_2^{\bullet-}$ production includes flavins and quinones of the ETC complexes, and this is more prominent under conditions that decrease electron transfer to complex VI, the terminal electron acceptor [239]. Since $O_2^{\bullet-}$ is the precursor of most of the downstream

ROS and it is also involved in the propagation of oxidative stress-mediated damages, it has become an important biomarker to assess oxidative damage of key macromolecules [240, 241].

A fluorescence probe, and a derivative of Hydroethidine (HE), MitoSOX Red is widely used for mitochondrial-targeted $O_2^{\bullet-}$ detection in live cells [14]. The positive charge on the phosphonium group in MitoSOX Red selectively targets this cell-permeant HE derivative to mitochondria [242]. Once in mitochondria, MitoSOX is oxidized by $O_2^{\bullet-}$ and the oxidation product elicits fluorescence response [242, 243] proportional to $O_2^{\bullet-}$ concentration. In numerous studies, MitoSOX use was validated with fluorescent microscopy [243-252] for selective detection of mitochondrial $O_2^{\bullet-}$ in endothelial cells [246, 247, 253], cardiomyocytes [246, 251, 253, 254], fibroblasts [252], and neuronal cells [243, 245, 248-250]. However, none of these studies allow for real-time detection of the mitochondrial superoxide production. Therefore, we aimed to develop a simple and quantitative method for detection of the mitochondrial superoxide production simultaneously in a large population of live cells with MitoSOX.

Since $O_2^{\bullet-}$ is the primordial ROS, we devoted our effort in this study to monitor and quantify the dynamic changes in $O_2^{\bullet-}$ production during modulation of ETC activities in PAEC, which to date has not been reported. We show for the first time that time-lapse microscopy in combination with MitoSOX can be used to quantitatively measure in real-time mitochondrial $O_2^{\bullet-}$ production. Our method was validated in PAECs using modulators of ETC, inhibitors: rotenone (complex I), antimycin A (complex III) and KCN (complex IV), and an ETC uncoupler, PCP. In addition, to further ascertain that ROS are primarily of mitochondrial source, the SOD mimetics, Mito-tempol, and tempol were used during the perturbation of mitochondrial ETC function. Addition of the metabolic agents induced metabolic stress that led to dynamic changes in the rate of $O_2^{\bullet-}$ production over time. It is worth noting that in other cell types, especially non-excitable

cells like PAECs, other sources of ROS production, for example NADPH oxidases (NOx) could contribute to the total $O_2^{\bullet-}$ production during simulated metabolic stress. Therefore, additional experiments were conducted using apocynin to assess potential ROS production from NOx sources. Overall, the use of time-lapse microscopy provides an ideal approach to study the spatial and temporal changes in mitochondrial $O_2^{\bullet-}$ production in real time during metabolic stress in live cells. Our method not only assesses the $O_2^{\bullet-}$ production from the ETC, but also localizes the source of ROS in mitochondria and extra-mitochondrial sources.

To demonstrate the capability of the presented method and the stablished experimental protocol, the dynamics of the superoxide production was also monitored, quantified, and compared in PAECs from injured hypertensive and normotensive animals. The protocol was also utilized to study the dynamics of the superoxide production in PAECs under oxygen stress conditions.

Lastly, the application of this approach is not limited to studying dynamic ROS production in real time in PAECs, it can be used in other live cell types under normal and pathophysiological conditions.

The following subsections will go through the experimental preparations, procedure, image processing as well as show and elaborate on the results.

3.2.1 Live cell preparation

PAECs from normotensive fetal lambs (NFL) and hypertensive fetal lambs (HTFL) as an injury model of PPHN were isolated and characterized using techniques described previously [119, 255]. Isolated PAECs were cultured in DMEM (Life Technologies) with 20% FBS (Life Technologies) and 1 X antibiotic/antimycotic (Life Technologies) at 37°C in room air and 5% CO2. PAECs between passages 3 and 4 were used for our experiments, and were cultured (104 cells/well) in 4-well chamber slides (Lab-Tek, VCAT) and kept in the incubator (room air and 5%

CO2, 37oC) before imaging. At the onset of each experiment and fluorescent imaging, the cells were loaded with 0.5 μM Hoechst (Life Technologies H1399, excitation/emission: UV/blue) in 2 ml growth medium to stain the nuclei and then incubated for 30 minutes before imaging. Following incubation, the cells were washed twice, and Hank's Balanced Salt Solution (HBSS, Life Technologies 14025092) was added to the plate for subsequent fluorescent imaging. During the imaging, production of mitochondrial $O_2^{\bullet-}$ was visualized in intact cultured PAECs loaded with a mitochondrial-targeted dihydroethidium (Mito-HE), red fluorescence probe (MitoSOX, Invitrogen M36008; excitation/emission: 510/580 nm; 0.5 μM). Once in the mitochondria, MitoSOX is oxidized by $O_2^{\bullet-}$ and exhibits a red fluorescent response proportional to the $O_2^{\bullet-}$ level.

3.2.2 Time-lapse microscopy

Live cell images were acquired at a magnification of 20× with a scale of 0.32μm per pixel, using the fluorescence microscope described in section 3.2.3. Time-lapse images were captured in the blue (Hoechst), red (MitoSOX), and bright field (BF) channels to monitor nuclei, mitochondrial ROS levels and the structure of the cells (Figure 3-6). Four FOVs of cells were imaged (one FOV in each chamber of the bottom-glass dish) under the aforementioned settings. The microscope is surrounded by a custom-made chamber (Okolab) housed around the stage, providing gas exchange and controlled temperature for time-lapse imaging over several hours. During the experiments, the level of the CO2 inside the chamber was maintained at 5% by mixing CO2 with room air at the proper ratio and chamber temperature was kept at 37 ± 2 °C. O2 and CO2 levels were continuously monitored with an O2-BTA model O2 sensor and CO2-BTA model CO2 probe (Vernier Co., Beaverton, OR).

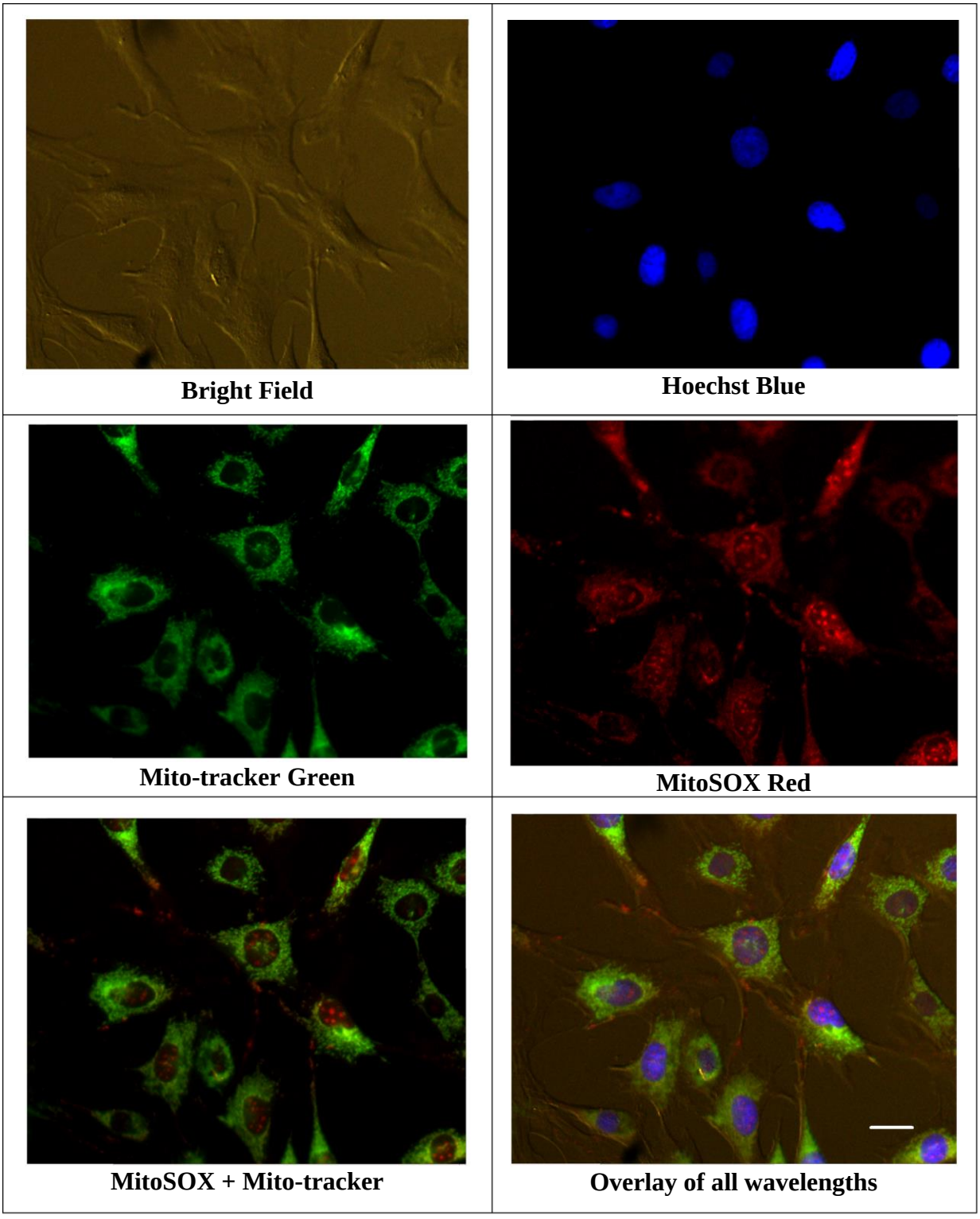

Figure 3-6: Panel A: from left to right are cell images in bright-field, and blue (Hoechst) fluorescence. Panel B shows Mito-tracker green and Mito-SOX red fluorescence signals, respectively. Panel C shows the overlay of the different fluorescence signals, left: merge of the red and green fluorescent markers demonstrates mitochondrial co-localization; right: all four fluorescent signals merged. Note that the scale bar in the right-bottom frame represents 32 µm (~100 pixels).

- **MitoSOX loading**

Production of O2•- in the live cells is visualized by MitoSOX Red chemical dye. This fluorescent probe is a triphenylphosphonium (TPP+)-linked DHE compound. It is preferentially attracted to the mitochondria by >100-fold compared with the cytosol [256] due to the strong negative mitochondrial membrane potential (ΔΨm). In mitochondria, the accumulated MitoSOX is oxidized by $O_2^{\bullet-}$ and the oxidation product exhibits fluorescence upon binding to mitochondrial DNA [242, 243]. The high matrix concentration of MitoSOX also allows the dye to compete with the endogenous mitochondrial $O_2^{\bullet-}$ scavenger, MnSOD, for $O_2^{\bullet-}$ [257, 258].

For the time lapse monitoring of the $O_2^{\bullet-}$ production, MitoSOX loading was performed online while the experiment was running in the microscope chamber environment. To maintain the high intra-mitochondrial concentrations of MitoSOX, the loading process was not followed by a wash. This approach keeps the MitoSOX concentration in mitochondria to compete with MnSOD for $O_2^{\bullet-}$. Ongoing binding to mitochondrial $O_2^{\bullet-}$ allows for the real-time monitoring of the MitoSOX oxidation rate translated to the $O_2^{\bullet-}$ concentration and production rate over time.

- **Co-localization**

Z-stacks of green and red fluorescence images of 20 randomly selected PAECs previously stained by Mito-tracker green and loaded online by MitoSOX red were acquired. The nuclear region of each cell image in z-stacks was excluded using the nuclear mask obtained in blue channel. Co-localization analysis was performed by pseudo-coloring and merging green and red fluorescence images together. Observations showed that both fluorophores reside within the same 3D volume whose minimum size is defined by the resolution limits of the microscope (0.32μm at a magnification of 20×). Quantitative statistical analyses of both the spatial distribution and the correlation between the intensities of the green and red fluorescence images were performed to

measure co-localization. Co-localization was determined by quantification of overlapping channels, performed by using the "object based methods" algorithm of JACoP plugin V2.0 [259].

3.2.3 Experimental procedure

Our experimental protocol was designed to measure changes in mitochondrial $O_2^{\bullet-}$ production associated with metabolic stress conditions as a model of ROS mediated dysfunction. Time-lapse images of FOV were captured in blue, red, and bright field channels, all in 1-minute intervals for 80 minutes. Ten minutes of baseline imaging was followed by the addition of MitoSOX 0.5μM to the PAEC live cells. Imaging was continued for 20 minutes after the addition of MitoSOX. Then cells were treated with pentachlorophenol sodium salt (PCP, ETC uncoupler, Sigma Alrich #76480), rotenone (Complex I inhibitor, Sigma Alrich #R8875), antimycin A (Complex III inhibitor, Sigma Alrich #A8674), or potassium *cyanide* (KCN, complex IV inhibitor, Sigma Alrich #60178) to study the $O_2^{\bullet-}$ production in the mitochondria as indicated by fluorescence intensity. Image acquisition continued for 50 min after adding the inhibitors/modulators. These agents also provide means to validate mitochondrial $O_2^{\bullet-}$ production in PAECs during online assessment of MitoSOX oxidation based on our experimental protocol.

To demonstrate the capability of our method to localize the source of mitochondrial $O_2^{\bullet-}$ under the stress condition, a dual agent (metabolic modulator) experimental protocol was designed. Five minutes after initiation of uncoupling induced by addition of the PCP, a metabolic inhibitor (rotenone, antimycin A or KCN) was administered. This approach identifies the specific ETC complexes associated with the large increase in $O_2^{\bullet-}$ using specific blockers, rotenone (complex I), antimycin A (complex III), or KCN (complex IV). Fluorescent recording was for 50 min after adding the second agent. These experiments were designed to determine the primary source of mitochondrial $O_2^{\bullet-}$ during uncoupling (PCP) of mitochondrial respiration.

Dual-agent experimental protocol is also helpful to validate mitochondrial $O_2^{\bullet-}$ production with real-time monitoring of MitoSOX oxidation using positive controls (uncoupler or inhibitor) as first agent and negative control (Mito-tempol) as second agent.

For the study of the cellular ROS dynamics in oxygen stress conditions, the experimental protocol was slightly adjusted. For the hypoxic condition, cells were incubated in hypoxic condition (3% oxygen, balanced nitrogen) for 2 hours and then continuously were exposed to hypoxic condition for imaging. For the stress condition resembling ischemia reperfusion, cells were incubated in hypoxic condition for 2 hours but then imaged in normal oxygen condition. Mito-SOX loading and drug treatment were performed based on the original experimental protocol described earlier. The changes in the superoxide production rate was quantified then in hypoxic cells before and after drug treatment.

3.2.4 Image and signal processing

The following subsections explain in detail the image and signal processing algorithms that were developed for time-lapse images.

- **Cell segmentation**

The segmentation algorithm described in section 3.2.4 was used to detect the border of the cells in the bright field images. The obtained mask (cells contours) was applied to the time-lapse image stack in the red fluorescent channel. The nuclei were also identified in the blue images and the resulted binary image was used as a mask for the stack of the red images to exclude the nuclei contribution from red intensity profiles. The mean intensity of the mitochondria in red channel images was calculated as a raw intensity profile of the live PAECs over time. This profile helps to monitor the dynamics of the mitochondrial ROS production before and after altering ETC function.

- **Intensity profile extraction**

Figure 3-7 represents the overall methodology to obtain final intensity profile of the cells from the input fluorescent images. Intensity profile of the red fluorescence images shows the dynamic of

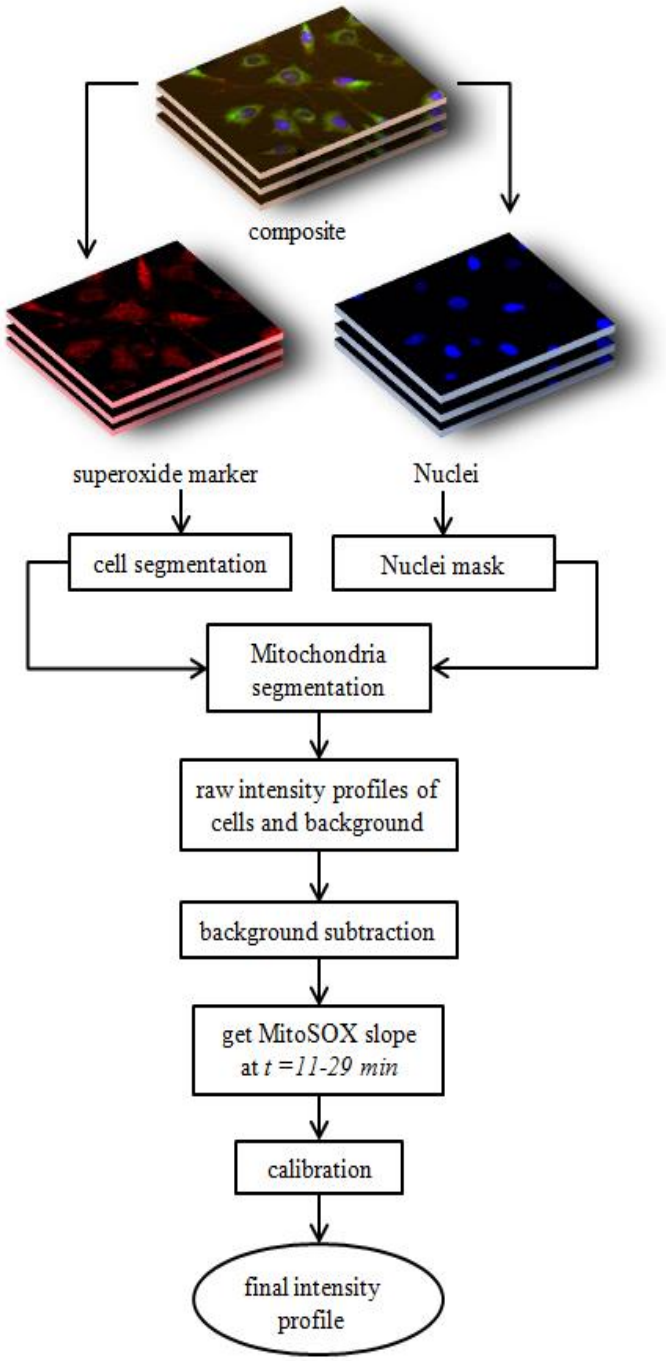

Figure 3-7: A schematic illustration of the methodology used to obtain the MitoSOX fluorescent intensity profiles of the cells from the input fluorescent images. The schematic flow chart shows the same approach for a typical single or dual-agent experiment.

$O_2^{\bullet-}$ production in response to MitoSOX (added at t=10 min) and metabolic agents (added at t=30 min). In order to quantify the dynamic changes in mitochondrial $O_2^{\bullet-}$ levels, and compare the changes in $O_2^{\bullet-}$ production between the control group (PAECs with MitoSOX i.e. no treatment) and treated groups (PAECs treated by inhibitor or/and uncoupler), the raw intensity profiles were first background subtracted, and secondly slope calibrated. Day-to-day variation of light intensity and illumination pattern, led to variations in the basal level intensity, which was accounted for as background subtraction. A linear scaling, slope calibration method, which preserves the slope ratio, was employed for better demonstration and comparison. The slope calibration was done in the single agent experiments, using the linear property of the MitoSOX-induced intensity rate (for 20-minute interval after administration of MitoSOX and before addition of the metabolic agent). The slope of the linear fit of the intensity profiles was calculated in the MitoSOX interval (t=11-29 min) for both control and treated groups. The MitoSOX-interval slope of the cell intensity profile in both control (no treatment) and treated groups were calibrated based on the MitoSOX-interval slope of a control in such a way that their slopes at this interval and before adding the agent were the same. Then the difference in the slope of the control and treated groups profiles was distinguishable after adding the agent. Therefore, the resulted intensity profiles are visually comparable for control and treated groups in the time interval of t=30-80 min which is helpful to evaluate the effect of the metabolic agent on the intensity profile. As mentioned earlier, for the dual agent experiments, the second agent, rotenone, antimycin A or KCN was administrated five minutes after addition of the PCP. Since the objective of the dual agent experiments is the evaluation of the inhibitor effect in the presence of the PCP, the slope calibration was applied based on the PCP-interval slope (t=33-35 min) in such a way that their slopes at this interval and therefore before adding the second agent was the same. The resulted intensity profiles then are

compared to the PCP group and the dual agent groups in the time interval of t=35-80 min to evaluate the effects of the ETC inhibitors (rotenone, antimycin A and KCN) in the rate of the intensity after oxidizing the ETC with PCP.

3.2.5 Quantification of superoxide dynamics

- **Parametric nonlinear modeling**

Exponential and sigmoidal models were employed for describing the time course of the red fluorescence intensity of the treated and control cells. These models provide a way to evaluate the temporal responses of the cells to metabolic perturbation.

The exponential and sigmoidal models were solved for six coefficients including amplitudes *b* and *c*, the time constants *T* and τ (equations 3-6 and 3-7), the constant intensity offset *a*, and the displacement factor *d* (along the time axis) to fit the slope calibrated profiles of the intracellular intensity over time for each group of experiments including *n*=6 for both treated (I_1), and untreated (I_2) groups:

$$I_1(t) \sim a + b * e^{-\frac{t-30}{T}} \quad (3\text{-}6)$$

$$I_2(t) \sim \frac{c}{1 + d * e^{-\frac{t-30}{\tau}}} \quad (3\text{-}7)$$

For the exponential model, *T* is the time point when the intensity level reaches to 65% of the ultimate value, *a*.

The aforementioned nonlinear fits describe the surge and stationary phases of the rates of $O_2^{\bullet-}$ production of the PAECs in the presence and absence of metabolic agents/modulators. The exponential model also provides the parameter of $\frac{-b}{T}$, which quantifies the slope of the exponential fit right after the addition of the metabolic agent and compared the effects of the mitochondrial oxidizing agent (PCP) vs. the mitochondrial reducing agents (e.g. rotenone or KCN). Similarly,

$\frac{cd}{\tau(1+d)^2}$ quantifies the slope of the sigmoidal fit at the same time point to compare the rates of $O_2^{\bullet-}$ production in the absence and presence of the metabolic agents.

- **Slope ratio (linear approach)**

After calibration for the dual agent experiments, the ratio (SR) of the second agent-interval (*t*=35-37 min) and first agent-interval (t=33-35 min) slopes, which were obtained by linear fit in the corresponding intervals shows the changes in the rate of the intensity and $O_2^{\bullet-}$ production after the administration of the second metabolic agent.

$$SR = \frac{second\ agent\ slope(35-37\text{min})}{first\ agent\ slope(33-35\text{min})} \qquad (3\text{-}8)$$

Linear approach provides the possibility to quantify the effect of the reducing agents (ETC blockers) in the presence of the oxidizing agent (PCP).

3.2.6 Statistical analysis

Data are shown as means ± SE. Student's t-test was used for normally distributed data (*n*=6 for each group). A *p* value < 0.05 was considered significant.

3.2.7 Results

Figure 3-6 shows the localization of MitoSOX in mitochondria proving that we have studied the *mitochondrial* superoxide production. Microscopic images captured in bright field and fluorescent channels (Figure 3-6: panels A and B) show the cell structure/shape, nuclei and mitochondria stained with Mito-tracker (50 nM), and mitochondrial $O_2^{\bullet-}$ production detected by MitoSOX (0.5 μM). Panel C shows the overlay of the red and green fluorescent markers demonstrating mitochondrial co-localization. Co-localization of MitoTracker Green with the mitochondria-probe MitoSOX Red in PAECs confirmed that $O_2^{\bullet-}$ anions were produced from

mitochondria in cells exposed to metabolic stress conditions. The degree of co-localization of these two staining in the PAECs was 0.91± 0.06 indicating significant co-localizations.

This section will now go through the results of the ROS studies in PAECs isolated from normotensive lamb (NFL) and hypertensive lamb (HTFL) performed under metabolic stress, and oxygen tension conditions.

- **ROS production in NFL PAECs under metabolic stress**

Representative profiles in figure 3-8 show that the addition of MitoSOX increases the intensity of cell images gradually in the fluorescent red channel (*t*=10-29 min), but the rate of this increase occurred significantly later with the administration of uncoupling or/and inhibiting agents. The top panel in figure 3-8A displays red fluorescent images of PAECs from which intensities were translated to the rate of $O_2^{\bullet-}$ production in mitochondria. The first row is the control (CTRL) group, the second and third rows are cells with the addition of uncoupler (PCP, 15μM), and inhibitor (KCN, 20μM), respectively. The first column of images is the first frame of the time-lapse imaging (*t*=0 min) showing the FOV of interest with no contrast between cells and background. The second column of images shows the same FOV just before adding the uncoupler or inhibitor at time *t*=30 min. The addition of the agents enhances the contrast between cells and background due to increasing $O_2^{\bullet-}$ production in mitochondria, as evidenced by the increased MitoSOX (added at *t*=10min) fluorescent signal. Compared to the second column, the third column images show the frames (at time *t*=60 min) with slight increase of the intensity in the first row (CTRL group), and significant increase of the intensity in the second and third rows due to exponential increase of $O_2^{\bullet-}$ production after adding KCN and PCP, respectively. The last column of images shows the frames at time *t*=80 min demonstrating larger increase of ROS production rate in the control group (first row), and smaller increase of ROS production in the treated groups (second and third rows). These

observations are consistent with the intensity profiles demonstrated in panel B. Figure 3-8B shows the corresponding quantitative changes in the fluorescent intensity in the cell after calibration.

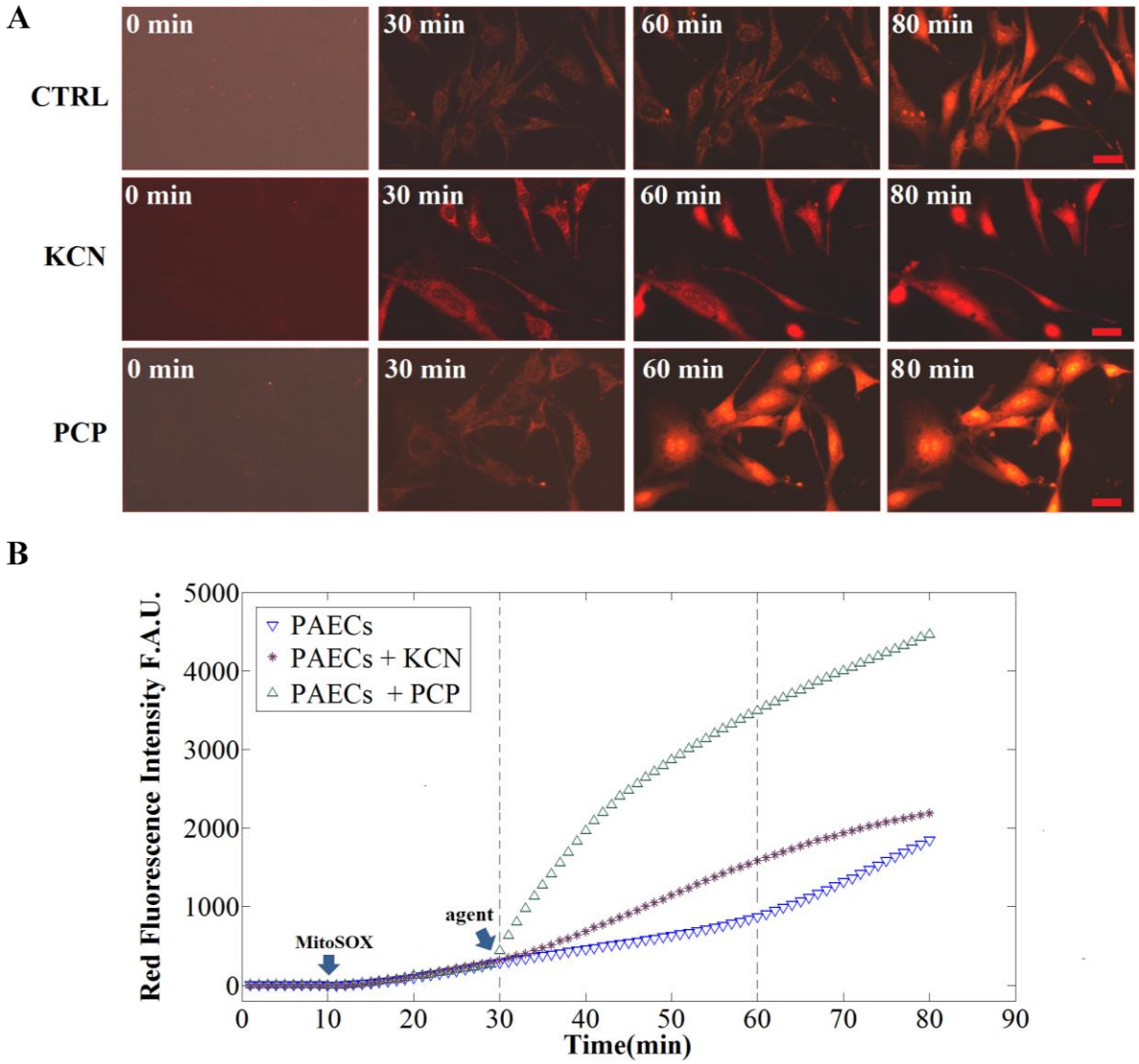

Figure 3-8: Panel A: representative raw frames from image stack of time-lapse microscopy showing dynamic $O_2^{\bullet-}$ production in 3 experiments using live PAEC loaded with MitoSOX in control (no treatment), in the presence of complex IV inhibitor (KCN) or the uncoupler PCP. Elapsed time is indicated in the upper left corner of each frame (0, 30, 60 and 80 min). Note that the scale bar in the right corner of the right bottom frame is the same for all frames and is 32 µm. Panel B: representative dynamic recordings of mean fluorescence intensity profiles of the cells in the three aforementioned conditions. The blue curve displays the dynamic of the fluorescence intensity in control cells over time; the green and purple curves represent the fluorescence intensity in cells treated with PCP and KCN, respectively. The arrows indicate the time MitoSOX and agents were added to the cells. F.A.U.,fluorescence arbitrary unit; KCN, potassium cyanide; PCP, pentachlorophenol sodium salt.

Inhibiting and uncoupling the mitochondria (purple and green curves, respectively) significantly increased the rate of $O_2^{\bullet-}$ production when compared to the control rate of $O_2^{\bullet-}$ production. Figure 3-8B also demonstrates that uncoupling the mitochondrial ETC with PCP resulted in an abrupt and marked increase in the rate of $O_2^{\bullet-}$ production when compared to the KCN treated cells. The slow but progressive increase of fluorescence over the 30-min to 80-min interval indicated that ROS production did not result from spontaneous auto-oxidation of MitoSOX molecules at stress conditions but involved cascade of enzymatic reduction-oxidation reactions and active cellular responses. Enhanced fluorescence intensity was evident right after addition of the metabolic agents, and its intensity increased continuously and exponentially over time, demonstrating a time-dependent amplification of ROS production.

To quantify the rate of $O_2^{\bullet-}$ production in the absence and presence of inhibitors or an uncoupler (added at t=30-80 min), sigmoidal and exponential models were fitted to the experimental data (control and treated cells). The BIC (Bayesian Information Criterion) of the fitted models assessed lower than -77 which confirms these models as good fits for the intensity profiles. Figure 3-9 shows the exponential (equation 3-6) and sigmoidal (equation 3-7) fit parameters as well as the initial slope of the intensity profile right after addition of the uncoupler/inhibitor. These nonlinear fits demonstrate that treating the cells with oxidizing agent (PCP 15µM), or reducing agents (ROT 15µM, AA 1µM, and KCN 20µM) results in significantly larger increase in the slope of the intensity profile ($\frac{-b}{T}$: 151.5±18.3, 56.6±1.8, 82.1±2.7, 56.5±4.8) at t=30 min when compared to that of the control cells ($\frac{cd}{\tau(1+d)^2}$: 36.6±3.7). Presented values correspond to the initial time (t=30min) when the metabolic agents were added. To evaluate for consistency and reproducibility of the results, a total of 48 wells of PAECs were imaged, with n=6 for each of the treated groups and the control. The slopes of the fitted models were calculated at

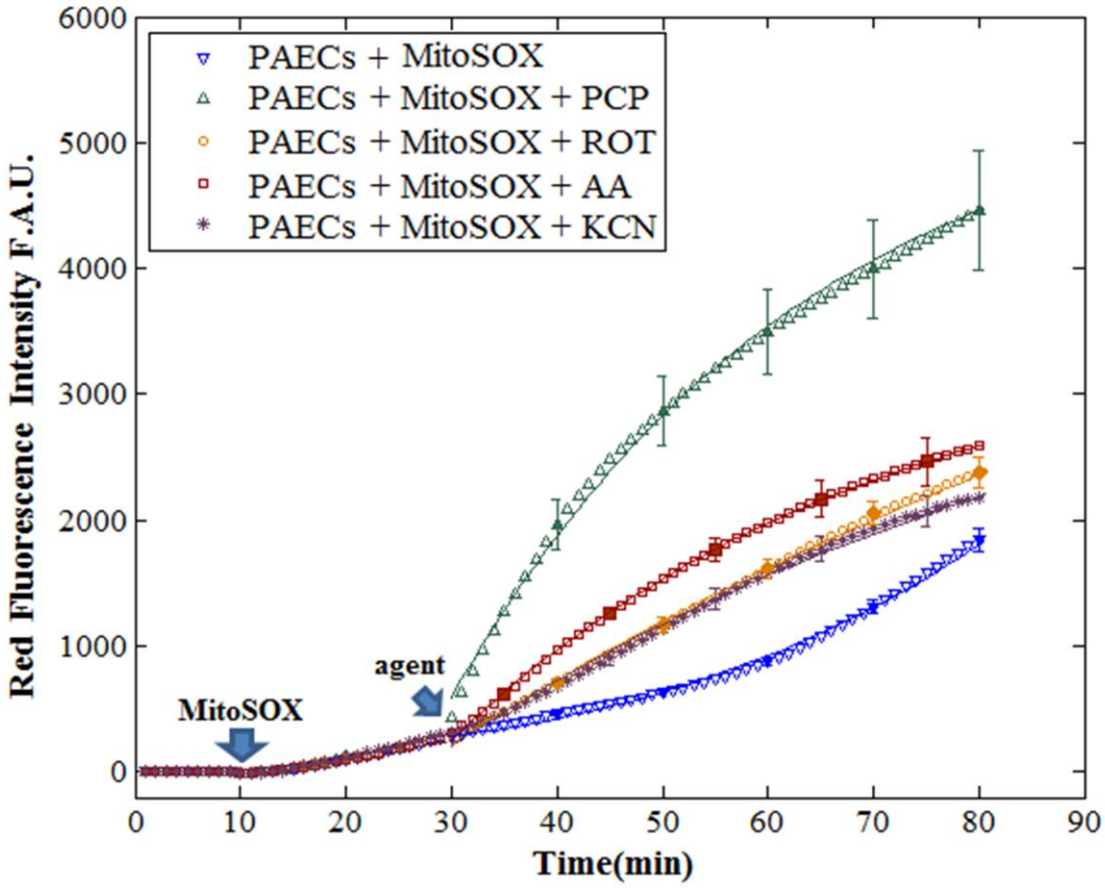

B

	fit parameters			initial slope
agent	**a**	**T**	**b**	$\frac{-b}{T}$
PCP	5943.7±960.7	36±6.9	-5360.3±993.5	151.5±18.3
ROT	8004.8±2860.9	143.2±58.2	-7791±2850.5	56.6±1.8
AA	3671.5±445.6	40.9±4.6	-3421.3±459.3	82.1±2.7
KCN	4429.4±607.1	77.6±11.6	-4224.1±620.1	56.5±4.8

	c	**τ**	**d**	$\frac{cd}{\tau(1+d)^2}$
CTRL	3216.7±247.4	12.7±0.3	5.2±0.3	36.6±3.7

Figure 3-9: A: Dynamic fluorescence intensity profiles over time of cells in the presence or absence of the uncoupler (PCP) or the mitochondrial ETC complex inhibitors (ROT, AA, or KCN). Values are means ± SE; n=6 for each treatment group. The solid lines are exponential and sigmoidal fits to the mean values of the agent -treated and control data. B: The table shows the mean values of fit parameters and the initial slope of the exponential and sigmoidal fits at t = 30 min for each treatment group and control. F.A.U., fluorescence arbitrary unit; ROT, rotenone; AA, antimycin A; KCN, potassium cyanide; PCP, pentachlorophenol sodium salt.

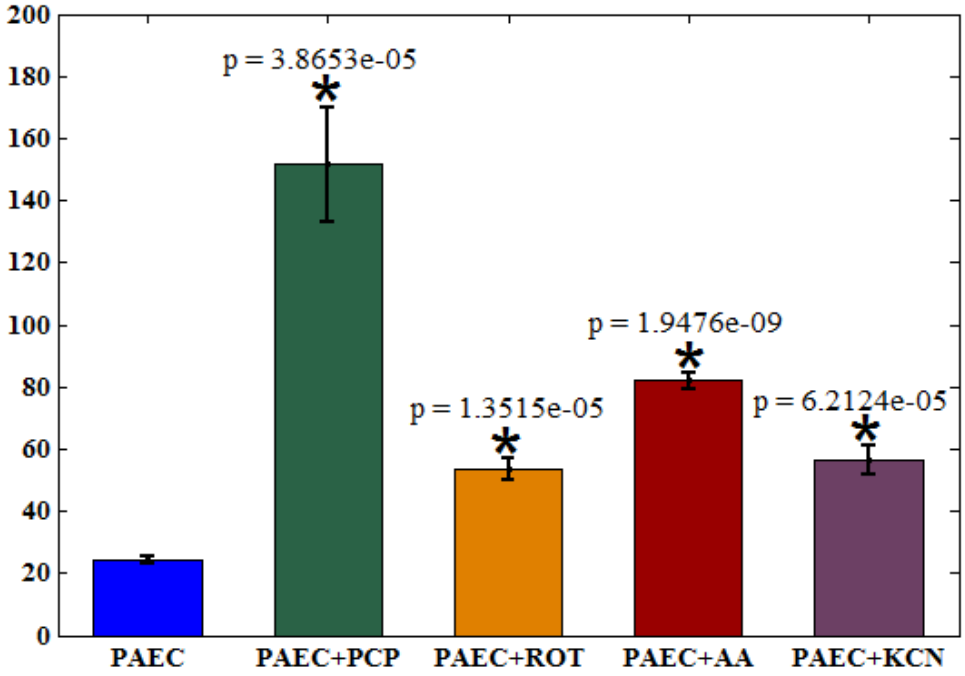

Figure 3-10: Summary bar graphs show the slope of the fluorescence intensity profiles right after the agent administration. Bar graphs show the means ± SE of the red fluorescence intensity slopes (t=30 min) for the five groups of cells. Addition of agents to PAECs (green, orange, red, and purple bars) resulted in *significant* (* $p<0.05$) increase in the rate of $O_2^{\bullet-}$ production when compared to the non-treated (control) PAECs (blue bar). n=6/group.

the time of the administration of the agent for six FOVs of each group of the treated cells and control cells. Green curve of figure 3-9 corresponds to the average profile of the PCP experiments. This curve demonstrates the fastest and greatest increase of 4.90 ± 0.5 in the rate of the $O_2^{\bullet-}$ production in the uncoupled mitochondria. The slopes of the intensity right after the addition of mitochondrial metabolic modulators (t=30min) were compared statistically in Figure 3-10, demonstrating significant changes between treated groups vs. control group.

To demonstrate the capability of our method to localize the source of mitochondrial $O_2^{\bullet-}$ under stress condition, a dual exposure experimental protocol was designed. This method was

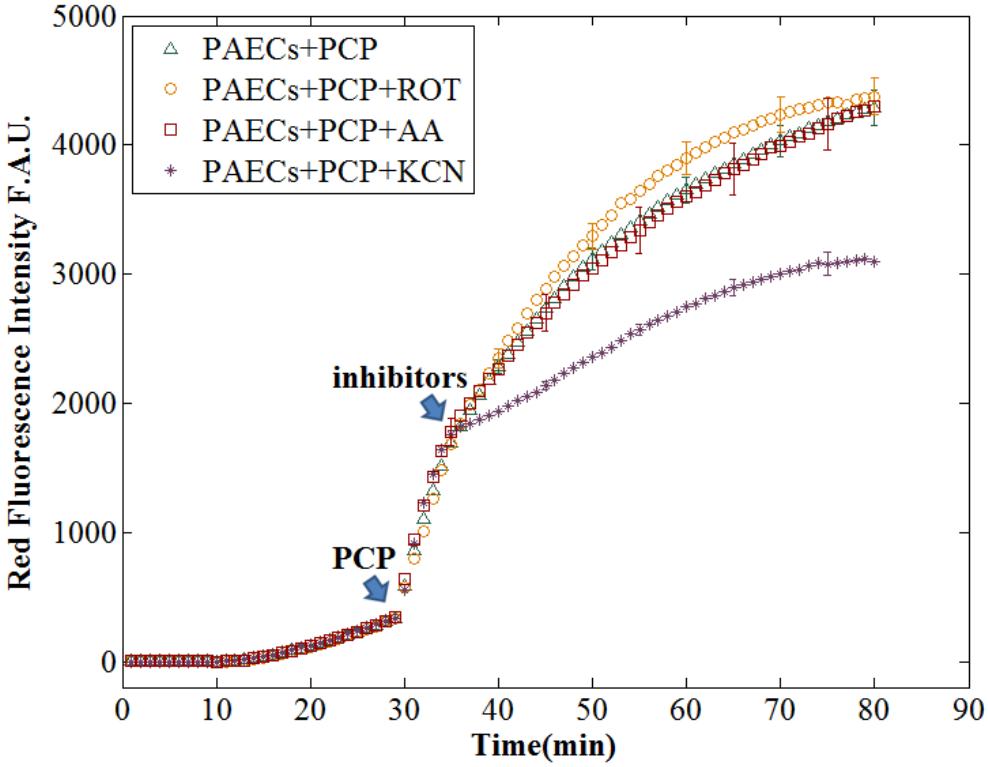

(a)

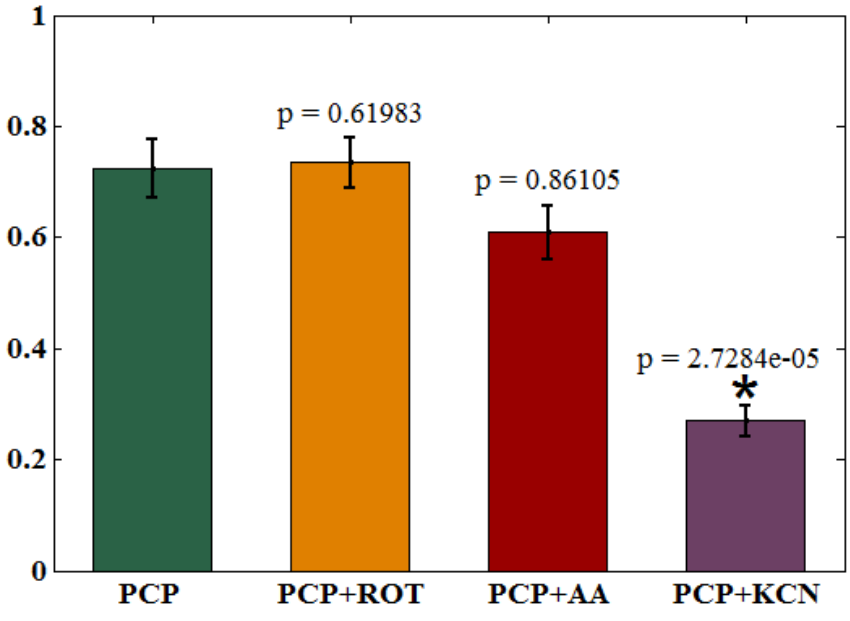

(b)

Figure 3-11: a) Mean ± SE of fluorescent intensity profiles of $O_2^{\bullet-}$ production over time in PAECs treated with PCP in addition with one of the ETC inhibitors; b) Summary bar graphs show mean ± SE of the slope ratio (SR, equation 3-8) of the red fluorescent intensities (t=35min) for the four treatment groups. n=6

able to partition the $O_2^{\bullet-}$ production from different parts of the ETC. After oxidizing the ETC with PCP, the ETC was reduced with the different ETC complex inhibitors to tease out the complexes responsible for the surge in $O_2^{\bullet-}$ production when PCP fully oxidizes mitochondrial ETC. The curves in figure 3-11 represent the profiles of mean intensity in each time point for the corresponding groups. The green curve displays PCP-induced intensity profile compared to the orange, red, and purple curves, which demonstrate the effects of the addition of ROT, AA, and KCN to the PCP treated cells. The slope ratio (SR) was calculated for all four groups, with n=6 for each group. Bar graphs in figure 3-11 show the means and SEM of the SR of the red fluorescence intensity for each of the four groups of cells. When compared to the addition of ROT and AA (orange and red bars, respectively), the addition of KCN to PCP-treated PAEC (purple bar) resulted in a significant reduction (p= 9.8026e-5), 62.7%, in the rate of increase of the fluorescence intensity as compared to fluorescence intensity of PAEC treated with PCP alone (green bar). This result shows that only KCN was able to partially reverse the effect of the uncoupling agent on the $O_2^{\bullet-}$ production.

We have also found further evidence that the surge in mitochondrial $O_2^{\bullet-}$ production by PCP is reversible by mitochondrial-targeted ROS scavenger, MitoTempol. The dual-agent exposure protocol is helpful in demonstrating this reversible effect while monitoring the real-time oxidation of MitoSOX, using uncoupler (positive control) as a first agent and Mito-tempol (negative control) as a second agent. Figure 3-12 shows fluorescence intensity profiles in untreated cells (control; blue curve) and PCP treated cells in the absence and presence of the mitochondrial targeted scavenger MitoTempol over time (green and red curves, respectively). As observed previously, adding PCP at t=30 min markedly increased $O_2^{\bullet-}$ production rate (compare green profile with blue curve); adding MitoTempol at t=35 min significantly decreased the rate of $O_2^{\bullet-}$

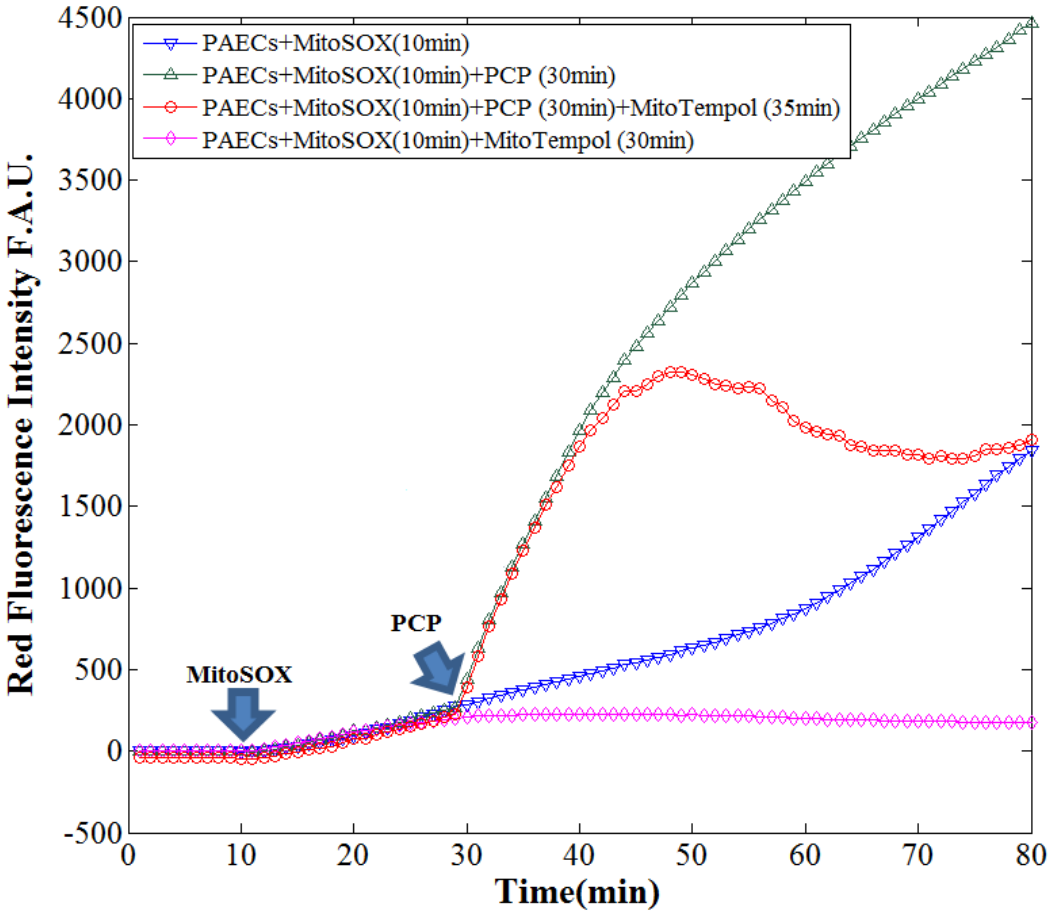

Figure 3-12: Representative fluorescent intensity profiles in untreated cells (control) and PCP treated cells in the absence and presence of the superoxide scavenger MitoTempol over time. The arrows indicate the time MitoSOX (10 minutes), PCP (30 minutes), and MitoTempol (35 minutes) were added to the cells. F.A.U.,fluorescence arbitrary unit; this panel shows that MitoTempol reversed PCP-induced $O_2^{\bullet-}$ production.

production (red profile vs. green curve), and by t=75 min, the PCP-induced $O_2^{\bullet-}$ production was completely abolished, reaching $O_2^{\bullet-}$ levels similar to the control cells (blue curve). The pink profile in this panel shows that using MitoTempol as a negative control decreased the $O_2^{\bullet-}$ production rate when compared with the control cells (blue profile). Comparison of the pink and blue profiles confirms that fluorescence measurement of MitoSOX oxidation reflects the dynamic changes in mitochondrial $O_2^{\bullet-}$ production in real-time. If MitoSOX is mitochondrial specific, then Tempol, a non-mitochondrial targeted ROS scavenger, affects the MitoSOX fluorescence less when

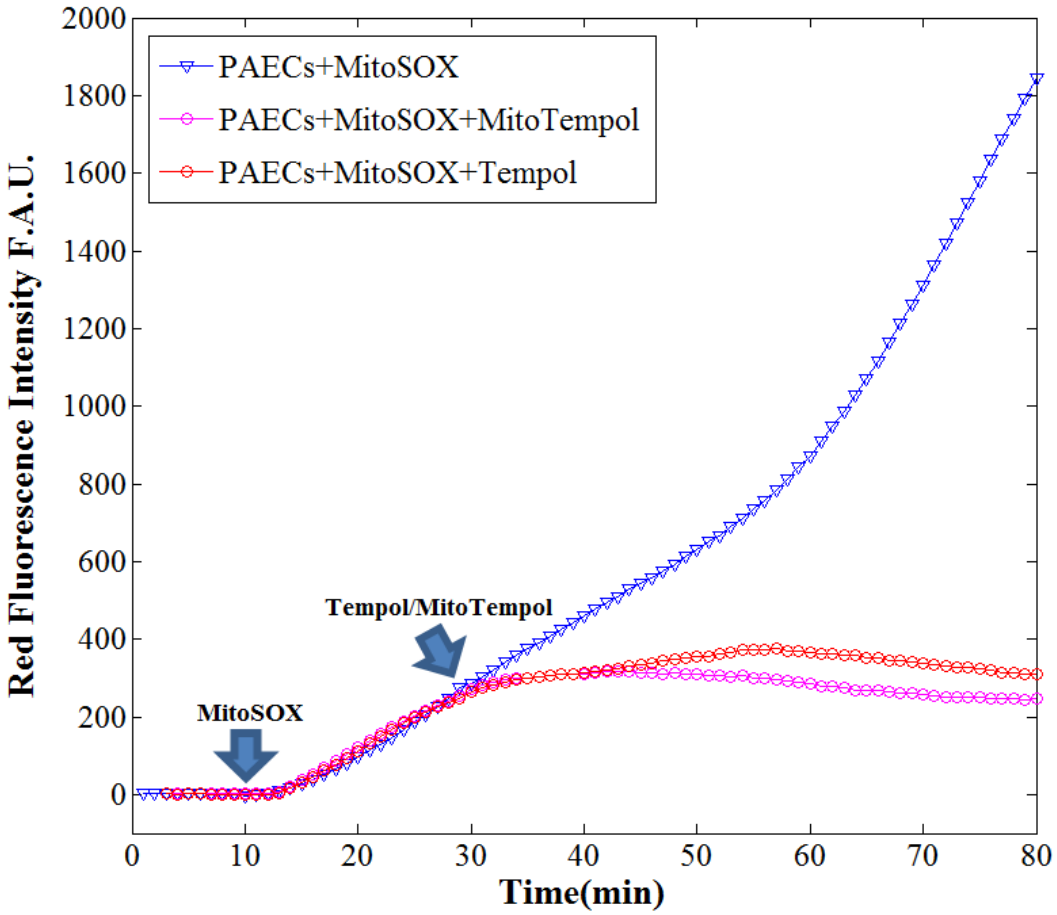

Figure 3-13: Representative dynamic fluorescence intensity profiles over time in the untreated cells (blue curve) and the treated cells treated with Tempol (red curve) and MitoTempol (pink curve). The arrows indicate the time MitoSOX (10 minutes), and MitoTempol (30 minutes) were added to the cells. F.A.U.,fluorescence arbitrary unit;

compared with MitoTempol. Figure 3-13 shows fluorescence intensity profiles of the untreated cells (blue curve) and the cells treated with Tempol (red curve) and MitoTempol (pink curve). These data demonstrate that the addition of MitoTempol reduced the $O_2^{\bullet-}$ levels, at a faster rate than Tempol. This result further confirms that MitoSOX fluorescence following oxidation by $O_2^{\bullet-}$ is correlated with mitochondrial $O_2^{\bullet-}$ production. We also observed that apocynin, NOx inhibitor, did not alter the trajectory of the mitochondrial ROS production (data not shown), verifying that the primary/major source of ROS during metabolic modulation in the PAECs is mitochondria.

- **ROS production in NFL versus HTFL PAECs under metabolic stress**

To investigates the hypothesis that pulmonary hypertension is associated with changes in mitochondrial superoxide production, NFL and HTFL PAECs were examined. The dynamic of the mitochondrial superoxide production in these two groups of PAECs was monitored over time using time-lapse microscopy and the experimental protocol described in section 3.3.3. After capturing the baseline images of the cells for 10 minutes, cells were stained with Mito-SOX reagent (0.5µM). To modulate the mitochondrial superoxide level, metabolic perturbation was induced by administration of 20µM potassium cyanide (KCN). The (red) fluorescence intensity profile of the cells was normalized to baseline and then background subtracted to monitor the dynamics of superoxide level over time and after inducing chain perturbation in mitochondria. Changes in the slope of the fluorescence intensity profile (t=30 min) in the red channel indicated the production rate of the superoxide before and after treating the cells with KCN (20µM). A total of 24 wells of PAECs were imaged including n=6 for each non-treated and KCN treated group.

Figure 3-14 shows the bar graphs illustrating the changes of superoxide production rate due to ETC inhibition by KCN for both NFL and HTFL PAECs. This figure illustrates that production of the superoxide in HTFL non-treated cells is 1.2 ± 0.2 faster than NFL non-treated cells and addition of KCN induced a significant increase of 1.9 ± 0.6 in the superoxide production rate of the HTFL PAECs as compared to the NFL FPAECs. Please note that the addition of KCN doubled (2 ± 0.8) and tripled (2.9 ± 0.7) the superoxide production rate in NFL cells (blue bars) and HTFL cells (red bars), respectively. Compared to NFL PAECs, addition of KCN induced instantly a significant increase of 1.9 ± 0.6 in the superoxide production rate of the HTFL PAECs.

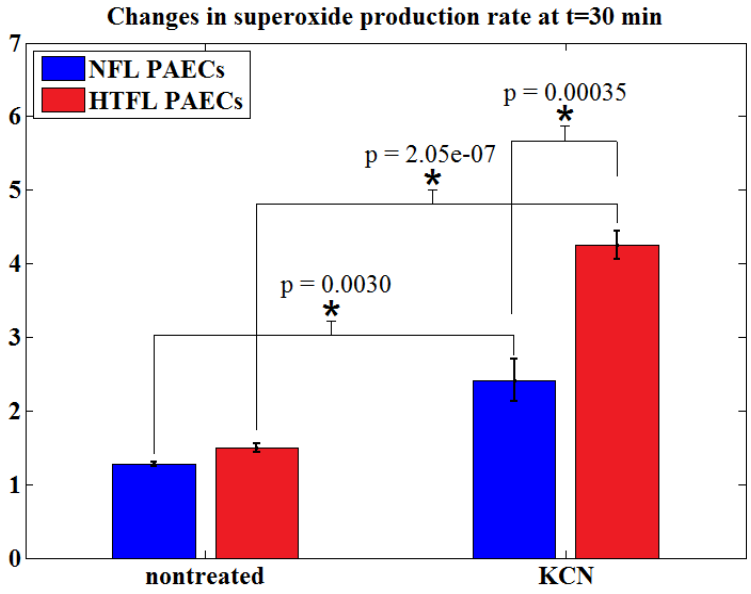

Figure 3-14: Bar graph plot showing the means and standard errors of the slope ratio of the red fluorescence intensity profile (*t*=30 min) for each group. Slope ratio is translated to change in the superoxide production rate. Blue bars correspond to NFL cells and red bars represent the HTFL cells. *n*=6/group.

- **ROS production in NFL PAECs under metabolic and oxygen stress**

The effect of the oxygen tension on the production of superoxide in mitochondria of PAECs were compared under two stress conditions including hypoxia plus uncoupling (by PCP) or ischemia reperfusion (IR; hypoxia followed by normoxia) plus uncoupling. The preliminary result is presented in figure 3-15. Hypoxic PAECs showed 2.7± 0.2 times higher superoxide production rate in uncoupled ETC than normal ETC. However, the production rate for the PCP-treated cells in the IR group increased by 4.4± 0.7 times compared to non-treated cells in this group. This result shows a wider dynamic range of the superoxide production in IR group versus hypoxia group.

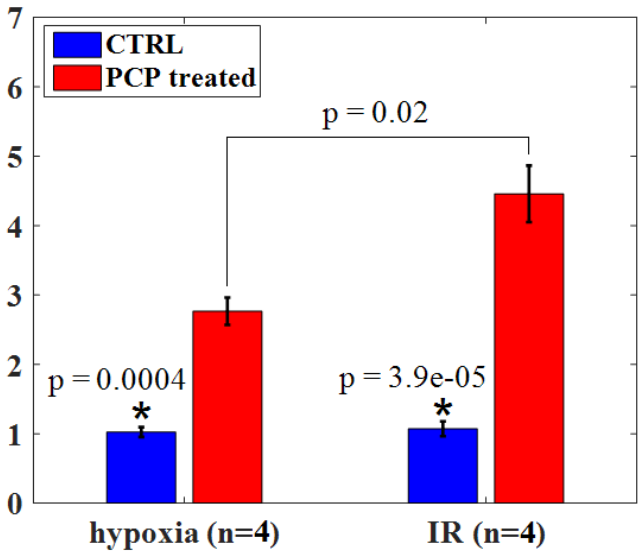

Figure 3-15: Bar graph plot showing the means and standard errors of the slope ratio of the red fluorescence intensity profile at *t*=30 min for hypoxia and IR groups. Slope ratio is translated to change in the superoxide production rate. Red bars represent the PCP-treated cells and blue bars correspond to non-treated cells. *n*=4/group.

3.2.8 Discussion and conclusion on lung cells *in vitro* studies

This study demonstrated the utility of fluorescent time-lapse microscopy for evaluating dynamic O2•- production along the ETC. Oxidative stress and mitochondrial dysfunction can lead to apoptotic cell death early in the pathology of different diseases [260-264] including pulmonary injury [107-110, 167, 265-270]. Therefore, the development of methods to assess the discrete sites for mitochondrial $O_2^{\bullet-}$ generation could help in recognizing the critical role of the organelle in the pathological generation of ROS in diseases and to understand the cellular responses to ROS mediated injuries.

I designed experiments to measure the changes in mitochondrial $O_2^{\bullet-}$ levels and rate of production over time with disrupted ETC function, to mimic pathological ROS emission (production>scavenging). MitoSOX Red was used as a $O_2^{\bullet-}$ indicator, which has been validated by others [243, 246, 247, 249, 251, 252, 271-274] for selective detection of mitochondrial $O_2^{\bullet-}$

production in endothelial cells [246, 247, 253]. Inline loading of cells with MitoSOX and real-time monitoring of mitochondrial $O_2^{\bullet-}$ production have not been previously reported.

The measurement of various ROS is dependent on suitable techniques and is impeded by lack of a sensitive and specific assay [239]. MitoSOX is a sensitive and specific fluorescent marker for mitochondrial $O_2^{\bullet-}$ and useful in the evaluation of dynamics of $O_2^{\bullet-}$ production. MitoSOX, a derivative of DHE, has the TPP-tag fluorescence that selectively targets and enters mitochondria in response to the strong ΔΨm [239]. Indeed, the strong negative ΔΨm makes the affinity and accumulation of the probe in mitochondria stronger than the cytosol [256]. This attribute makes the probe a suitable tool to assess mitochondrial-derived $O_2^{\bullet-}$ production in various live cells [242], including PAECs. The ETC drives electrons from reduced coenzymes (NADH(H+) and FADH2) to O2, which undergoes the complete reduction to H2O catalyzed by complex IV. During the electron transfer, some electrons escape from the ETC at discrete sites to generate $O_2^{\bullet-}$ [239]. $O_2^{\bullet-}$ production is favored in general by high ΔΨm and large NADH(H+), or when electron transfer is impeded by alteration in the ETC complexes [240, 275]. In this scenario, a decrease in ROS production would portend ΔΨm depolarization due to enhanced electron transfer, as observed with uncoupling agents. Paradoxically, though, conditions have been reported in which mitochondrial uncoupling and ΔΨm dissipation are associated with increased production of ROS [276]. This observation is consistent with our results which show PCP, an uncoupling agent, increases $O_2^{\bullet-}$ production (figures 3-5). According to the proposed model of redox-optimized ROS balance by Aon et al. [277], this apparent paradox might be explained by the hypothesis that physiological signaling ROS occurs within an optimized redox state, and oxidative stress can happen at the extreme of either reduction or oxidation. Consistent with this hypothesis, our results demonstrated higher $O_2^{\bullet-}$ levels and rates of production in both the reduced and oxidized ETC. The elevated level

of ROS initially overwhelms the scavenging potential of mitochondria and leads to excess ROS (oxidative stress).

Inhibitors of complex I are useful for determining the source of ROS [239]. The ETC is fully reduced when complex I is blocked with rotenone. Complex I, a transmembrane protein, oxidizes NADH and rotenone inhibits the electron transfer from Fe-S centers in the complex to coenzyme ubiquinone (CoQ), rendering complex I incapable of transferring electrons to CoQ [239]. The highly reduced redox state creates a buildup of electrons within the mitochondrial matrix, leading to forced electron leak that reduces O_2 to $O_2^{\bullet-}$ anions; thus making complex I a major site of $O_2^{\bullet-}$ production in the presence of rotenone [267, 269, 278]. This observation is consistent with our results that show (figure 3-9) an increase in the intensity of red fluorescence emitted from mitochondria after addition of rotenone. Increase in the slope of intensity profile by a factor of 1.83 ± 0.05 is translated to rotenone-induced increase in the rate of $O_2^{\bullet-}$ production from complex I. It is worth noting that complex I is probably the main source of mitochondrial ROS under most physiologic conditions.

Complex III is believed to contain a Q cycle with the inner Q (Qi) and outer Q (Qo) pool of ubiquinone (Q) oriented toward the matrix (i) and the mitochondrial inter-membrane space (o) [239]. Specifically, complex III funnels electrons from the CoQ pool to cytochrome c. It has been regarded as a source of ROS production in mitochondria, but whether the ROS produced is relevant physiologically or pathophysiologically [242, 243, 279, 280] remains controversial [239]. When supplied with $CoQH_2$ and when the Qi site is inhibited by antimycin, complex III produces large amounts of $O_2^{\bullet-}$ from the reaction of O_2 with an ubisemiquinone bound to the Qo site [242, 243, 279-284]. The red curve in Figure 4 shows the apparent increase by a factor of 2.66 ± 0.08 in the rate of $O_2^{\bullet-}$ generation initiated by addition of antimycin A. KCN is an irreversible inhibitor of the

enzyme cytochrome c oxidase, complex IV. The binding of cyanide to cytochrome c prevents transfer of electrons from the enzyme to O_2, creating a buildup of electrons within the inter-membrane space. As a result, inhibiting complex IV increases ROS production and decreases O_2 consumption and cellular respiration (hypoxia). The purple curve of Figure 4 corresponds with the average profile of KCN experiments. This profile shows a 1.83 ± 0.14 increase in the rate of $O_2^{\bullet-}$ production by KCN compared to the control (untreated cells). These data show that inhibition of O_2 binding with complex-IV leads to both electron backup and availability of molecular O_2 to be reduced to $O_2^{\bullet-}$, without the generation of H_2O.

Pentachlorophenol (PCP) is a powerful uncoupler of oxidative phosphorylation and also induces oxidative stress to cause mitochondrial damage [285-289]. PCP dissipates the proton gradient by consuming the proton motive force via increased proton leak back into the matrix. A recent study reported that PCP oxidizes the ETC and increase the activity of complexes I and II [290], leading to the production of more protons and transfer of more electrons along the ETC. Lack of proton gradient for phosphorylation activates a mechanism to compensate for the uncoupling effect by increasing proton pumping in an attempt to reestablish the proton gradient. Paradoxically, the increase in activity of the complexes in the uncoupled chain increases electron transfer along the ETC, and as a result, increases electron leak to O2 leading to $O_2^{\bullet-}$ production [277, 291-294]. This notion is supported by our observation that uncoupling respiration with PCP led to the fastest and greatest increase (figure 3-9) in the mitochondrial $O_2^{\bullet-}$ production. The finding also suggests that the increase protonophoric effect of FCCP (electron leak) leads to a feed-forward mechanism that exacerbates ROS production.

Administration of the ***metabolic stressor***/modulators (PCP, KCN, AA, or ROT) in PAECs induces two phases of the $O_2^{\bullet-}$ production (figures 3-8 and 3-9). Initial $O_2^{\bullet-}$ formation increases markedly right after addition of the metabolic agents (surge phase) but later settles to a state in which the $O_2^{\bullet-}$ production rate (the slope of the intensity profile) decreases and eventually saturates (steady-state phase). This steady-state phase is consistent with the view that increased $O_2^{\bullet-}$ level induces MnSOD activity as a negative feedback mechanism to remove the excess $O_2^{\bullet-}$ and therefore decrease the rate of $O_2^{\bullet-}$ levels over time [295] as compared to the early phase of the stress condition. The fast dismutation of $O_2^{\bullet-}$ by MnSOD also enhances this saturating effect. The oxidation of MitoSOX is 500 times slower than the rate of $O_2^{\bullet-}$ scavenging by SOD [243]. Therefore, less $O_2^{\bullet-}$ is available for oxidizing MitoSOX leading to a decrease in the rate of the $O_2^{\bullet-}$ at the later stage of the imposed stress conditions.

Figure 3-9 also represents the ***nonlinear fitted models*** to the intensity profiles of the treated and non- treated PAECs. These nonlinear fits show that chain uncoupling and inhibiting involves the exponential up-regulation of the superoxide level, while the non-treated cells demonstrate sigmoidal profile. Having these nonlinear fits of the intensity profiles allows for quantifying important parameters of $O_2^{\bullet-}$ dynamics including $O_2^{\bullet-}$ production rate, which is the slope of the fit in each time point and the $O_2^{\bullet-}$ level that is proportional to the intensity value of the fit at each time point. Moreover, nonlinear fits provide the time constant (T; the time point when the intensity level rises to 65% of the ultimate value, b) of the exponential up-regulation of the mitochondrial $O_2^{\bullet-}$. We also used the slope of the fit exactly after addition of the agent to quantify the initiation of the $O_2^{\bullet-}$ production after each treatment. The quantified parameters of the nonlinear fits (bottom panel of Figure 3-9) suggest that uncoupling of the mitochondrial ETC by PCP leads to the smallest time constant or the fastest rate of $O_2^{\bullet-}$ production and highest levels of $O_2^{\bullet-}$ accumulation compared to

the inhibition of the ETC. Shorter time constant, and therefore significantly higher slope of the exponential fit ($\frac{-b}{T}$) of the PCP-treated cells is an evidence for faster $O_2^{\bullet-}$ generation in the uncoupled chain. The parameter b of exponential fit, which represents the final levels of the accumulated $O_2^{\bullet-}$ is the evidence for the higher $O_2^{\bullet-}$ levels in PAECs with uncoupled chain, consistent with the studies of Aon et al. [277]. Among the inhibitors (Figure 3-10), AA resulted in faster $O_2^{\bullet-}$ production in the early phase of the inhibition of complex III compared to the inhibition of mitochondrial complexes I and IV by ROT and KCN, respectively.

The rate of $O_2^{\bullet-}$ productions was also assessed in ***dual-agent experiments*** to identify the complexes that mediate the uncoupling effect of ETC on $O_2^{\bullet-}$ production and scavenging potential of mitochondrial-targeted (MitoTempol) and non-mitochondrial-targeted (Tempol) scavengers. $O_2^{\bullet-}$ productions from mitochondria are primarily from complexes (I, III, and IV), distinguished by the use of specific blockers (see Materials and Methods) of the ETC complexes. Of the three complexes targeted, only complex IV blocker, KCN, significantly decreased the rate of $O_2^{\bullet-}$ production induced by PCP. This suggests strongly that the uncoupling effect of PCP on $O_2^{\bullet-}$ production is related to increased electron leak to final acceptor, O_2, without generation of H_2O. Thus, in the uncoupled mitochondria, the main source for $O_2^{\bullet-}$ production is probably associated with the oxidation of mitochondria via complex IV. Therefore, a notable observation is that in the PAECs complex IV is a major site for $O_2^{\bullet-}$ production when mitochondria are uncoupled.

Consistent with the redox-optimized ROS balance hypothesis, our method has the potential to model redox as ROS modulator and confirm the important role that redox modulation plays in controlling ROS production and potentially, ROS-mediated mitochondrial dysfunction and concomitant cellular injury. The single agent experiments showed that reduction (inhibition) or oxidation (uncoupling) of ETC leads to exponential increase in ROS production. Therefore, any

shift toward oxidation or reduction leads to an increase in the ROS production rate. As equation 3-9 shows, this ROS production is proportional to the difference of the redox state (R) from its optimal value (Ropt).

$$ROS \sim |R\text{-}Ropt| \qquad (3\text{-}9)$$

In addition, the dual-agent experiments demonstrated the shift in the redox state towards oxidation by PCP, and the reversal of the $O_2^{\bullet-}$ by KCN suggests that the redox optimized balance could be modulated by targeting specific ETC complexes. In this scenario, the redox state (R) of the uncoupled ETC becomes more reduced after adding KCN and moves toward optimal redox state and attenuates ROS production.

Since mitochondria are the major source of $O_2^{\bullet-}$ production during the uncoupling of respiration with PCP, we also examined whether the initial surge in $O_2^{\bullet-}$ production was amenable to the mitochondria-targeted ***ROS scavenger***, MitoTempol and the cytosolic counterpart Tempol. Mito-Tempol, unlike Tempol, is hitched to the cationic agent TPP+, which pulls the scavenger into mitochondria where it acts as an effective SOD mimetic. Our results (figures 3-12 and 3-13) confirm that the initial surge in mitochondrial ROS production following uncoupling of respiration with PCP is primarily mediated by the deranged electron transfer in the ETC. This is also consistent with the observation that the complex IV might be the source of electron leak that contributes to the surge in $O_2^{\bullet-}$ generation in the initial phase, i.e. when production exceeds the scavenging potential of MnSOD. We further verified that the primary source of the $O_2^{\bullet-}$ anion during simulation of metabolic stress is from the mitochondria, because the Nox inhibitor, apocynin, did not alter the cellular ROS production (data not shown).

The dynamics of superoxide production rate was quantified and compared in inhibited PAECs isolated from ***Persistent Pulmonary Hypertensive lamb*** and normal lamb. Our result

demonstrated that administration of the KCN significantly doubled and tripled the superoxide production rate in NFL and HTFL PAECs, respectively. Compared to NFL PAECs, addition of KCN induced significantly greater increase (double) in the superoxide production rate of the HTFL PAECs [31]. This result is consistent with decreased manganese superoxide dismutase (MnSOD) expression and activity contribute to the endothelial dysfunction observed in PPHN [116]. Our results suggest that pulmonary hypertension is associated with lower basal superoxide level and greater mitochondrial superoxide production rate.

Hypoxia as a severe oxygen stress causes irreversible injury to lung cells. However, under stress condition due to other injuries or metabolic stressor, hypoxia can decrease the severity of the original injury [111]. This effect was examined by quantifying $O_2^{\bullet-}$ production rate in hypoxic PAECs treated with PCP. Our results revealed that hypoxic cells have smaller dynamic range of the superoxide generation when treated with PCP. While treating with PCP leads to an increase of 4.9 ± 0.5 times greater $O_2^{\bullet-}$ production rate in normal cells, it increases this rate by a factor of 2.7 ± 0.2 in hypoxic cells. This result indicates 45% decrease in the $O_2^{\bullet-}$ production rate of uncoupled PAECs under hypoxic condition when compared to normal oxygen condition. The decrease in $O_2^{\bullet-}$ production rate suggests a slower rate of electron transfer along the ETC and hence a slower activity of uncoupled chain in hypoxic condition which leads to a less oxidized chain. Decreased activity of the uncoupled ETC in hypoxic condition demonstrates that lower concentration of ambient oxygen decreases the severity of the metabolic stress and mitochondrial dysfunction. This happens through a compensating mechanism which regulate $O_2^{\bullet-}$ production rate leading to a more resistive state to metabolic stress and injury.

The ***IR model*** leads to more enhanced $O_2^{\bullet-}$ production (4.4 ± 0.7) compared to hypoxia (2.7 ± 0.2) leading to less resistive state in response to metabolic stress condition, uncoupling. This

result revealed that reoxygenation after hypoxia oxidizes ETC and thus the $O_2^{\bullet-}$ production rate increases to the $O_2^{\bullet-}$ production rate of uncoupled ETC (4.9 ± 0.5). This is consistent with previous results which demonstrated an oxidized ETC in lungs sustained IR [296, 297]. This results also confirms that IR is an injury model leading to oxidative stress and mitochondrial dysfunction.

Limitations: We relied on the concept that MitoSOX is oxidized by $O_2^{\bullet-}$ and the oxidation product becomes highly fluorescent upon subsequent binding to mitochondrial DNA over time [243]. It is possible that as a cationic molecule, MitoSOX uptake into mitochondria can also contribute to direct ROS production by depolarizing $\Delta\Psi_m$. However, the ROS generated in this case is minute when compared to the ROS produced from modulating ETC complexes. Using lower concentration of the MitoSOX in nano-molar range provides a longer time interval for the study and decreases the effect of the MitoSOX on the Mitochondria.

It should also be noted that MitoSOX uptake increases 10 fold for every 60mv increase in membrane potential [243, 298]. Since $\Delta\Psi$m decreases in the presence of uncoupler [299, 300] and ETC inhibitors [299, 301], the decrease in $\Delta\Psi$m could impede the uptake of MitoSOX. Therefore, the fluorescence intensities presented could be under-estimated for the levels of the ROS in the inhibited and uncoupled chain.

Interaction of the $O_2^{\bullet-}$ and MitoSOX is also affected by pharmacokinetics of MitoSOX and its binding properties. The initial phase of the intensity profile shows a greatly enhanced fluorescence due to binding of the oxidized MitoSOX to mitochondrial DNA. In the steady state phase of the fluorescence recording, the saturation effect of the signal profile is possibly due to binding of oxidized MitoSOX to nuclei, which results in apparent nuclear and nucleolar localization (Figure 3A). Due to nuclei binding of MitoSOX and thus, the subsequent diminished

mitochondrial uptake, the fluorescence intensity of the mitochondrial compartment become saturated and after a while reaches the final level.

The mitochondria-derived $O_2^{\bullet -}$ detection can be also further improved by high resolution 3D imaging, segmenting the mitochondria of the cells in the 3D red fluorescent images, and quantifying the intensity profile of the mitochondrial compartment.

3.3 Summary

In closing, *fluorescence microscopy* was used to quantify the changes of (1) vascular morphologies in retina and (2) cellular ROS in lung cells in the early phase of their response to ROS-mediated injuries. *In the first approach*, vascular network of the mice retina including vascular area, acellular capillaries, vascular fractal dimension, and more specifically vascular cells, were assessed on the *fixed microscope slides*. A multi-parameter image processing tool was developed to quantify the subtle changes in retinal vascular network due to injury and oxidative stress. The developed program was also able to classify the injured and healthy retinas. *In the second approach*, a new experimental protocol was established to study oxidative stress in *live lung cells*. Part of the image processing program developed for retina cell studies was used to segment the lung cells from fluorescence microscopic images, which shows the capabilities of the developed programs and can also be applied to other applications. The image processing tool was further developed to model and quantify the cellular response of the lung cells to the injuries and stress conditions. The details of both approaches were explained and the results were discussed.

Chapter 4

Ex vivo studies of lung in animal model

4. *Ex vivo* studies of lung in animal model

Pulmonary diseases are the third leading cause of death in America [302]. A wide range of lung diseases affect the structure of the alveoli, leading to deterioration of the lung function. For instance, pulmonary edema, hyperoxia, pulmonary fibrosis, restrictive and obstructive pulmonary disease are known by the progressive destruction of alveolar lining layer and wall. Chronic obstructive pulmonary disease (COPD) is defined by the progressive destruction of alveolar walls leading to permanently dilated alveoli. In contrast, pulmonary fibrosis is characterized by causing stiffening and, thus, impeding alveolar dilation [303]. Prolonged hyperoxia also causes impaired alveolization leading to alveolar dilation as well as a decrease in the number of alveoli [304]. Moreover, hypoxia and alveolar edema activate a hyperventilation mechanism to compensate for the lack of oxygen. Prolonged hypoxia and edema cause impaired alveoli. Therefore, evaluation of the structural changes in lung tissue, and particularly alveolar sacs and wall, provides diagnostic information about these pulmonary diseases and the severity of the lung injury sustained.

The recognition of the crucial role of the alveolar structure dynamics rekindled significant interest in the development of methods to image and assess the alveolar wall damage in the lung and the severity of the disease. A developed spectral domain - optical coherence tomography (SD-OCT) device was utilized to image the underlying structure of lung tissue including alveoli in real-time fashion. Furthermore, an automated segmentation and quantification algorithm for the quantification of alveoli structures in optical coherence tomography images was implemented.

Our implemented software is able to provide 3D visualizations of the alveolar sacs and to quantify the changes in alveoli compliance in the lung injury models. Our method allows for the evaluation of alveoli compliance on lung tissue acquired at different levels of expansion. This method has the potential to provide structural remodeling caused by a range of respiratory diseases, including pulmonary alveolar edema, chronic obstructive pulmonary disease and pulmonary fibrosis.

This chapter will now go through the methods, experimental setup, data analysis and results of the lung studies performed for this project.

4.1. Tissue Preparation

4.1.1. Rat lungs

Lungs were harvested from anesthetized rats weighing 300 to 350g and were perfused as previously reported [305]. Each rat was anesthetized with pentobarbital sodium (40 mg/kg body wt. intraperitoneal), after which the chest was opened. Heparin (0.7 IU/g body wt.) was injected into the right ventricle. Cannulas were placed in the pulmonary artery and the trachea, and the pulmonary venous outflow was accessed via a cannula in the left atrium. The lungs were removed from the chest and attached to a ventilation and perfusion system. The perfusate was Krebs-Ringer bicarbonate solution containing (in mM) 4.7 KCl, 2.51 $CaCl_2$, 1.19 $MgSO_4$, 2.5 KH_2PO_4, 118 NaCl, 25 $NaHCO_3$, 5.5 glucose, and 3% bovine serum albumin (BSA) [306]. The ventilation gas mixture was 15% O_2, 6% CO_2, balance N_2. The perfusate was pumped (at 10 mL/min) through the lung until it was clear of blood, then SD-OCT scans and spectral signal acquisition were performed under resting conditions.

4.1.2. Pulmonary alveolar edema

The primary function of the lungs is the diffusion of oxygen into and the release of carbon dioxide from the bloodstream. Air-filled sacs in the lung, called alveoli, facilitate this exchange of gases. Alveolar edema which is a pulmonary edema in the alveoli can be developed by hypoxemia (hypoxia), and dyspnea in different ways. In 1974, Webb and Tierney demonstrated for the first time that mechanical ventilation could generate lung lesions in intact animals [307]. Rats ventilated with peak inspiratory pressures of 30 or 45 cm H_2O (22-33 torr) developed pulmonary edema within 60 and 20 min, respectively [308]. This method was used to make the normal rat lung, edemic. After compliance experiment was performed on the normal rat, the lung was ventilated with peak inspiratory pressure of 22 torr for 60 min and developed alveolar edema. Then, the compliance experiment was repeated on the edemic lung.

4.2. Pulmonary compliance experiment

Pulmonary compliance is a measure of the ability of the lung to stretch, and it is assessed by quantifying the changes in lung volume due to continuous increase and decrease in the airway pressure. The pressure-volume (PL-VL) curve of an excised lung inflated-deflated between

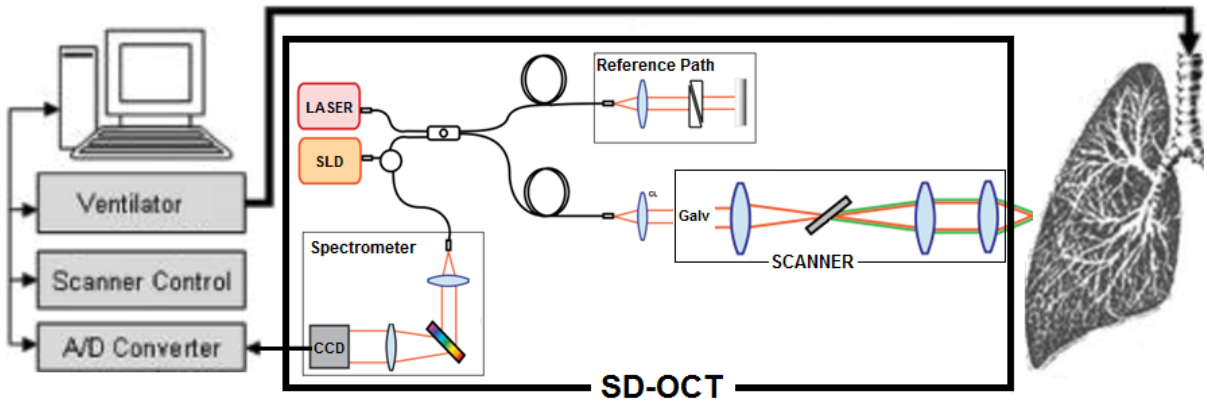

Figure 4-1: Experimental setup for the compliance experiments

minimum lung volume and total lung capacity is characterized by a nonlinear relationship and is typified by a large hysteretic area indicating an irreversible energy loss. The mechanical behavior of excised lungs is associated with an irreversible behavior linked to structural alterations in the lung tissue. In order to see the dynamic change of structure, SD-OCT data were collected from the surface of the buffer perfused and ventilated rat lungs at different ventilator pressures from 0 to 11 torr. For the deflation, expiration pressure was decreased from 11 torr to zero. Figure 4-1 shows the setup for the compliance experiments. Controlling the scanner, collecting lung data, and ventilator pressure are managed through a software. The details of the SD-OCT system are described as follows.

4.3. OCT instrument

A spectral-domain optical coherence tomography (SD-OCT) system was designed and implemented by our collaborator in the BIST lab (of UW-Milwaukee) to monitor microvasculature activity which incorporates rapid hemodynamic, fluorescent and metabolic imaging. The system was optimized for real-time imaging to monitor hemodynamic activity. The enhanced capability of the system can provide imaging rates of 80 (2D) images (1000 × 512 pixels) per second. This high-speed tool will allow for real-time microvasculature monitoring at video rates. Additional fluorescent image modalities can coordinate fluorescent signals with hemodynamic reactions.

The optical setup of the SD-OCT system (figure 4-2) used for alveolar imaging is based on a low coherent light source, which is a broadband near-infrared super-luminescent diode (SLD) with a 200-nm-wide spectrum centered at 1300 nm. Output power of SLD is coupled into a single-mode optical fiber. After passing a fiber coupler joining the pathways to the SLD and to the spectrometer, the light is guided to a scanner. In the scanner, the light is collimated to a free space

beam and deflected from a set of galvanometer mirrors providing fast beam deflection. The deflected beam is transmitted through a dichroic mirror and then focused on the sample by an objective lens. The other arm serves as the reference pathway for the OCT interferometer. The light reflected by scattering structures within the probe, together with the reference light, form the interference pattern relative to position and is focused back into one common fiber and guided via the fiber coupler into the grating spectrometer, where the dispersed light is focused on a InGaAs line detector with a width of 1024 pixels. The resulting interference spectrum is read out to a personal computer at a maximum rate of 91 KHz. To control all of the hardware used, as well as data acquisition of OCT spectra, and display them in real time, a LabVIEW program has been designed.

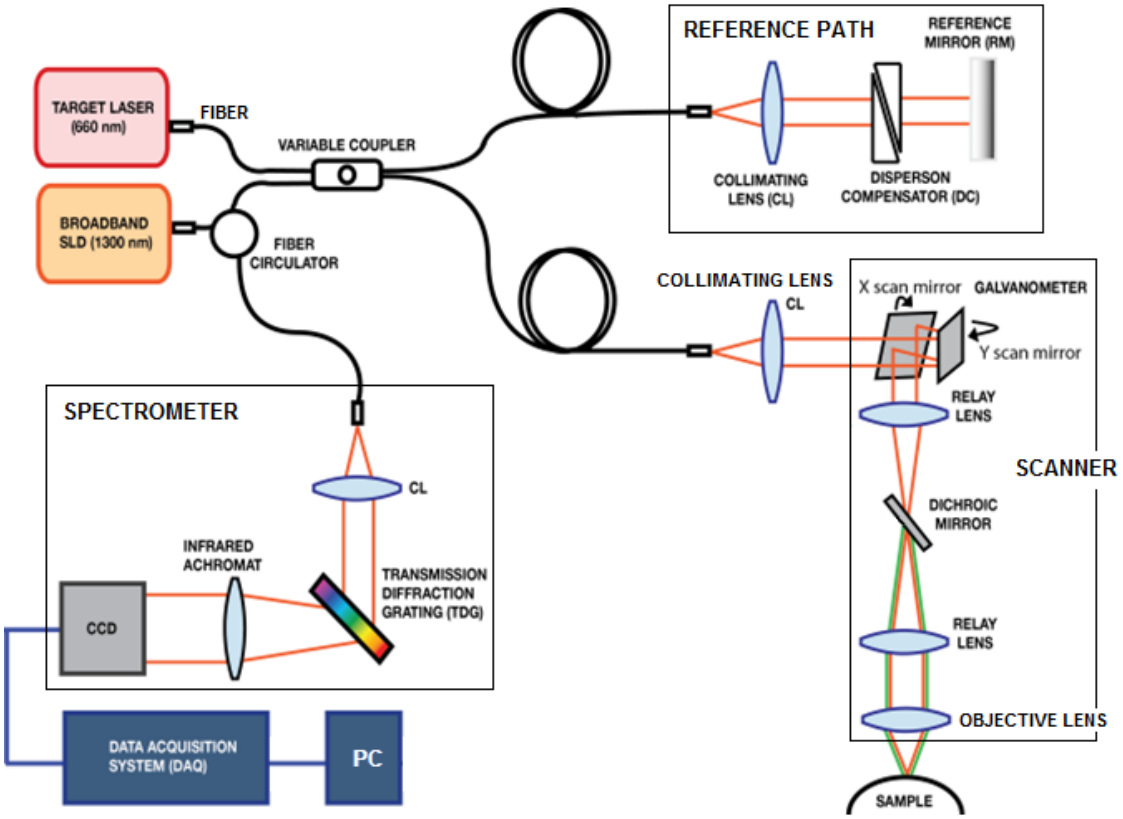

Figure 4-2: Schematic of the spectral domain OCT

4.4. Imaging and image processing

The SD-OCT system was utilized to capture real-time cross sectional images of lung and, thus, alveolar structure in a ventilated and buffer perfused isolated rat lung. The ability of the OCT system to provide depth information makes it a promising tool for disease diagnosis and tumor investigation. To our knowledge, there has been no report so far on OCT imaging of alveolar compliance dynamic in rat lungs. Using image processing techniques, the structural changes in the alveoli and the compliance were quantified and monitored.

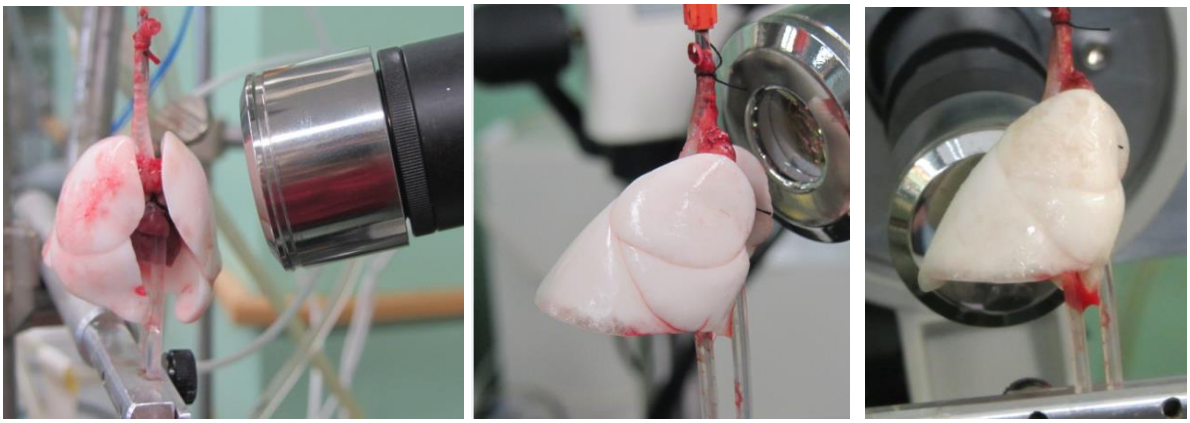

Figure 4-3: Images of the scanner head during *ex-vivo* experiments on the normal (left) and edemic on edge (middle), and severe edemic (right) lungs attached to the Langendorff perfusion system

4.4.1. Imaging and image acquisition

Figure 4-3 shows perfused and ventilated lungs (both normal and edemic rat lungs), which were scanned under resting condition by the described SD-OCT system. The raw data, which is the spectrum of the interference patterns relative to different lateral positions, were collected from the surface of the fixated lung and stacked together to produce a 2D cross-sectional image.

For lung compliance experiments, SD-OCT data collected from the surface of the normal and edemic rat lungs ventilated at different pressures from 0 to 11 torr. A stack of 2D cross sectional images with field of view of 3 mm × 3 mm (figure 4-4a) were obtained by the SD-OCT

system. Due to curvature of the lung surface, some part of this image is in focus and some parts are out of focus. Therefore, only in-focus field of view of this image (figure 4-4b) was selected for the processing. Then, a processing algorithm was applied to segment the contour of the alveolar sacs (highlighted with green lines in figure 4-4c) and to extract the whole information relevant to these contours.

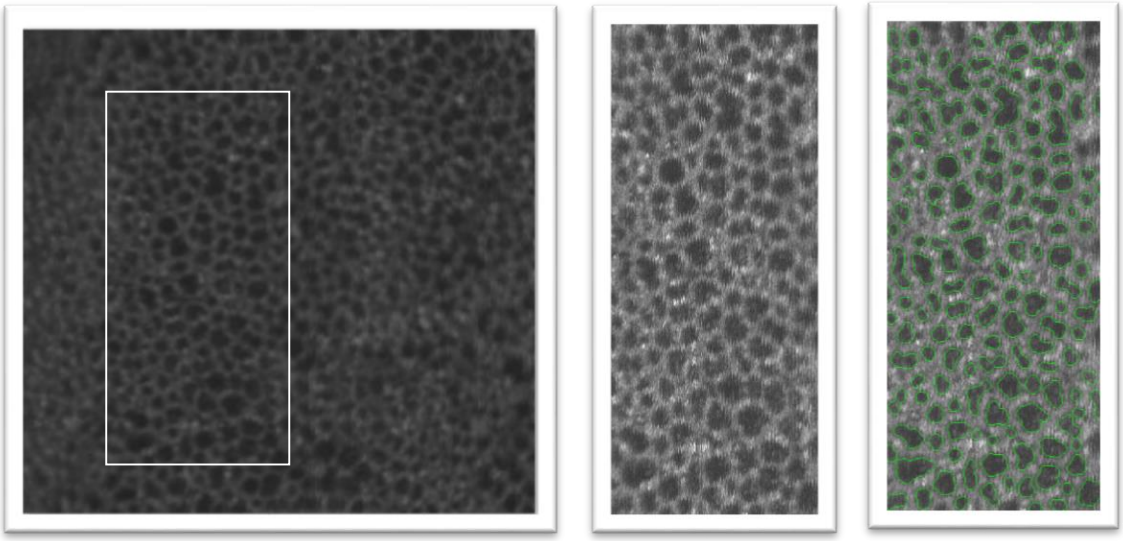

(a) (b) (c)

Figure 4-4: Extraction of the alveolar sacs from the raw image produced by the SD-OCT system. a) A 2D cross sectional OCT image at the depth of 63µm from the surface of lung. The white rectangle shows the area of which is in focus and segmentation was applied, b) selected area after contrast enhancing, c) detection of alveolar sacs on the selected area.

4.4.2. Image processing

3D visualizations: To present 3D visualizations of the lung structures, first the 2D cross sectional images were reconstructed through a multi-step process. Acquired raw data transformed from the frequency domain (the interference pattern) to time domain to reconstruct an A-scan. After background subtraction, noise removal, and contrast enhancement, A-scans obtained from different lateral positions are stacked together to produce a 2D cross-sectional image. Surface scans performed on each spot (with field of view of 3 mm × 3 mm) of a rat lung at each ventilation

pressure point resulted in a stack of 2D cross sectional images. Then, a 3D image was rendered from the preprocessed stack of images.

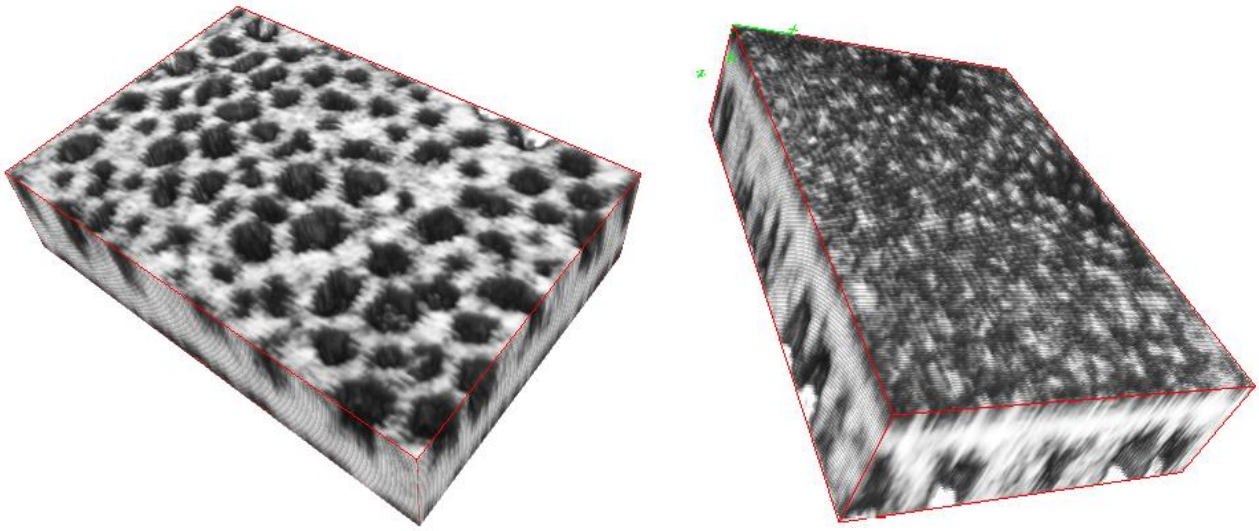

(a) (b)

Figure 4-5: 3D reconstructed image of the lung alveoli. a) alveolar sacs (bottom) view; b) lung surface (top) view

Figure 4-5 shows 3D rendered visualization of the reconstructed images acquired from surface scanning of a normal rat lung. These visualizations show, to our knowledge, the first 3D volume renderings of rat lung structures acquired with an OCT system. In these visualizations, the structures of the alveolar wall and sacs were clearly presented (figure 4-5a).

Alveoli segmentation: A segmentation technique was developed to detect the contour of the alveolar sacs in the 2D cross sectional images. Segmented contours provide the structural dynamic information, which were quantified for both normal and edemic lungs.

The segmentation program utilizes the 2D cross sectional images to detect the alveolar sacs in the images. The location and the border of the alveoli in each image was determined using the segmentation algorithm shown in figure 4-6 as a schematic, and figure 4-7 as example pictures.

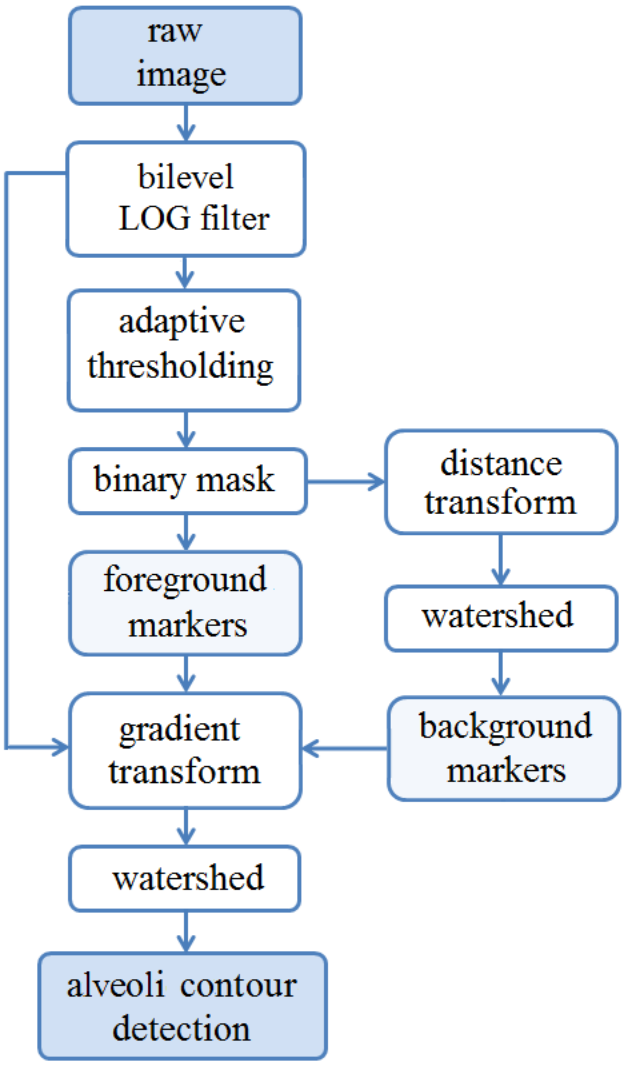

Figure 4-6: Flowchart of the alveoli segmentation procedure.

The segmentation algorithm shown in figure 4-6 is a marker based watershed technique [55]. Since the objective of the present segmentation algorithm is to find the border contours of the alveolar sacs, we defined a marker for alveolar sacs as foreground and a marker for the alveolar walls as background. The gradient of the images was calculated and the magnitude of this gradient

considered as the segmentation function. To avoid over-segmentation problems [309, 310], the segmentation function was modified based on the foreground and background markers. To enhance the contrast of the circular sacs (foreground markers), a bilevel LOG filter [311] was applied (using the center and surround method). The background markers (alveolar walls) were computed by applying distance transform and then watershed detection on the resultant binary mask of the previous stage. The gradient magnitude of image was then modified so that only its regional minima occurred in the foreground and background markers' pixels. At this stage, the watershed transform [312] of the modified segmentation function finds and uses the markers as the "catchment basins" and the border of the foreground markers as "watershed ridge lines", resulting in a binary mask containing the borders of the alveolar sacs.

It should be noted that defining background marker is necessary. Otherwise, watershed transform results in segmenting some part of the alveolar wall and background of the image as alveoli sacs. It is also important to define the background markers such that they are not too close to the edges of the foreground markers that we are trying to segment. To avoid this problem, the background was thinned by computing the "skeleton by influence zones", or SKIZ [313], of the foreground. This can be done by computing the watershed transform of the distance transform (DT) of the foreground. DT transforms each pixel value into the distance to the nearest alveolus. Therefore, as figure 4-7d shows the brightest pixel in the resulting image show the farthest pixel from the nearest alveoli. Watershed in this case detects the ridge lines which defines areas with the maximal distance to the nearest alveoli. Therefore, the resulting background markers are the lines that separate the image into individual regions, while maintaining the maximum distance from the nearest alveoli (figure 4-7e).

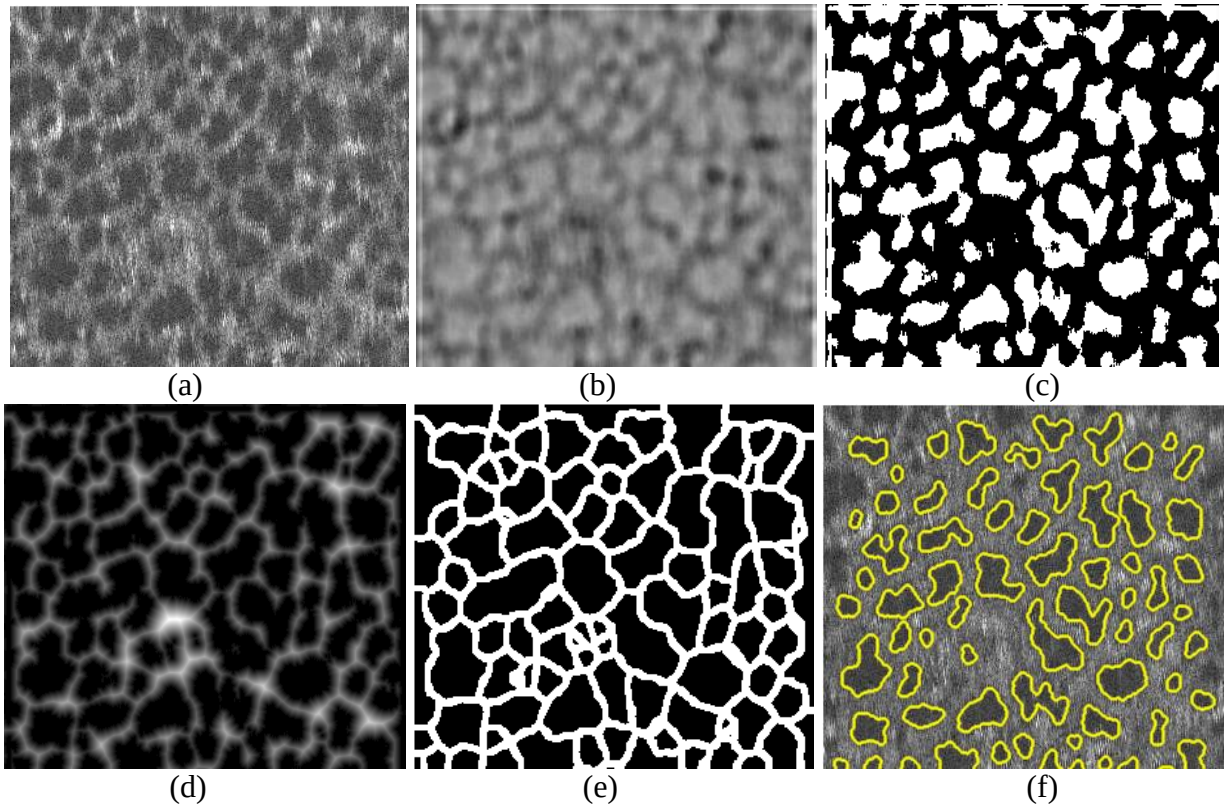

Figure 4-7: Output of the segmentation algorithm in different stages. a) original image; b) filtered image by bilevel LOG filter; c) foreground markers: binary mask resulted from Otsu thresholding; d) distance transform of the binary mask after morphological reconstruction; e) background markers obtained by watershed transform of stage d; f) segmented alveolar sacs in yellow contours.

Large variations of intensity within and between the alveolar walls make accurate segmentation difficult. This challenge is further increased by the need for high-speed operation for the real time monitoring. Enhancing the object-background contrast by using a fast and effective filter helps to overcome this challenge. As mentioned earlier, a bilevel LOG filter was implemented in this study to sharpen the edges and enhance the contrast of the circular objects of the images (alveolar sacs).

The filter is specified by four parameters H_1, H_2, R_1, and R_2:

$$f(r) = \begin{cases} H_1, & |r| \le R_1 \\ H_2, & R_1 < |r| \le R_2 \\ 0 & |r| > R_2 \end{cases} \qquad (4\text{-}1)$$

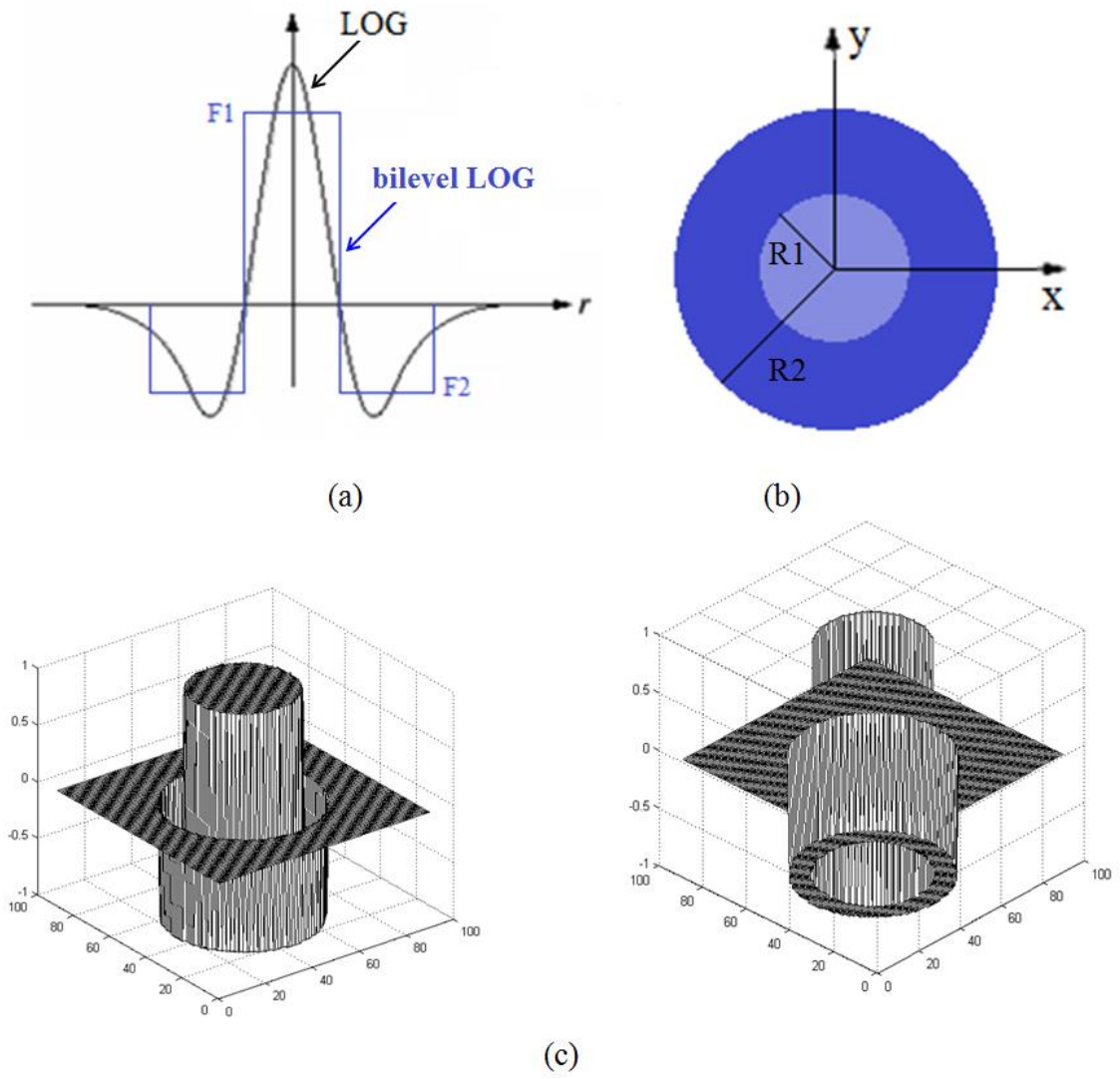

Figure 4-8: (a) Bilevel LOG filter in blue color (b) top view of filter C) two different side views of the implemented filter.

Different views of this filter have been shown in figure 4-8. The size of the filter, which is defined by R_1 and R_2, was computed based on the minimum and maximum size of the alveolar sacs (objects of interest). H_1 and H_2 are the amplitude of the filter in the corresponding regions. The LOG filter is an orientation-independent operator and is optimal for edge detection but not computationally efficient, especially for high throughput assessments. Bilevel LOG filter approximates LOG filter to only two levels (H_1 = +10, and H_2 = -10) and improves the speed of the filter [311], making it more useful for our application. This filter emphasizes circular objects

by leaving pixels in a central circle $|r| \leq R_1$ magnified by a factor of H_1, while reversing pixels outside of the central circle $R_1 < |r| \leq R_2$ by a factor of H_2 to create a high contrast around circular objects in the image.

The performance of the alveolus segmentation algorithm depends on the choice of several parameters, which should be tuned to obtain optimal performance of the algorithm. The first of these parameters are R_1 and R_2, which define the size of the filter used to improve the alveolus contrast. Initialization of these parameters was determined by a prior estimate based on the size of the alveoli in a set of manually segmented (ground truth) images. Another parameter is the threshold level, which was used to convert the image intensity to a binary mask containing the alveolar sacs. The initial value for the threshold level was computed based on Otsu's method [314], which selects the threshold to minimize the intraclass variance of the thresholded black and white pixels. After initialization, these parameters will be selected in an interval around the initial values so that the segmentation error decreases. The error in the alveolus count was defined as the criterion for determining the segmentation error.

Before applying the segmentation algorithm to detect alveolar sacs, morphological reconstruction methods including closing and opening were applied to enhance the shape of foreground markers (alveolar walls) and minimize the segmentation error. Moreover, the post processing was performed to quantify the parameters of interest including, 2D area of each alveolus, the total area of alveoli, the distance between all two points of each alveolar wall, maximum, minimum, and average diameter of alveolar sacs and the total number of alveolar sacs. The 2D area of each alveolus was calculated by summing the number of the white pixels within each contour of the binary image.

4.5. Results

4.5.1. Alveolar structure segmentation

3D OCT scans were taken from different spots of rat lung lobes. Figure 4-4 showed one of the best images acquired by the OCT scans. However, the OCT images have the average quality shown in top panel of figure 4-9. In these images, the contour of the individual alveolus cannot be clearly seen. The implemented segmentation algorithm, however, was able to detect the contours of the alveolar sacs with an accuracy of 98.6% compared to manual detection. The bottom panel in figure 4-9 shows the segmented alveolar sacs in yellow color. The segmentation algorithm is capable of finding the contour of each alveolus and calculating the 2D cross section area of each alveolus, the total area of alveoli, maximum, minimum, and average diameter of alveolar sacs in the image and the total number of alveolar sacs.

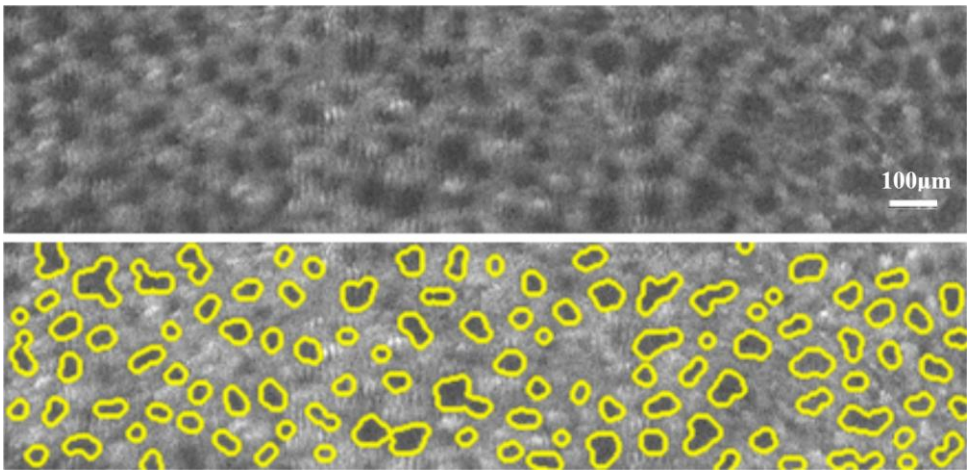

Figure 4-9: Top: Average quality 2D image of lung alveoli at a depth of 75 µm from 450 g five months old rat captured and reconstructed by SD-OCT in the ventilated pressure of 5 torr. Bottom: Yellow contours show segmented alveolar sacs. Total number of alveoli in this image is 106, 2D cross section area of an alveolus is 4070 $(\mu m)^2$ on average, and diameter of the alveolus is 72 µm on average.

4.5.2. Alveolar compliance results

In order to see the dynamic change of structure, SD-OCT data were collected from the surface of a buffer perfused and ventilated rat lung at different ventilator pressures: 2.5, 5, and 6.5 torr. The images were reconstructed and the segmentation algorithm was applied so that the structural changes of the lung could be extracted. Figure 4-10A shows the histograms of alveoli diameters at aforementioned pressures. As expected, alveoli diameter changes according to ventilator pressure. The higher the driving pressure, the greater alveoli diameter. Figure 4-10B shows the measured normalized alveolar volume as blue points together with a linear curve fit of alveoli volume versus ventilator pressure. The slope of the linear fit can also be seen in the figure, and this slope differs for diseased (edemic, obstructive, and restrictive) lungs compared to normal lungs, and can help to classify lung diseases.

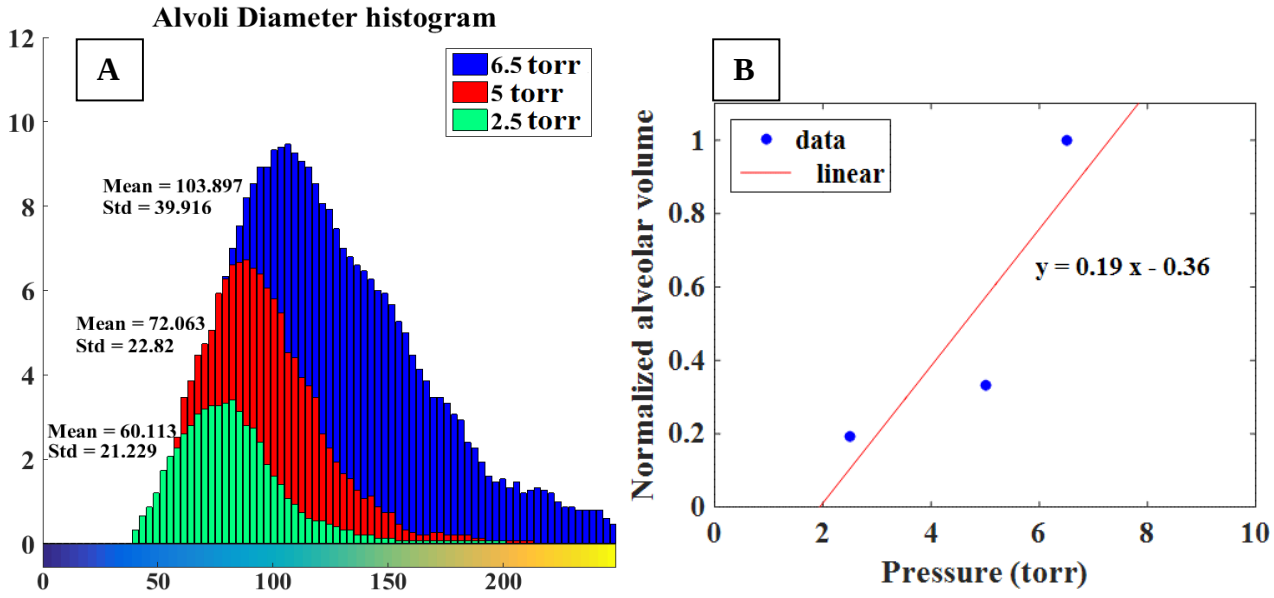

Figure 4-10: A: Histograms of alveoli diameter (μm) at three pressures: 2.5 torr (green), 5 torr (red), 6.5 torr (blue). B: Linear curve fitting of alveoli volume versus pressure. Lung was harvested from 450 g five months old rat.

Compliance experiments were repeated for normoxic lung versus edemic lung from two months old rats (n=2) weighing 300 and 350 g. Dynamic OCT scans of lungs undergoing simulated expiration were performed and a sequence of lung scans at different stages of alveolar compression was acquired for normal and edemic lung. Figure 4-11 demonstrates the SD-OCT reconstructed images. The structural dynamic was quantified after applying segmentation algorithm and was compared between edemic and normal lungs at predefined lung pressure of 8.1 torr. This figure displays that the edemic lung (top panel) has smaller alveoli diameter and smaller cross sectional area when compared with the normal lung (bottom panel). Total number of alveoli in a specific FOV of *normal* lung was 243, 2D cross section area of an alveolus was 2249 $(\mu m)^2$ on average, and the average diameter of an alveolus was 63.5 μm. However, in the same field of view, *edemic* rat lung had 222 alveoli, 2D cross section area of an alveolus was 1843 $(\mu m)^2$ on average, and the diameter of an alveolus was 58 μm on average.

The expiration compliance of the normal and edemic lungs versus pressure are shown in figure 4-12. Alveolar expiration compliance is a measure of the ability of the alveoli sacs to stretch, and it is assessed by quantifying the changes in alveolar volume due to continuous decrease in the airway pressure. The slope of the line fitted to the compliance data points was calculated for the edemic and normal lung. Results showed a decrease of 40% in the slope of the edemic compliance when compared with the slope of the normal compliance [2].

Figure 4-11: 2D images of alveoli from *ex vivo* rat lung captured and reconstructed by SD-OCT at a depth of 83 μm and a ventilated representative pressure of 8.1 torr. Top: Green contours show segmented alveolar sacs in the *edemic* rat lung. Total number of alveoli in this image is 222, 2D cross section area of an alveolus is 1843 $(\mu m)^2$ on average, and diameter of an alveolus is 58 μm on average. Bottom: Purple contours show segmented alveolar sacs in the *normal* rat lung. Total number of alveoli in this image is 243, 2D cross section area of an alveolus is 2249 $(\mu m)^2$ on average, and diameter of an alveolus is 63.5 μm on average [2].

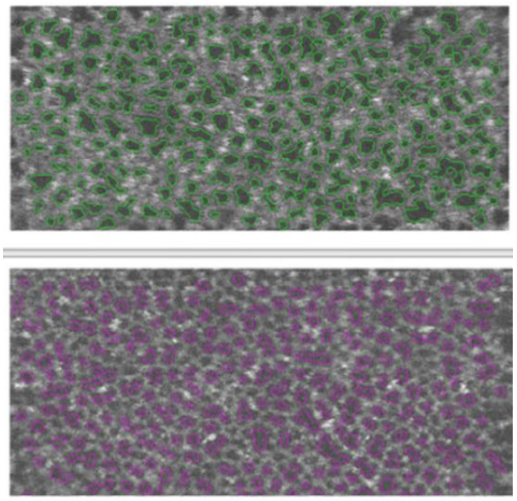

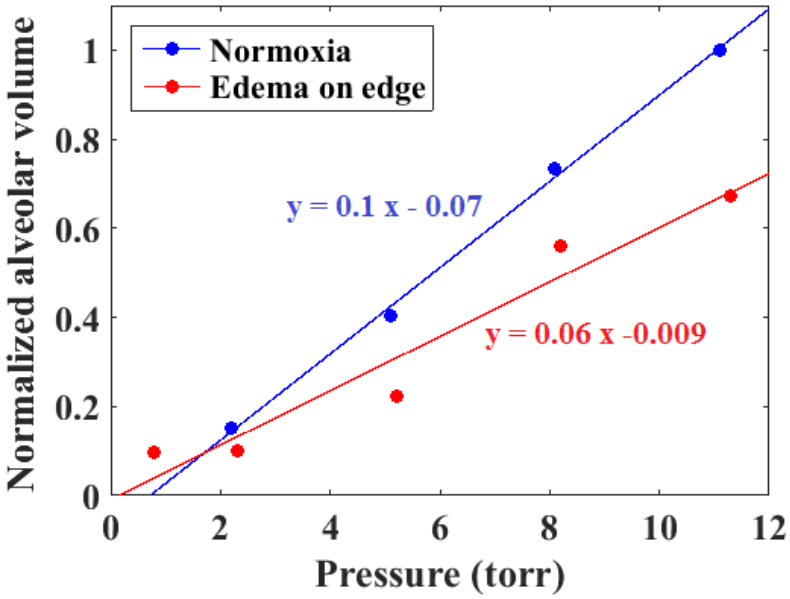

Figure 4-12: Alveolar expiration compliance of edemic (red color) and normal (blue color) rat lungs [2].

4.6. Conclusion

Spectral domain OCT was utilized to monitor and study the structural dynamics in lungs in real-time fashion. A fast image processing algorithm was developed to quantify the morphological changes in lung for disease diagnosis purposes. The ability of this technique was

verified by quantifying the dynamic changes of alveolar morphology in a rodent injury model of pulmonary edema. Our method detected alveolar structure and statistically (within each set of images from 2 rats of each group) quantified four parameters, including diameter and area of each alveolus, total number of alveolar sacs, and alveolar compliance. Alveolar expiration compliance was quantified by computing the alveolar morphology of the *ex vivo* lung acquired at different levels of expansion and compression.

Automated quantification of the alveoli compliance from SD-OCT images revealed a decreased compliance in edemic lung when compared to the normal lung. The reason behind lower compliance of the edemic lungs lies on the mechanical stress which liquid-filled alveoli induce on air-filled alveoli. Reducing the compliance of air-filled alveoli results in a decreases in the overall lung compliance.

Dynamic OCT scans of lungs undergoing simulated respiration at predefined lung pressures combined with our fast quantification software demonstrated the practicality of our method and showed its potential in the evaluation of alveoli compliance in a range of diseases. Quantification of lung and alveoli structure dimensions at each pressure, and changes across pressures, could provide an indicator of changes in tissue compliance due to tissue remodeling, which is significant in diseases such as edema, emphysema and pulmonary fibrosis.

Chapter 5

Conclusion and future work

5. Conclusion and future direction

This thesis has explored different optical techniques to quantify the effect of the oxidative stress due to injury on the cellular structure and physiological responses in eyes and lungs. The novel approaches presented in this thesis have shown the ability for quantitative detection of mitochondrial dysfunction due to injuries and stress conditions in tissue and cells.

The following four sub-sections present conclusion and outlook for each optical imaging technique.

5.1 Cryoimaging

The results of our cryoimaging studies demonstrate the quantitative capability of the optical cryoimaging technique to measure the retina mitochondrial redox state. Optical redox imaging yields a direct analysis of the cellular metabolic state within the mitochondrial compartment of the retina from animal model of diabetes, retinitis pigmentosa, OIR, and HHT1, which have not previously been reported. Our cryoimaging research showed a significant difference in the redox state of healthy and injured eyes, confirming the application of this technique in diagnosis of ocular injuries. Apart from expanding the application to a wide variety of injuries and diseases, it is possible to use this as a technique to investigate the progress of the injury or the effect of therapy over time.

Optical redox imaging is also helpful to study the effect of the gene manipulation and deletion on the eye metabolism. Our results revealed that the endoglin gene maintains the oxidative state in retina and knocking out this gene makes the retina more resistive to the ROS and reduces its metabolic redox state. However, other injuries investigated in this research, including diabetes and retinitis pigmentosa, showed an increase in the redox state and more oxidized chain. Our study

also showed a significant difference in the mean redox ratio of eyes with and without endoglin haploinsufficiency in both room air and OIR conditions. This result discloses the essential role of reactive oxygen species and the effect of the ambient oxygen concentration on the metabolism and hence cellular activities including angiogenesis.

These results will inspire future studies that will allow researchers to establish a diagnostic tool for early detection of different diseases and a correlation between retinal degeneration and changes in the RR levels, as a marker of oxidative stress caused by disease progression. Furthermore, the studies presented in this thesis set the stage for future studies, using *ex vivo* and *in vivo* fluorescence imaging of mitochondrial redox states of retina to characterize disease progression in various retinal dystrophies and to evaluate mitochondria targeted drug regimens that diminish oxidative stress.

5.2 Image cytometry

Automated multi-feature quantification of diabetic retinopathy and retinal vascular changes in retinal trypsin digests samples was studied. Diabetic retinopathy is a progressive disease and many of the early changes associated with vascular dysfunction go undetected due to our inability to discover such changes early on. The multi-parameter method described in this thesis provides an opportunity to get a comprehensive view of retinal vasculature at the cellular level. Therefore, with advancements in new imaging modalities with cellular resolution it will be possible to utilize the method developed here for quantitative evaluation of retinal vasculature with significant accuracy. This knowledge will be instrumental in development of new treatment modality to stop the development and progression of the disease and save vision.

Our novel quantification method measures subtle retinal vascular changes, which are markers of *early* microvascular dysfunction during diabetes and/or diabetes development. These markers include cell count, EC/PC ratios, fractal dimension, the vessel coverage, and acellular capillary count of the images. Segmentation of images containing touching and overlapping cell nuclei is the most difficult stage for quantitative cell segmentation, and it is the subject of the future work to improve clustered cell segmentation algorithm. We hope that by using multi-phase active contour technique and considering multiple level set functions, each individual cell type and cell cluster can be segmented. Therefore, the error of the automatic cell counting and distinguishing the cell type due to clustered cells can be further reduced.

5.3 *In vitro* time lapse microscopy

Using fluorescence time lapse microscopy, a novel approach was provided to partition and quantify the dynamics of $O_2^{\bullet-}$ production from ETC complexes under different simulated metabolic stress conditions in intact live cells, for the first time. This approach has far-reaching implications for assessment of ROS in physiology and pathophysiology. Measuring the $O_2^{\bullet-}$ dynamics, particularly in the *early phase* of the stress response could lead to future studies extending the approach to situations that would allow us to establish a diagnostic tool for assessing the role of the mitochondrial ROS in different diseases.

Utilizing this novel approach and fluorescence microscopy, ROS dynamics was assessed in PAECs due to the metabolic modulation (to mimic pathological ROS emission), injury (persistent pulmonary hypertension; PPHN), and oxygen tension (hypoxia, IR). ROS-mediated injuries including hypoxia and IR were modeled with hypoxic environment in microscope top incubator. Metabolic modulation, pulmonary hypertension, and IR demonstrated greater mitochondrial

superoxide production rate. However, uncoupled ETC in hypoxic condition showed that lower concentration of ambient oxygen decreases the severity of the metabolic stress and mitochondrial dysfunction. This phenomenon shows the potential of the hypoxia therapy for the lung injuries including hyperoxia and PPHN, and it is our next step to further expand this research. It is also predicted that hyperoxic condition may exacerbates the severity of lung injury in PAECs by modulating superoxide levels produced. Furthermore, it is intended for future studies to monitor the behavior of the injured PAECs under long hypoxic conditions followed by hyperoxic conditions to investigate the effect of the ambient oxygen concentrations on the severity of the injuries lung sustained. Studying a hypoxic condition followed by a hyperoxic condition is also advantageous in another aspect as well, since it simulates the birth transition of the fetal lung for the PAECs. The immature lung of the fetus that develops in moderate hypoxia in-utero, might be more vulnerable to other injury in the relatively hyperoxic extra-uterine environment.

5.4 *Ex vivo* OCT imaging

Spectral domain OCT in combination with a fast image processing algorithm was utilized to monitor and study the structural dynamics in lungs in real-time fashion. The ability of our technique was verified by quantifying the dynamic changes of alveolar morphology and expiration compliance in a rodent injury model of pulmonary edema. Automated quantification of the alveoli compliance from SD-OCT images revealed a decreased compliance in edemic lung, which also reduces the overall lung compliance when compared to the normal lung. Our method has the potential in the evaluation of alveoli compliance in a range of diseases such as edema, emphysema and pulmonary fibrosis.

We intend to extend our OCT studies and evaluate structural changes in lung tissue in hyperoxia injury rodent models *ex vivo* for real-time disease diagnosis. Hyperoxia injury has known effects on alveolar structures in lung which has not been previously measured in real time using OCT. Prolonged hyperoxia causes impaired alveolization leading to alveolar dilation as well as a decrease in the number of alveoli [304]. Alveolar dilation in hyperoxic lungs causes an increase in the alveoli diameter [304] and hence in alveolar compliance [316].

6. References

[1] Z. Ghanian, S. Maleki, S. Park, C. M. Sorenson, N. Sheibani, and M. Ranji, "Organ specific optical imaging of mitochondrial redox state in a rodent model of hereditary hemorrhagic telangiectasia-1," *J Biophotonics,* vol. 7, pp. 799-809, Oct 2014.

[2] Z. Ghanian, M. Ranji, F. Atry, S. Frye, R. Pashaie, and S. Audi, "Optical Instrumentation and the Image Cytometry of Lung and Eye Injuries: Studies in the Rodent Model," in *Biomedical Optics 2014*, Miami, Florida, 2014, p. BT3A.58.

[3] B. Alberts, *Molecular biology of the cell*, 4th ed. New York: Garland Science, 2002.

[4] *Cell Structure & Function. Available: http://people.eku.edu/ritchisong/301notes1.htm*

[5] E. N. Marieb and K. Hoehn, *Human anatomy & physiology*, 8th ed. San Francisco: Benjamin Cummings, 2010.

[6] M. W. Davidson. (2015, 2/4/2015). *Mitochondria*. Available: http://micro.magnet.fsu.edu/cells/mitochondria/mitochondria.html

[7] K. Henze and W. Martin, "Evolutionary biology: essence of mitochondria," *Nature,* vol. 426, pp. 127-8, Nov 13 2003.

[8] D. Voet, J. G. Voet, and C. W. Pratt, *Fundamentals of biochemistry : life at the molecular level*, 2nd ed. Hoboken, N.J.: Wiley, 2006.

[9] N. R. Pace, "The universal nature of biochemistry," *Proc Natl Acad Sci U S A,* vol. 98, pp. 805-8, Jan 30 2001.

[10] N. A. Campbell, B. Williamson, and R. J. Heyden, *Biology: Exploring Life*. Boston, Massachusetts: Pearson Prentice Hall, 2006.

[11] (4/2/2015). *Electron Transport Chain*. Available: http://sciencesoup.tumblr.com/post/92192632459/electron-transport-chain-from-the-mitochondrial

[12] H. Lodish, *Molecular cell biology*, 7th ed. New York, NY: W. H. Freeman and Co., 2012.

[13] T. M. Devlin, *Textbook of biochemistry : with clinical correlations*, 7th ed. Hoboken, NJ: John Wiley & Sons, 2011.

[14] N. Kango, *Textbook of Microbiology*. New Delhi: I.K. International Publishing House Pvt. Ltd., 2010.

[15] A. B. Fisher, "Intermediary metabolism of the lung," *Environ Health Perspect,* vol. 55, pp. 149-58, Apr 1984.

[16] A. Boveris and B. Chance, "The mitochondrial generation of hydrogen peroxide. General properties and effect of hyperbaric oxygen," *Biochem J,* vol. 134, pp. 707-16, Jul 1973.

[17] H. Nohl and D. Hegner, "Do mitochondria produce oxygen radicals in vivo?," *Eur J Biochem,* vol. 82, pp. 563-7, Jan 16 1978.

[18] B. Halliwell and J. M. C. Gutteridge, *Free radicals in biology and medicine,* 4th ed. Oxford ; New York: Oxford University Press, 2007.

[19] T. M. Buttke and P. A. Sandstrom, "Oxidative Stress as a Mediator of Apoptosis," *Immunology Today,* vol. 15, pp. 7-10, Jan 1994.

[20] K. Staniszewski, "OPTICAL INSTRUMENTATION AND IMAGE CYTOMETRY OF LUNG AND EYE INJURIES: STUDIES IN THE RODENT MODEL," Masters, Electrical Engineering, University of wisconsin Milwaukee, Milwaukee, 2012.

[21] M. Ranji, S. Kanemoto, M. Matsubara, M. A. Grosso, J. H. Gorman, R. C. Gorman, *et al.*, "Fluorescence spectroscopy and imaging of myocardial apoptosis," *Journal of Biomedical Optics,* vol. 11, Nov-Dec 2006.

[22] M. Ranji, M. Matsubara, B. G. Leshnower, R. H. Hinmon, D. L. Jaggard, B. Chance, *et al.*, "Quantifying acute myocardial injury using ratiometric fluorometry," *IEEE Trans Biomed Eng,* vol. 56, pp. 1556-63, May 2009.

[23] M. Matsubara, M. Ranji, B. G. Leshnower, M. Noma, S. J. Ratcliffe, B. Chance, *et al.*, "In Vivo Fluorometric Assessment of Cyclosporine on Mitochondrial Function During Myocardial Ischemia and Reperfusion," *Annals of Thoracic Surgery,* vol. 89, pp. 1532-1537, May 2010.

[24] B. Chance and H. Baltscheffsky, "Respiratory enzymes in oxidative phosphorylation. VII. Binding of intramitochondrial reduced pyridine nucleotide," *J Biol Chem,* vol. 233, pp. 736-9, Sep 1958.

[25] C. H. Barlow, W. R. Harden, 3rd, A. H. Harken, M. B. Simson, J. C. Haselgrove, B. Chance, *et al.*, "Fluorescence mapping of mitochondrial redox changes in heart and brain," *Crit Care Med,* vol. 7, pp. 402-6, Sep 1979.

[26] R. S. Balaban and L. J. Mandel, "Coupling of aerobic metabolism to active ion transport in the kidney," *J Physiol,* vol. 304, pp. 331-48, Jul 1980.

[27] E. Meirovithz, J. Sonn, and A. Mayevsky, "Effect of hyperbaric oxygenation on brain hemodynamics, hemoglobin oxygenation and mitochondrial NADH," *Brain Res Rev,* vol. 54, pp. 294-304, Jun 2007.

[28] Z. Ghanian, S. Maleki, H. Reiland, D. E. Butz, G. Chiellini, F. M. Assadi-Porter, *et al.*, "Optical imaging of mitochondrial redox state in rodent models with 3-iodothyronamine," *Exp Biol Med (Maywood),* vol. 239, pp. 151-8, Feb 2014.

[29] F. Salehpour, Z. Ghanian, C. Yang, N. N. Zheleznova, T. Kurth, R. K. Dash, *et al.*, "Effects of p67phox on the mitochondrial oxidative state in the kidney of Dahl salt-sensitive rats: optical fluorescence 3-D cryoimaging," *Am J Physiol Renal Physiol,* vol. 309, pp. F377-82, Aug 15 2015.

[30] R. Sepehr, K. Staniszewski, S. Maleki, E. R. Jacobs, S. Audi, and M. Ranji, "Optical imaging of tissue mitochondrial redox state in intact rat lungs in two models of pulmonary oxidative stress," *J Biomed Opt,* vol. 17, p. 046010, Apr 2012.

[31] Z. Ghanian, G. Konduri, and M. Ranji, "Optical Studies of Oxidative Stress in Persistent Pulmonary Hypertension Cells," in *Optics in the Life Sciences,* Vancouver, 2015, p. OW3D.6.

[32] J. R. Lakowicz, *Principles of fluorescence spectroscopy*, 3rd ed. New York: Springer, 2006.

[33] (4/25/2012). *Basic Concepts in Fluorescence*. Available: http://micro.magnet.fsu.edu/primer/techniques/fluorescence/fluorescenceintro.html

[34] J. H. Markus Sauer, Jörg Enderlein, *Handbook of Fluorescence Spectroscopy and Imaging: From Single Molecules to Ensembles*: Wiley, 2011.

[35] L. V. Wang, "Biomedical Optics: Principles and Imaging," 06/04/2007 ed. Washington University: Wiley, 2007.

[36] J. M. Christie, M. Salomon, K. Nozue, M. Wada, and W. R. Briggs, "LOV (light, oxygen, or voltage) domains of the blue-light photoreceptor phototropin (nph1): Binding sites for the chromophore flavin mononucleotide," *Proceedings of the National Academy of Sciences of the United States of America,* vol. 96, pp. 8779-8783, Jul 20 1999.

[37] G. H. Patterson, S. M. Knobel, P. Arkhammar, O. Thastrup, and D. W. Piston, "Separation of the glucose-stimulated cytoplasmic mitochondrial NAD(P)H responses in pancreatic islet beta cells," *Proceedings of the National Academy of Sciences of the United States of America,* vol. 97, pp. 5203-5207, May 9 2000.

[38] B. Chance, B. Schoener, R. Oshino, F. Itshak, and Y. Nakase, "Oxidation-reduction ratio studies of mitochondria in freeze-trapped samples. NADH and flavoprotein fluorescence signals," *J Biol Chem,* vol. 254, pp. 4764-71, Jun 10 1979.

[39] N. Ramanujam, R. Richards-Kortum, S. Thomsen, A. Mahadevan-Jansen, M. Follen, and B. Chance, "Low Temperature Fluorescence Imaging of Freeze-trapped Human Cervical Tissues," *Opt Express,* vol. 8, pp. 335-43, Mar 12 2001.

[40] M. Ranji, S. Kanemoto, M. Matsubara, M. A. Grosso, J. H. Gorman, 3rd, R. C. Gorman, *et al.*, "Fluorescence spectroscopy and imaging of myocardial apoptosis," *J Biomed Opt,* vol. 11, p. 064036, Nov-Dec 2006.

[41] K. E. Lewis, R. S. Chung, A. K. West, and M. I. Chuah, "Distribution of exogenous metallothionein following intraperitoneal and intramuscular injection of metallothionein-deficient mice," *Histol Histopathol,* vol. 27, pp. 1459-70, Nov 2012.

[42] C. H. Jiang, X. F. Wang, B. Yin, X. Y. Li, and X. M. Cui, "[Effects of exogenous nitric oxide on the subcellular distribution and chemical forms of copper in tomato seedlings under copper stress]," *Ying Yong Sheng Tai Xue Bao,* vol. 23, pp. 3033-9, Nov 2012.

[43] Z. H. Zhang, D. Blessington, H. Li, T. M. Busch, J. Glickson, Q. M. Luo, *et al.*, "Redox ratio of mitochondria as an indicator for the response of photodynamic therapy," *Journal of Biomedical Optics,* vol. 9, pp. 772-778, Jul-Aug 2004.

[44] H. N. Xu, H. Zhao, T. A. Mir, S. C. Lee, M. Feng, R. Choe, *et al.*, "Chop Therapy Induced Mitochondrial Redox State Alteration in Non-Hodgkin's Lymphoma Xenografts," *Journal of Innovative Optical Health Sciences,* vol. 6, Apr 2013.

[45] J. H. Ostrander, C. M. McMahon, S. Lem, S. R. Millon, J. Q. Brown, V. L. Seewaldt, *et al.*, "Optical Redox Ratio Differentiates Breast Cancer Cell Lines Based on Estrogen Receptor Status," *Cancer Research,* vol. 70, pp. 4759-4766, Jun 1 2010.

[46] L. Z. Li, H. N. Xu, M. Ranji, S. Nioka, and B. Chance, "Mitochondrial Redox Imaging for Cancer Diagnostic and Therapeutic Studies," *Journal of Innovative Optical Health Sciences,* vol. 2, pp. 325-341, Oct 2009.

[47] M. A. Mycek, K. T. Schomacker, and N. S. Nishioka, "Colonic polyp differentiation using time-resolved autofluorescence spectroscopy," *Gastrointestinal Endoscopy,* vol. 48, pp. 390-394, Oct 1998.

[48] M. C. Skala, K. M. Riching, D. K. Bird, A. Gendron-Fitzpatrick, J. Eickhoff, K. W. Eliceiri, *et al.*, "In vivo multiphoton fluorescence lifetime imaging of protein-bound and free nicotinamide adenine dinucleotide in normal and precancerous epithelia," *Journal of Biomedical Optics,* vol. 12, Mar-Apr 2007.

[49] A. Mayevsky and G. G. Rogatsky, "Mitochondrial function in vivo evaluated by NADH fluorescence: from animal models to human studies," *American Journal of Physiology-Cell Physiology,* vol. 292, pp. C615-C640, Feb 2007.

[50] A. Mayevsky and B. Chance, "Oxidation-reduction states of NADH in vivo: From animals to clinical use," *Mitochondrion,* vol. 7, pp. 330-339, Sep 2007.

[51] A. Mayevsky, S. Meilin, T. Manor, N. Zarchin, and J. Sonn, "Optical monitoring of NADH redox state and blood flow as indicators of brain energy balance," *Oxygen Transport to Tissue Xxi,* vol. 471, pp. 133-140, 1999.

[52] N. Ramanujam, M. F. Mitchell, A. Mahadevan, S. Thomsen, A. Malpica, T. Wright, *et al.*, "Spectroscopic diagnosis of cervical intraepithelial neoplasia (CIN) in vivo using laser-induced fluorescence spectra at multiple excitation wavelengths," *Lasers in Surgery and Medicine,* vol. 19, pp. 63-74, 1996.

[53] T. Vo-Dinh, M. Panjehpour, and B. F. Overholt, "Laser-induced fluorescence for esophageal cancer and dysplasia diagnosis," *Advances in Optical Biopsy and Optical Mammography,* vol. 838, pp. 116-122, 1998.

[54] I. Georgakoudi, B. C. Jacobson, M. G. Muller, E. E. Sheets, K. Badizadegan, D. L. Carr-Locke, *et al.*, "NAD(P)H and collagen as in vivo quantitative fluorescent biomarkers of epithelial precancerous changes," *Cancer Research,* vol. 62, pp. 682-687, Feb 1 2002.

[55] Z. Ghanian, K. Staniszewski, N. Jamali, R. Sepehr, S. Wang, C. M. Sorenson, *et al.*, "Quantitative Assessment of Retinopathy Using Multi-parameter Image Analysis," *J Med Signals Sens,* vol. 6, pp. 71-80, Apr-Jun 2016.

[56] R. A. Kowluru and P. S. Chan, "Oxidative stress and diabetic retinopathy," *Exp Diabetes Res,* vol. 2007, p. 43603, 2007.

[57] M. Al-Shabrawey, M. Bartoli, A. B. El-Remessy, D. H. Platt, S. Matragoon, M. A. Behzadian, *et al.*, "Inhibition of NAD(P)H oxidase activity blocks vascular endothelial growth factor overexpression and neovascularization during ischemic retinopathy," *Am J Pathol,* vol. 167, pp. 599-607, Aug 2005.

[58] D. S. Fong, L. Aiello, T. W. Gardner, G. L. King, G. Blankenship, J. D. Cavallerano, *et al.*, "Diabetic retinopathy," *Diabetes Care,* vol. 26, pp. 226-9, Jan 2003.

[59] "Retinopathy and nephropathy in patients with type 1 diabetes four years after a trial of intensive therapy. The Diabetes Control and Complications Trial/Epidemiology of Diabetes Interventions and Complications Research Group," *N Engl J Med,* vol. 342, pp. 381-9, Feb 10 2000.

[60] L. P. Aiello, T. W. Gardner, G. L. King, G. Blankenship, J. D. Cavallerano, F. L. Ferris, *et al.*, "Diabetic retinopathy," *Diabetes Care,* vol. 21, pp. 157-159, Jan 1998.

[61] R. N. Frank, "Diabetic retinopathy," *N Engl J Med,* vol. 350, pp. 48-58, Jan 1 2004.

[62] H. P. Hammes, Y. Feng, F. Pfister, and M. Brownlee, "Diabetic retinopathy: targeting vasoregression," *Diabetes,* vol. 60, pp. 9-16, Jan 2011.

[63] R. Klein, B. E. Klein, S. E. Moss, M. D. Davis, and D. L. DeMets, "The Wisconsin epidemiologic study of diabetic retinopathy. II. Prevalence and risk of diabetic retinopathy when age at diagnosis is less than 30 years," *Arch Ophthalmol,* vol. 102, pp. 520-6, Apr 1984.

[64] T. S. Kern, Y. P. Du, C. M. Miller, D. A. Hatala, and L. A. Levin, "Overexpression of Bcl-2 in Vascular Endothelium Inhibits the Microvascular Lesions of Diabetic Retinopathy," *American Journal of Pathology,* vol. 176, pp. 2550-2558, May 2010.

[65] T. Khalfaoui, N. Basora, and A. Ouertani-Meddeb, "Apoptotic factors (Bcl-2 and Bax) and diabetic retinopathy in type 2 diabetes," *Journal of Molecular Histology,* vol. 41, pp. 143-152, Apr 2010.

[66] W. L. Li and D. Y. Jiang, "Effect of Resveratrol on Bcl-2 and VEGF Expression in Oxygen-Induced Retinopathy of Prematurity," *Journal of Pediatric Ophthalmology & Strabismus,* vol. 49, pp. 230-235, Jul-Aug 2012.

[67] M. Mizutani and M. Lorenzi, "Increased expression of Bcl-2 in Muller glial cells in human diabetic retinopathy.," *Diabetes,* vol. 46, pp. 502-502, May 1997.

[68] N. Sheibani and C. M. Sorenson, "Bcl-2 is essential for development of the retinal vasculature and retinal neovascularization during oxygen-induced ischemic retinopathy," *Investigative Ophthalmology & Visual Science,* vol. 45, pp. U733-U733, Apr 2004.

[69] H. Y. Wang and X. L. Chen, "Effects of a Rho kinase inhibitor on the sequential expression of ICAM-1, HIF-1 alpha, Bcl-2 and caspase-3 in the retina of rats with oxygen-induced retinopathy," *International Journal of Molecular Medicine,* vol. 32, pp. 457-463, Aug 2013.

[70] S. J. Wang, C. M. Sorenson, and N. Sheibani, "Attenuation of retinal vascular development and neovascularization during oxygen-induced ischemic retinopathy in Bcl-2-/- mice," *Developmental Biology,* vol. 279, pp. 205-219, Mar 1 2005.

[71] A. K. Zimmermann, F. A. Loucks, E. K. Schroeder, R. J. Bouchard, K. L. Tyler, and D. A. Linseman, "Glutathione binding to the Bcl-2 homology-3 domain groove - A molecular basis for Bcl-2 antioxidant function at mitochondria," *Journal of Biological Chemistry,* vol. 282, pp. 29296-29304, Oct 5 2007.

[72] I. Giardino, D. Edelstein, and M. Brownlee, "BCL-2 expression or antioxidants prevent hyperglycemia-induced formation of intracellular advanced glycation endproducts in bovine endothelial cells," *Journal of Clinical Investigation,* vol. 97, pp. 1422-1428, Mar 15 1996.

[73] N. Susnow, L. Y. Zeng, D. Margineantu, and D. M. Hockenbery, "Bcl-2 family proteins as regulators of oxidative stress," *Seminars in Cancer Biology,* vol. 19, pp. 42-49, Feb 2009.

[74] Z. C. Han, J. J. Guo, S. M. Conley, and M. I. Naash, "Retinal Angiogenesis in the Ins2(Akita) Mouse Model of Diabetic Retinopathy," *Investigative Ophthalmology & Visual Science,* vol. 54, pp. 574-584, Jan 2013.

[75] A. J. Barber, D. A. Antonetti, C. E. N. Reiter, C. A. Stiller, T. W. Gardner, and S. K. Bronson, "The Ins2(Akita) mouse as a model of diabetic retinopathy," *Investigative Ophthalmology & Visual Science,* vol. 45, pp. U92-U92, Apr 2004.

[76] N. N. Vagaja, N. Binz, S. McLenachan, E. P. Rakoczy, and P. G. McMenamin, "Influence of endotoxin-mediated retinal inflammation on phenotype of diabetic retinopathy in Ins2(Akita) mice," *British Journal of Ophthalmology,* vol. 97, pp. 1343-1350, Oct 2013.

[77] K. A. McAllister, K. M. Grogg, D. W. Johnson, C. J. Gallione, M. A. Baldwin, C. E. Jackson, *et al.*, "Endoglin, a TGF-beta binding protein of endothelial cells, is the gene for hereditary haemorrhagic telangiectasia type 1," *Nat Genet,* vol. 8, pp. 345-51, Dec 1994.

[78] S. A. Abdalla and M. Letarte, "Hereditary haemorrhagic telangiectasia: current views on genetics and mechanisms of disease," *J Med Genet,* vol. 43, pp. 97-110, Feb 2006.

[79] D. W. Johnson, J. N. Berg, M. A. Baldwin, C. J. Gallione, I. Marondel, S. J. Yoon, *et al.*, "Mutations in the activin receptor-like kinase 1 gene in hereditary haemorrhagic telangiectasia type 2," *Nat Genet,* vol. 13, pp. 189-95, Jun 1996.

[80] L. A. Fernandez, F. Sanz-Rodriguez, F. J. Blanco, C. Bernabeu, and L. M. Botella, "Hereditary hemorrhagic telangiectasia, a vascular dysplasia affecting the TGF-beta signaling pathway," *Clin Med Res,* vol. 4, pp. 66-78, Mar 2006.

[81] J. McDonald and P. Bayrak-Toydemir, "Hereditary hemorrhagic telangiectasia," *Haematologica,* vol. 90, pp. 728-32, Jun 2005.

[82] J. McDonald, P. Bayrak-Toydemir, and R. E. Pyeritz, "Hereditary hemorrhagic telangiectasia: an overview of diagnosis, management, and pathogenesis," *Genet Med,* vol. 13, pp. 607-16, Jul 2011.

[83] J. McDonald and R. E. Pyeritz, "Hereditary Hemorrhagic Telangiectasia," 1993.

[84] L. Jonker and H. M. Arthur, "Endoglin expression in early development is associated with vasculogenesis and angiogenesis," *Mechanisms of Development,* vol. 110, pp. 193-196, Jan 2002.

[85] T. Seki, J. Yun, and S. P. Oh, "Arterial endothelium-specific activin receptor-like kinase 1 expression suggests its role in arterialization and vascular remodeling," *Circ Res,* vol. 93, pp. 682-9, Oct 3 2003.

[86] C. L. Shovlin, "Hereditary haemorrhagic telangiectasia: pathophysiology, diagnosis and treatment," *Blood Rev,* vol. 24, pp. 203-19, Nov 2010.

[87] A. M. Brant, A. P. Schachat, and R. I. White, "Ocular manifestations in hereditary hemorrhagic telangiectasia (Rendu-Osler-Weber disease)," *Am J Ophthalmol,* vol. 107, pp. 642-6, Jun 15 1989.

[88] D. G. Davis and J. L. Smith, "Retinal involvement in hereditary hemorrhagic telangiectasia," *Arch Ophthalmol,* vol. 85, pp. 618-21 passim, May 1971.

[89] E. L. Forker and W. B. Bean, "Retinal arteriovenous aneurysm in hereditary hemorrhagic telangiectasia," *Arch Intern Med,* vol. 111, pp. 778-83, Jun 1963.

[90] A. Giovannini, B. Scassellati-Sforzolini, E. D'Altobrando, C. Mariotti, T. Rutili, and R. Tittarelli, "Choroidal findings in the course of idiopathic serous pigment epithelium

detachment detected by indocyanine green videoangiography," *Retina,* vol. 17, pp. 286-93, 1997.

[91] D. C. Tsai, A. G. Wang, A. F. Lee, W. M. Hsu, J. H. Liu, and M. Y. Yen, "Choroidal telangiectasia in a patient with hereditary hemorrhagic telangiectasia," *Eye (Lond),* vol. 16, pp. 92-4, Jan 2002.

[92] M. Ziani, C. Valignat, J. G. Lopez, A. Ruffion, H. Plauchu, and P. Perrin, "Renal arteriovenous malformation requiring surgery in Rendu-Osler-Weber disease (hereditary hemorrhagic telangiectasia)," *J Urol,* vol. 164, pp. 1292-3, Oct 2000.

[93] G. D. Babushkina, M. I. Davidov, and T. V. Kir'ianova, "[Profuse intravesical hemorrhage caused by Rendu-Osler-Weber disease]," *Klin Med (Mosk),* vol. 79, pp. 67-8, 2001.

[94] L. E. Smith, E. Wesolowski, A. McLellan, S. K. Kostyk, R. D'Amato, R. Sullivan, *et al.*, "Oxygen-induced retinopathy in the mouse," *Invest Ophthalmol Vis Sci,* vol. 35, pp. 101-11, Jan 1994.

[95] S. Park, T. A. Dimaio, W. Liu, S. Wang, C. M. Sorenson, and N. Sheibani, "Endoglin Regulates the Activation and Quiescence of Endothelium by Participating in Canonical and Non-Canonical TGF-beta Signaling Pathways," *J Cell Sci,* Feb 15 2013.

[96] R. A. Kowluru, J. Tang, and T. S. Kern, "Abnormalities of retinal metabolism in diabetes and experimental galactosemia. VII. Effect of long-term administration of antioxidants on the development of retinopathy," *Diabetes,* vol. 50, pp. 1938-42, Aug 2001.

[97] M. Kanwar, P. S. Chan, T. S. Kern, and R. A. Kowluru, "Oxidative damage in the retinal mitochondria of diabetic mice: possible protection by superoxide dismutase," *Invest Ophthalmol Vis Sci,* vol. 48, pp. 3805-11, Aug 2007.

[98] Y. Tang, E. A. Scheef, S. Wang, C. M. Sorenson, C. B. Marcus, C. R. Jefcoate, *et al.*, "CYP1B1 expression promotes the proangiogenic phenotype of endothelium through decreased intracellular oxidative stress and thrombospondin-2 expression," *Blood,* vol. 113, pp. 744-54, Jan 15 2009.

[99] D. Besch, H. Jagle, H. P. Scholl, M. W. Seeliger, and E. Zrenner, "Inherited multifocal RPE-diseases: mechanisms for local dysfunction in global retinoid cycle gene defects," *Vision Res,* vol. 43, pp. 3095-108, Dec 2003.

[100] J. Sancho-Pelluz, B. Arango-Gonzalez, S. Kustermann, F. J. Romero, T. van Veen, E. Zrenner, *et al.*, "Photoreceptor cell death mechanisms in inherited retinal degeneration," *Mol Neurobiol,* vol. 38, pp. 253-69, Dec 2008.

[101] D. T. Hartong, E. L. Berson, and T. P. Dryja, "Retinitis pigmentosa," *Lancet,* vol. 368, pp. 1795-809, Nov 18 2006.

[102] N. Sanvicens, V. Gomez-Vicente, I. Masip, A. Messeguer, and T. G. Cotter, "Oxidative stress-induced apoptosis in retinal photoreceptor cells is mediated by calpains and caspases and blocked by the oxygen radical scavenger CR-6," *J Biol Chem,* vol. 279, pp. 39268-78, Sep 17 2004.

[103] M. M. Sanz, L. E. Johnson, S. Ahuja, P. A. Ekstrom, J. Romero, and T. van Veen, "Significant photoreceptor rescue by treatment with a combination of antioxidants in an animal model for retinal degeneration," *Neuroscience,* vol. 145, pp. 1120-9, Mar 30 2007.

[104] M. Donovan, R. J. Carmody, and T. G. Cotter, "Light-induced photoreceptor apoptosis in vivo requires neuronal nitric-oxide synthase and guanylate cyclase activity and is caspase-3-independent," *J Biol Chem,* vol. 276, pp. 23000-8, Jun 22 2001.

[105] H. Yamada, E. Yamada, A. Ando, N. Esumi, N. Bora, J. Saikia, *et al.,* "Fibroblast growth factor-2 decreases hyperoxia-induced photoreceptor cell death in mice," *Am J Pathol,* vol. 159, pp. 1113-20, Sep 2001.

[106] F. Q. Schafer and G. R. Buettner, "Redox environment of the cell as viewed through the redox state of the glutathione disulfide/glutathione couple," *Free Radical Biology and Medicine,* vol. 30, pp. 1191-1212, Jun 1 2001.

[107] K. Nagata, Y. Iwasaki, T. Yamada, T. Yuba, K. Kono, S. Hosogi, *et al.,* "Overexpression of manganese superoxide dismutase by N-acetylcysteine in hyperoxic lung injury," *Respiratory Medicine,* vol. 101, pp. 800-807, Apr 2007.

[108] E. Gitto, R. J. Reiter, M. Karbownik, X. T. Dun, and I. Barberi, "Respiratory distress syndrome in the newborn: role of oxidative stress," *Intensive Care Medicine,* vol. 27, pp. 1116-1123, Jul 2001.

[109] M. E. Wearden, U. T. Brunk, A. Terman, and J. W. Eaton, "Mitochondria: Potential importance in hyperoxic lung injury," *Pediatric Research,* vol. 47, pp. 380a-380a, Apr 2000.

[110] O. D. Saugstad, "Bronchopulmonary dysplasia-oxidative stress and antioxidants," *Semin Neonatol,* vol. 8, pp. 39-49, Feb 2003.

[111] V. Sampath, A. C. Radish, A. L. Eis, K. Broniowska, N. Hogg, and G. G. Konduri, "Attenuation of lipopolysaccharide-induced oxidative stress and apoptosis in fetal pulmonary artery endothelial cells by hypoxia," *Free Radic Biol Med,* vol. 46, pp. 663-71, Mar 1 2009.

[112] K. N. Farrow, S. Wedgwood, K. J. Lee, L. Czech, S. F. Gugino, S. Lakshminrusimha, *et al.,* "Mitochondrial oxidant stress increases PDE5 activity in persistent pulmonary hypertension of the newborn," *Respiratory Physiology & Neurobiology,* vol. 174, pp. 272-281, Dec 31 2010.

[113] S. Lakshminrusimha, J. A. Russell, R. H. Steinhorn, D. D. Swartz, R. M. Ryan, S. F. Gugino, *et al.*, "Pulmonary Hemodynamics in neonatal lambs resuscitated with 21%, 50%, and 100% oxygen," *Pediatric Research,* vol. 62, pp. 313-318, Sep 2007.

[114] R. J. Teng, A. Eis, I. Bakhutashvili, N. Arul, and G. G. Konduri, "Increased superoxide production contributes to the impaired angiogenesis of fetal pulmonary arteries with in utero pulmonary hypertension," *American Journal of Physiology-Lung Cellular and Molecular Physiology,* vol. 297, pp. L184-L195, Jul 2009.

[115] A. J. Afolayan, A. Eis, M. Alexander, T. Michalkiewicz, R. J. Teng, S. Lakshminrusimha, *et al.*, "Decreased endothelial nitric oxide synthase expression and function contribute to impaired mitochondrial biogenesis and oxidative stress in fetal lambs with persistent pulmonary hypertension," *American Journal of Physiology-Lung Cellular and Molecular Physiology,* vol. 310, pp. L40-L49, Jan 1 2016.

[116] A. J. Afolayan, A. Eis, R. J. Teng, I. Bakhutashvili, S. Kaul, J. M. Davis, *et al.*, "Decreases in manganese superoxide dismutase expression and activity contribute to oxidative stress in persistent pulmonary hypertension of the newborn," *American Journal of Physiology-Lung Cellular and Molecular Physiology,* vol. 303, pp. L870-L879, Nov 2012.

[117] R. J. Teng, J. H. Du, S. Welak, T. J. Guan, A. Eis, Y. Shi, *et al.*, "Cross talk between NADPH oxidase and autophagy in pulmonary artery endothelial cells with intrauterine persistent pulmonary hypertension," *American Journal of Physiology-Lung Cellular and Molecular Physiology,* vol. 302, pp. 1651-1663, Apr 2012.

[118] G. G. Konduri, I. Bakhutashvili, A. Eis, and K. Pritchard, "Oxidant stress from uncoupled nitric oxide synthase impairs vasodilation in fetal lambs with persistent pulmonary hypertension," *American Journal of Physiology-Heart and Circulatory Physiology,* vol. 292, pp. H1812-H1820, Apr 2007.

[119] G. G. Konduri, J. S. Ou, Y. Shi, and K. A. Pritchard, "Decreased association of HSP90 impairs endothelial nitric oxide synthase in fetal lambs with persistent pulmonary hypertension," *American Journal of Physiology-Heart and Circulatory Physiology,* vol. 285, pp. H204-H211, Jul 2003.

[120] G. G. Konduri, J. S. Ou, S. Yang, and K. A. Pritchard, "Decreased association of heat shock protein 90 (hsp90) impairs endothelial nitric oxide synthase (eNOS) in fetal lambs with persistent pulmonary hypertension of newborn (PPHN)," *Pediatric Research,* vol. 53, pp. 352a-352a, Apr 2003.

[121] M. E. T. Villanueva, F. M. Zaher, D. M. Svinarich, and G. G. Konduri, "Decreased gene expression of endothelial nitric oxide synthase in newborns with persistent pulmonary hypertension," *Pediatric Research,* vol. 44, pp. 338-343, Sep 1998.

[122] M. E. T. Villanueva, F. M. Zaher, D. M. Svinarich, and G. G. Konduri, "Decreased expression of endothelial nitric oxide synthase in newborns with persistent pulmonary hypertension," *Pediatrics,* vol. 100, pp. 500-500, Sep 1997.

[123] A. B. Fisher, L. Furia, and B. Chance, "Evaluation of redox state of isolated perfused rat lung," *Am J Physiol,* vol. 230, pp. 1198-1204, May 1976.

[124] J. D. Crapo, B. E. Barry, H. A. Foscue, and J. Shelburne, "Structural and biochemical changes in rat lungs occurring during exposures to lethal and adaptive doses of oxygen," *Am Rev Respir Dis,* vol. 122, pp. 123-43, Jul 1980.

[125] W. A. Altemeier and S. E. Sinclair, "Hyperoxia in the intensive care unit: why more is not always better," *Curr Opin Crit Care,* vol. 13, pp. 73-8, Feb 2007.

[126] A. B. Fisher and M. F. Beers, "Hyperoxia and acute lung injury," *Am J Physiol Lung Cell Mol Physiol,* vol. 295, p. L1066; author reply L1067, Dec 2008.

[127] C. S. Ng, S. Wan, and A. P. Yim, "Pulmonary ischaemia-reperfusion injury: role of apoptosis," *Eur Respir J,* vol. 25, pp. 356-63, Feb 2005.

[128] http://www.infoplease.com/science/health/us-transplants-year

[129] A. Piechota and A. Goraca, "INFLUENCE OF NUCLEAR FACTOR-kappa B INHIBITION ON ENDOTHELIN-1 INDUCED LUNG EDEMA AND OXIDATIVE STRESS IN RATS," *Journal of Physiology and Pharmacology,* vol. 62, pp. 183-188, Apr 2011.

[130] C. Chupin, A. Prive, E. Brochiero, and Y. Berthiaume, "Impact of oxidative stress on epithelial repair and alveolar oedema, within in vitro model of lung injury," *Faseb Journal,* vol. 22, Apr 2008.

[131] S. Khademi, K. Jeckel, M. A. Frye, D. Irwin, T. Schroeder, B. F. Miller, *et al.*, "Oxidative stress and induction of non-cardiogenic pulmonary edema following cerebral hypoxia in a canine model," *Faseb Journal,* vol. 27, Apr 2013.

[132] A. Mishra, Z. Ali, A. Vibhuti, R. Kumar, P. Alam, R. Ram, *et al.*, "CYBA and GSTP 1 variants associate with oxidative stress under hypobaric hypoxia as observed in high-altitude pulmonary oedema," *Clinical Science,* vol. 122, pp. 299-309, Mar 2012.

[133] S. Gumus, O. Yucel, M. Gamsizkan, A. Eken, O. Deniz, E. Tozkoparan, *et al.*, "The role of oxidative stress and effect of alpha-lipoic acid in reexpansion pulmonary edema - an experimental study," *Archives of Medical Science,* vol. 6, pp. 848-853, Dec 2010.

[134] K. Kim, Y. Lee, D. Hyun, S. Lee, and S. Park, "Rutin Ameliorates Neutrophilic Oxidative Stress-Induced Acute Pulmonary Edema in Rats Given IL-1 Intratracheally.," *American Journal of Respiratory and Critical Care Medicine,* vol. 179, 2009.

[135] S. Sarada, P. Himadri, C. Mishra, P. Geetali, M. S. Ram, and G. Ilavazhagan, "Role of oxidative stress and NFkB in hypoxia-induced pulmonary edema," *Experimental Biology and Medicine,* vol. 233, pp. 1088-1098, Sep 2008.

[136] T. Stuber, S. Thalmann, P. Y. Jayet, M. Villena, D. Hutter, C. Sartori, *et al.*, "Oxidative stress mediated chronic pulmonary hypertension in re-entry pulmonary oedema-prone high-altitude dwellers," *European Heart Journal*, vol. 26, pp. 81-81, Sep 2005.

[137] S. Thalmann, Y. Allemann, P. Y. Jayet, D. Hutter, C. Salinas, T. Stuber, *et al.*, "Oxidative stress mediated chronic pulmonary hypertension in re-entry pulmonary edema-prone high-altitude dwellers," *Faseb Journal*, vol. 19, pp. A1333-A1333, Mar 7 2005.

[138] I. S. Anand, B. A. K. Prasad, S. S. Chugh, K. R. M. Rao, D. N. Cornfield, C. E. Milla, *et al.*, "Effects of inhaled nitric oxide and oxygen in high-altitude pulmonary edema," *Circulation*, vol. 98, pp. 2441-2445, Dec 1 1998.

[139] P. Bartsch, M. Maggiorini, M. Ritter, C. Noti, P. Vock, and O. Oelz, "Prevention of High-Altitude Pulmonary-Edema by Nifedipine," *New England Journal of Medicine*, vol. 325, pp. 1284-1289, Oct 31 1991.

[140] B. Vollmar, M. Burkhardt, T. Minor, H. Klauke, and M. D. Menger, "A correlation of intravital microscopically assessed NADH fluorescence, tissue oxygenation, and organ function during shock and resuscitation of the rat liver," *Oxygen Transport to Tissue Xx*, vol. 454, pp. 95-101, 1998.

[141] S. Nioka, D. J. Wang, J. Im, T. Hamaoka, Z. Y. J. Wang, J. S. Leigh, *et al.*, "Simulation of Mb/Hb in NIRS and oxygen gradient in the human and canine skeletal muscles using H-NMR and NIRS," *Oxygen Transport to Tissue Xxvii*, vol. 578, pp. 223-228, 2006.

[142] N. Ramanujam, M. F. Mitchell, A. Mahadevan, S. Warren, S. Thomsen, E. Silva, *et al.*, "In-Vivo Diagnosis of Cervical Intraepithelial Neoplasia Using 337-Nm-Excited Laser-Induced Fluorescence," *Proceedings of the National Academy of Sciences of the United States of America*, vol. 91, pp. 10193-10197, Oct 11 1994.

[143] A. Shiino, M. Haida, B. Beauvoit, and B. Chance, "Three-dimensional redox image of the normal gerbil brain," *Neuroscience*, vol. 91, pp. 1581-5, 1999.

[144] B. Quistorff, J. C. Haselgrove, and B. Chance, "High spatial resolution readout of 3-D metabolic organ structure: an automated, low-temperature redox ratio-scanning instrument," *Anal Biochem*, vol. 148, pp. 389-400, Aug 1 1985.

[145] C. M. Sorenson, S. Wang, R. Gendron, H. Paradis, and N. Sheibani, "Thrombospondin-1 Deficiency Exacerbates the Pathogenesis of Diabetic Retinopathy," *J Diabetes Metab*, vol. Suppl 12, May 25 2013.

[146] D. Y. Li, L. K. Sorensen, B. S. Brooke, L. D. Urness, E. C. Davis, D. G. Taylor, *et al.*, "Defective angiogenesis in mice lacking endoglin," *Science*, vol. 284, pp. 1534-7, May 28 1999.

[147] Z. Wu, S. Wang, C. M. Sorenson, and N. Sheibani, "Attenuation of retinal vascular development and neovascularization in transgenic mice over-expressing thrombospondin-1 in the lens," *Dev Dyn,* vol. 235, pp. 1908-20, Jul 2006.

[148] S. Maleki, S. Gopalakrishnan, Z. Ghanian, R. Sepehr, H. Schmitt, J. Eells, *et al.*, "Optical imaging of mitochondrial redox state in rodent model of retinitis pigmentosa," *J Biomed Opt,* vol. 18, p. 16004, Jan 2013.

[149] B. Chance, B. Schoener, R. Oshino, F. Itshak, and Y. Nakase, "Oxidation-reduction ratio studies of mitochondria in freeze-trapped samples. NADH and flavoprotein fluorescence signals," *Journal of Biological Chemistry,* vol. 254, pp. 4764-71, Jun 10 1979.

[150] J. J. Kelly, J. R. Ewen, S. L. Bernard, R. W. Glenny, and C. H. Barlow, "Regional blood flow measurements from fluorescent microsphere images using an Imaging CryoMicrotome," *Review of Scientific Instruments,* vol. 71, pp. 228-234, Jan 2000.

[151] S. L. Bernard, J. R. Ewen, C. H. Barlow, J. J. Kelly, S. McKinney, D. A. Frazer, *et al.*, "High spatial resolution measurements of organ blood flow in small laboratory animals," *Am J Physiol Heart Circ Physiol,* vol. 279, pp. H2043-52, Nov 2000.

[152] B. Chance and H. Baltscheffsky, "Respiratory enzymes in oxidative phosphorylation. VII. Binding of intramitochondrial reduced pyridine nucleotide," *Journal of Biological Chemistry,* vol. 233, pp. 736-9, Sep 1958.

[153] B. Chance, C. P. Lee, and B. Schoener, "High and low energy states of cytochromes. II. In submitochondrial particles," *Journal of Biological Chemistry,* vol. 241, pp. 4574-6, Oct 25 1966.

[154] G. H. Travis, "Mechanisms of cell death in the inherited retinal degenerations," *Am J Hum Genet,* vol. 62, pp. 503-8, Mar 1998.

[155] M. A. Penna and K. A. Dines, "A simple method for fitting sphere-like surfaces," *Ieee Transactions on Pattern Analysis and Machine Intelligence,* vol. 29, pp. 1673-1678, Sep 2007.

[156] W. T. Ham, Jr., H. A. Mueller, and D. H. Sliney, "Retinal sensitivity to damage from short wavelength light," *Nature,* vol. 260, pp. 153-5, Mar 11 1976.

[157] W. T. Ham, Jr., H. A. Mueller, J. J. Ruffolo, Jr., D. Guerry, 3rd, and R. K. Guerry, "Action spectrum for retinal injury from near-ultraviolet radiation in the aphakic monkey," *Am J Ophthalmol,* vol. 93, pp. 299-306, Mar 1982.

[158] M. Bando, M. Oka, K. Kawai, H. Obazawa, and M. Takehana, "NADH photo-oxidation is enhanced by a partially purified lambda-crystallin fraction from rabbit lens," *Molecular Vision,* vol. 13, pp. 1722-1729, Sep 18 2007.

[159] A. Polito, S. M. Shah, J. A. Haller, I. Zimmer-Galler, R. Zeimer, P. A. Campochiaro, *et al.*, "Comparison between retinal thickness analyzer and optical coherence tomography

for assessment of foveal thickness in eyes with macular disease," *Am J Ophthalmol,* vol. 134, pp. 240-51, Aug 2002.

[160] F. Mac Gabhann, A. M. Demetriades, T. Deering, J. D. Packer, S. M. Shah, E. Duh, *et al.*, "Protein transport to choroid and retina following periocular injection: theoretical and experimental study," *Ann Biomed Eng,* vol. 35, pp. 615-30, Apr 2007.

[161] J. L. Dunaief, T. Dentchev, G. S. Ying, and A. H. Milam, "The role of apoptosis in age-related macular degeneration," *Arch Ophthalmol,* vol. 120, pp. 1435-42, Nov 2002.

[162] F. Podesta, G. Romeo, W. H. Liu, S. Krajewski, J. C. Reed, C. Gerhardinger, *et al.*, "Bax is increased in the retina of diabetic subjects and is associated with pericyte apoptosis in vivo and in vitro," *Am J Pathol,* vol. 156, pp. 1025-32, Mar 2000.

[163] L. A. Kerrigan, D. J. Zack, H. A. Quigley, S. D. Smith, and M. E. Pease, "TUNEL-positive ganglion cells in human primary open-angle glaucoma," *Arch Ophthalmol,* vol. 115, pp. 1031-5, Aug 1997.

[164] Y. Du, C. M. Miller, and T. S. Kern, "Hyperglycemia increases mitochondrial superoxide in retina and retinal cells," *Free Radic Biol Med,* vol. 35, pp. 1491-9, Dec 1 2003.

[165] N. G. Docherty, J. M. Lopez-Novoa, M. Arevalo, A. Duwel, A. Rodriguez-Pena, F. Perez-Barriocanal, *et al.*, "Endoglin regulates renal ischaemia-reperfusion injury," *Nephrol Dial Transplant,* vol. 21, pp. 2106-19, Aug 2006.

[166] M. Jerkic, M. G. Kabir, A. Davies, L. X. Yu, B. A. McIntyre, N. W. Husain, *et al.*, "Pulmonary hypertension in adult Alk1 heterozygous mice due to oxidative stress," *Cardiovasc Res,* vol. 92, pp. 375-84, Dec 1 2011.

[167] M. Toporsian, M. Jerkic, Y. Q. Zhou, M. G. Kabir, L. X. Yu, B. A. McIntyre, *et al.*, "Spontaneous adult-onset pulmonary arterial hypertension attributable to increased endothelial oxidative stress in a murine model of hereditary hemorrhagic telangiectasia," *Arterioscler Thromb Vasc Biol,* vol. 30, pp. 509-17, Mar 2010.

[168] F. Seta, M. Rahmani, P. V. Turner, and C. D. Funk, "Pulmonary oxidative stress is increased in cyclooxygenase-2 knockdown mice with mild pulmonary hypertension induced by monocrotaline," *PLoS One,* vol. 6, p. e23439, 2011.

[169] S. Usui, K. Komeima, S. Y. Lee, Y. J. Jo, S. Ueno, B. S. Rogers, *et al.*, "Increased expression of catalase and superoxide dismutase 2 reduces cone cell death in retinitis pigmentosa," *Mol Ther,* vol. 17, pp. 778-86, May 2009.

[170] J. Shen, X. Yang, A. Dong, R. M. Petters, Y. W. Peng, F. Wong, *et al.*, "Oxidative damage is a potential cause of cone cell death in retinitis pigmentosa," *J Cell Physiol,* vol. 203, pp. 457-64, Jun 2005.

[171] D. Y. Yu and S. J. Cringle, "Oxygen distribution and consumption within the retina in vascularised and avascular retinas and in animal models of retinal disease," *Prog Retin Eye Res,* vol. 20, pp. 175-208, Mar 2001.

[172] J. A. Dykens, A. K. Carroll, S. Wiley, D. F. Covey, Z. Y. Cai, L. Zhao, *et al.*, "Photoreceptor preservation in the S334ter model of retinitis pigmentosa by a novel estradiol analog," *Biochem Pharmacol,* vol. 68, pp. 1971-84, Nov 15 2004.

[173] D. S. Cassarino, R. H. Swerdlow, J. K. Parks, W. D. Parker, Jr., and J. P. Bennett, Jr., "Cyclosporin A increases resting mitochondrial membrane potential in SY5Y cells and reverses the depressed mitochondrial membrane potential of Alzheimer's disease cybrids," *Biochem Biophys Res Commun,* vol. 248, pp. 168-73, Jul 9 1998.

[174] M. J. Phillips, T. A. Walker, H. Y. Choi, A. E. Faulkner, M. K. Kim, S. S. Sidney, *et al.*, "Tauroursodeoxycholic acid preservation of photoreceptor structure and function in the rd10 mouse through postnatal day 30," *Invest Ophthalmol Vis Sci,* vol. 49, pp. 2148-55, May 2008.

[175] L. Yang, J. H. Kim, K. D. Kovacs, J. G. Arroyo, and D. F. Chen, "Minocycline inhibition of photoreceptor degeneration," *Arch Ophthalmol,* vol. 127, pp. 1475-80, Nov 2009.

[176] I. Georgakoudi, B. C. Jacobson, M. G. Muller, E. E. Sheets, K. Badizadegan, D. L. Carr-Locke, *et al.*, "NAD(P)H and collagen as in vivo quantitative fluorescent biomarkers of epithelial precancerous changes," *Cancer Res,* vol. 62, pp. 682-7, Feb 1 2002.

[177] G. A. Wagnieres, W. M. Star, and B. C. Wilson, "In vivo fluorescence spectroscopy and imaging for oncological applications," *Photochem Photobiol,* vol. 68, pp. 603-32, Nov 1998.

[178] L. R. Joseph, "*Principles of Fluorescence Spectroscopy*," *Springer,* 2006.

[179] T. Kim, S. J. Kim, K. Kim, U. B. Kang, C. Lee, K. S. Park, *et al.*, "Profiling of vitreous proteomes from proliferative diabetic retinopathy and nondiabetic patients," *Proteomics,* vol. 7, pp. 4203-15, Nov 2007.

[180] B. Chance, P. Cohen, F. Jobsis, and B. Schoener, "Intracellular oxidation-reduction states in vivo," *Science,* vol. 137, pp. 499-508, Aug 17 1962.

[181] Y. Avi-Dor, J. Olson, M. Doherty, and N. Kaplan, "Fluorescence of pyridine nucleotides in mitochondria," *Biol. Chem,* vol. 237, p. 7, 1962.

[182] L. K. Klaidman, A. C. Leung, and J. D. Adams, Jr., "High-performance liquid chromatography analysis of oxidized and reduced pyridine dinucleotides in specific brain regions," *Anal Biochem,* vol. 228, pp. 312-7, Jul 1 1995.

[183] M. O'Connor, F. Welsh, L. Komarnicky, L. Davis, J. Stevens, D. Lewis, *et al.*, "Origin of labile NADH tissue fluorescence," *Oxygen Physiol. Function,* p. 10, 1977.

[184] T. Y. Wong and P. Mitchell, "Hypertensive retinopathy," *N Engl J Med,* vol. 351, pp. 2310-7, Nov 25 2004.

[185] N. M. Bressler, S. B. Bressler, and S. L. Fine, "Age-related macular degeneration," *Survey of Ophthalmology,* vol. 32, pp. 375-413, May-Jun 1988.

[186] L. A. Wittenberg, N. J. Jonsson, R. V. Chan, and M. F. Chiang, "Computer-based image analysis for plus disease diagnosis in retinopathy of prematurity," *J Pediatr Ophthalmol Strabismus,* vol. 49, pp. 11-9; quiz 10, 20, Jan-Feb 2012.

[187] M. K. Ikram, C. Y. Cheung, M. Lorenzi, R. Klein, T. L. Z. Jones, T. Y. Wong, *et al.*, "Retinal Vascular Caliber as a Biomarker for Diabetes Microvascular Complications," *Diabetes Care,* vol. 36, pp. 750-759, Mar 2013.

[188] G. N. Thomas, S. Y. Ong, Y. C. Tham, W. Hsu, M. L. Lee, Q. P. Lau, *et al.*, "Measurement of macular fractal dimension using a computer-assisted program," *Invest Ophthalmol Vis Sci,* vol. 55, pp. 2237-43, Apr 2014.

[189] M. D. Abramoff, J. C. Folk, D. P. Han, J. D. Walker, D. F. Williams, S. R. Russell, *et al.*, "Automated analysis of retinal images for detection of referable diabetic retinopathy," *JAMA Ophthalmol,* vol. 131, pp. 351-7, Mar 2013.

[190] S. H. Rasta, M. E. Partovi, H. Seyedarabi, and A. Javadzadeh, "A comparative study on preprocessing techniques in diabetic retinopathy retinal images: illumination correction and contrast enhancement," *J Med Signals Sens,* vol. 5, pp. 40-8, Jan-Mar 2015.

[191] T. Y. Wong, M. D. Knudtson, R. Klein, B. E. Klein, S. M. Meuer, and L. D. Hubbard, "Computer-assisted measurement of retinal vessel diameters in the Beaver Dam Eye Study: methodology, correlation between eyes, and effect of refractive errors," *Ophthalmology,* vol. 111, pp. 1183-90, Jun 2004.

[192] H. Li, W. Hsu, M. L. Lee, and T. Y. Wong, "Automatic grading of retinal vessel caliber," *IEEE Trans Biomed Eng,* vol. 52, pp. 1352-5, Jul 2005.

[193] X. Benavent, L. Martinez-Costa, G. Ayala, J. Domingo, and P. Marco, "Semi-automated evaluation tool for retinal vasculopathy," *Comput Methods Programs Biomed,* vol. 95, pp. 288-99, Sep 2009.

[194] S. Mahal, W. D. Strain, M. E. Martinez-Perez, S. A. Thom, N. Chaturvedi, and A. D. Hughes, "Comparison of the retinal microvasculature in European and African-Caribbean people with diabetes," *Clin Sci (Lond),* vol. 117, pp. 229-36, Sep 2009.

[195] W. R. Bell, W. R. Green, and M. F. Goldberg, "Histopathologic and trypsin digestion studies of the retina in incontinentia pigmenti," *Ophthalmology,* vol. 115, pp. 893-7, May 2008.

[196] R. P. Danis and I. H. Wallow, "HRP/trypsin technique for studies of the retinal vasculature," *Invest Ophthalmol Vis Sci,* vol. 27, pp. 434-7, Mar 1986.

[197] J. C. Chou, S. D. Rollins, and A. A. Fawzi, "Trypsin digest protocol to analyze the retinal vasculature of a mouse model," *J Vis Exp,* p. e50489, 2013.

[198] I. N. Mohamed, S. A. Soliman, A. Alhusban, S. Matragoon, B. A. Pillai, A. A. Elmarkaby, *et al.*, "Diabetes exacerbates retinal oxidative stress, inflammation, and microvascular degeneration in spontaneously hypertensive rats," *Molecular Vision,* vol. 18, pp. 1457-1466, Jun 2 2012.

[199] A. M. Joussen, T. Murata, A. Tsujikawa, B. Kirchhof, S. E. Bursell, and A. P. Adamis, "Leukocyte-mediated endothelial cell injury and death in the diabetic retina," *Am J Pathol,* vol. 158, pp. 147-52, Jan 2001.

[200] R. Klein, B. E. Klein, S. E. Moss, T. Y. Wong, L. Hubbard, K. J. Cruickshanks, *et al.*, "The relation of retinal vessel caliber to the incidence and progression of diabetic retinopathy: XIX: the Wisconsin Epidemiologic Study of Diabetic Retinopathy," *Arch Ophthalmol,* vol. 122, pp. 76-83, Jan 2004.

[201] T. S. Kern, J. Tang, and B. A. Berkowitz, "Validation of structural and functional lesions of diabetic retinopathy in mice," *Molecular Vision,* vol. 16, pp. 2121-2131, Oct 19 2010.

[202] D. J. Veis, C. M. Sorenson, J. R. Shutter, and S. J. Korsmeyer, "Bcl-2-Deficient Mice Demonstrate Fulminant Lymphoid Apoptosis, Polycystic Kidneys, and Hypopigmented Hair," *Cell,* vol. 75, pp. 229-240, Oct 22 1993.

[203] S. Wang, Z. Wu, C. M. Sorenson, J. Lawler, and N. Sheibani, "Thrombospondin-1-deficient mice exhibit increased vascular density during retinal vascular development and are less sensitive to hyperoxia-mediated vessel obliteration," *Developmental Dynamics,* vol. 228, pp. 630-42, Dec 2003.

[204] J. St-Pierre, J. A. Buckingham, S. J. Roebuck, and M. D. Brand, "Topology of superoxide production from different sites in the mitochondrial electron transport chain," *Journal of Biological Chemistry,* vol. 277, pp. 44784-44790, Nov 22 2002.

[205] T. F. Chan and L. A. Vese, "Active contours without edges," *Ieee Transactions on Image Processing,* vol. 10, pp. 266-277, Feb 2001.

[206] L. A. Vese and T. F. Chan, "A multiphase level set framework for image segmentation using the Mumford and Shah model," *International Journal of Computer Vision,* vol. 50, pp. 271-293, Dec 2002.

[207] J. H. Price, E. A. Hunter, and D. A. Gough, "Accuracy of least squares designed spatial FIR filters for segmentation of images of fluorescence stained cell nuclei," *Cytometry,* vol. 25, pp. 303-16, Dec 1 1996.

[208] Zahra Ghanian, Kevin Staniszewski, Christine M. Sorenson, Nader Sheibani, and M. Ranji, "Cytometric analysis of retinopathies in retinal trypsin digests," in *SPIE Proceeding,* 2014.

[209] N. Otsu, "A threshold selection method from gray-level histograms.," *IEEE Transactions on Systems, Man, and Cybernetics* vol. 9, 1979.

[210] G. S. Jung and R. H. Park, "Automatic Edge Extraction Using Locally Adaptive Threshold," *Electronics Letters,* vol. 24, pp. 711-712, May 26 1988.

[211] L. Lam, S.-W. Lee, and C. Y. Suen, "Thinning Methodologies-A Comprehensive Survey," *IEEE Trans. Pattern Anal. Mach. Intell.,* vol. 14, pp. 869-885, 1992.

[212] Z. K. Huang and K. W. Chau, "A new image thresholding method based on Gaussian mixture model," *Applied Mathematics and Computation,* vol. 205, pp. 899-907, Nov 15 2008.

[213] M. J. Kirkby, *The fractal geometry of nature. Benoit B. Mandelbrot. W. H. Freeman and co., San Francisco, 1982. No. of pages: 460.* vol. 8: John Wiley & Sons, Ltd, 1983.

[214] H. Bittner, P. Wlczek, and M. Sernetz, "Characterization of fractal biological objects by image analysis," *Acta Stereol,* vol. 8, pp. 31-40, 1989.

[215] N. Sarkar and B. B. Chaudhuri, "An Efficient Differential Box-Counting Approach to Compute Fractal Dimension of Image," *Ieee Transactions on Systems Man and Cybernetics,* vol. 24, pp. 115-120, Jan 1994.

[216] B. Mandelbrot, "An Original Method for Spot Detection and Analysis for Large Surveys of Videos in JET," *American Association for the Advancement of Science,* vol. 156, pp. 636-638, May 1967.

[217] C. Cortes and V. Vapnik, "Support-Vector Networks," *Machine Learning,* vol. 20, pp. 273-297, Sep 1995.

[218] R. Kohavi, "A Study of Cross-Validation and Bootstrap for Accuracy Estimation and Model Selection," in *International Joint Conference on Articial Intelligence (IJCAI),* San Mateo, CA: Morgan Kaufmann, 1995, pp. 1137–1143.

[219] L. P. Coelho, A. Shariff, and R. F. Murphy, "Nuclear Segmentation in Microscope Cell Images: A Hand-Segmented Dataset and Comparison of Algorithms," *Proc IEEE Int Symp Biomed Imaging,* vol. 5193098, pp. 518-521, 2009.

[220] Y. Al-Kofahi, W. Lassoued, W. Lee, and B. Roysam, "Improved Automatic Detection and Segmentation of Cell Nuclei in Histopathology Images," *Ieee Transactions on Biomedical Engineering,* vol. 57, pp. 841-852, Apr 2010.

[221] R. L. Engerman and T. S. Kern, "Retinopathy in Animal-Models of Diabetes," *Diabetes-Metabolism Reviews,* vol. 11, pp. 109-120, Jul 1995.

[222] M. Mizutani, T. S. Kern, and M. Lorenzi, "Accelerated death of retinal microvascular cells in human and experimental diabetic retinopathy," *Journal of Clinical Investigation,* vol. 97, pp. 2883-2890, Jun 15 1996.

[223] T. Sugiyama, M. Kobayashi, H. Kawamura, Q. Li, and D. G. Puro, "Enhancement of P2X(7)-induced pore formation and apoptosis: an early effect of diabetes on the retinal microvasculature," *Invest Ophthalmol Vis Sci,* vol. 45, pp. 1026-32, Mar 2004.

[224] T. S. Kern, J. Tang, M. Mizutani, R. A. Kowluru, R. H. Nagaraj, G. Romeo, *et al.*, "Response of capillary cell death to aminoguanidine predicts the development of retinopathy: Comparison of diabetes and galactosemia," *Investigative Ophthalmology & Visual Science,* vol. 41, pp. 3972-3978, Nov 2000.

[225] A. M. Joussen, V. Poulaki, N. Mitsiades, W. Y. Cai, I. Suzuma, J. Pak, *et al.*, "Suppression of Fas-FasL-induced endothelial cell apoptosis prevents diabetic blood-retinal barrier breakdown in a model of streptozotocin-induced diabetes," *FASEB J,* vol. 17, pp. 76-8, Jan 2003.

[226] K. Shimizu, Y. Kobayashi, and K. Muraoka, "Midperipheral fundus involvement in diabetic retinopathy," *Ophthalmology,* vol. 88, pp. 601-12, Jul 1981.

[227] A. J. Barber, D. A. Antonetti, T. S. Kern, C. E. N. Reiter, R. S. Soans, J. K. Krady, *et al.*, "The Ins2(Akita) mouse as a model of early retinal complications in diabetes," *Investigative Ophthalmology & Visual Science,* vol. 46, pp. 2210-2218, Jun 2005.

[228] R. A. Feit-Leichman, R. Kinouchi, M. Takeda, Z. G. Fan, S. Mohr, T. S. Kern, *et al.*, "Vascular damage in a mouse model of diabetic retinopathy: Relation to neuronal and glial changes," *Investigative Ophthalmology & Visual Science,* vol. 46, pp. 4281-4287, Nov 2005.

[229] E. Midena, T. Segato, S. Radin, G. Digiorgio, F. Meneghini, S. Piermarocchi, *et al.*, "Studies on the Retina of the Diabetic Db/Db Mouse .1. Endothelial Cell-Pericyte Ratio," *Ophthalmic Research,* vol. 21, pp. 106-111, Mar-Apr 1989.

[230] W. Y. Li, M. Yanoff, X. P. Liu, and X. D. Ye, "Retinal capillary pericyte apoptosis in early human diabetic retinopathy," *Chinese Medical Journal,* vol. 110, pp. 659-663, Sep 1997.

[231] F. Family, B. R. Masters, and D. E. Platt, "Fractal Pattern-Formation in Human Retinal-Vessels," *Physica D,* vol. 38, pp. 98-103, Sep 1989.

[232] N. Cheung, K. C. Donaghue, G. Liew, S. L. Rogers, J. J. Wang, S. W. Lim, *et al.*, "Quantitative Assessment of Early Diabetic Retinopathy Using Fractal Analysis," *Diabetes Care,* vol. 32, pp. 106-110

226, Jan 2009.

[233] S. W. Lim, N. Cheung, J. J. Wang, K. C. Donaghue, G. Liew, F. M. Islam, *et al.*, "Retinal vascular fractal dimension and risk of early diabetic retinopathy: A prospective study of children and adolescents with type 1 diabetes," *Diabetes Care,* vol. 32, pp. 2081-3, Nov 2009.

[234] A. C. B. Kunicki, A. J. Oliveira, M. B. M. Mendonca, C. T. F. Barbosa, and R. A. Nogueira, "Can the fractal dimension be applied for the early diagnosis of non-proliferative diabetic retinopathy?," *Brazilian Journal of Medical and Biological Research,* vol. 42, pp. 930-934, Oct 2009.

[235] M. Kanwar, P. S. Chan, T. S. Kern, and R. A. Kowluru, "Oxidative damage in the retinal mitochondria of diabetic mice: Possible protection by superoxide dismutase," *Investigative Ophthalmology & Visual Science,* vol. 48, pp. 3805-3811, Aug 2007.

[236] J. F. Turrens, "Mitochondrial formation of reactive oxygen species," *Journal of Physiology-London,* vol. 552, pp. 335-344, Oct 15 2003.

[237] A. P. West, G. S. Shadel, and S. Ghosh, "Mitochondria in innate immune responses," *Nat Rev Immunol,* vol. 11, pp. 389-402, Jun 2011.

[238] B. Chance, H. Sies, and A. Boveris, "Hydroperoxide metabolism in mammalian organs," *Physiol Rev,* vol. 59, pp. 527-605, Jul 1979.

[239] D. F. Stowe and A. K. S. Camara, "Mitochondrial Reactive Oxygen Species Production in Excitable Cells: Modulators of Mitochondrial and Cell Function," *Antioxidants & Redox Signaling,* vol. 11, pp. 1373-1414, Jun 2009.

[240] A. K. S. Camara, E. J. Lesnefsky, and D. F. Stowe, "Potential Therapeutic Benefits of Strategies Directed to Mitochondria," *Antioxidants & Redox Signaling,* vol. 13, pp. 279-347, Aug 2010.

[241] A. K. S. Camara, M. Bienengraeber, and D. F. Stowe, "Mitochondrial approaches to protect against cardiac ischemia and reperfusion injury," *Frontiers in Physiology,* vol. 2, 2011.

[242] P. Mukhopadhyay, M. Rajesh, G. Hasko, B. J. Hawkins, M. Madesh, and P. Pacher, "Simultaneous detection of apoptosis and mitochondrial superoxide production in live cells by flow cytometry and confocal microscopy," *Nat Protoc,* vol. 2, pp. 2295-301, 2007.

[243] K. M. Robinson, M. S. Janes, M. Pehar, J. S. Monette, M. F. Ross, T. M. Hagen, *et al.*, "Selective fluorescent imaging of superoxide in vivo using ethidium-based probes," *Proceedings of the National Academy of Sciences of the United States of America,* vol. 103, pp. 15038-15043, Oct 10 2006.

[244] H. R. Rezvani, N. Ali, A. Taieb, H. de Verneuil, and F. Mazurier, "Hypoxia-inducible factor-1alpha, a key factor in skin physiology and pathophysiology," *Journal of Investigative Dermatology,* vol. 132, pp. S31-S31, May 2012.

[245] M. Pehar, M. R. Vargas, K. M. Robinson, P. Cassina, P. J. Diaz-Amarilla, T. M. Hagen, *et al.*, "Mitochondrial superoxide production and nuclear factor erythroid 2-related factor 2 activation in p75 neurotrophin receptor-induced motor neuron apoptosis," *Journal of Neuroscience,* vol. 27, pp. 7777-7785, Jul 18 2007.

[246] P. Mukhopadhyay, M. Rajesh, K. Yoshihiro, G. Hasko, and P. Pacher, "Simple quantitative detection of mitochondrial superoxide production in live cells," *Biochemical and Biophysical Research Communications,* vol. 358, pp. 203-208, Jun 22 2007.

[247] B. J. Hawkins, M. Madesh, C. J. Kirkpatrick, and A. B. Fisher, "Superoxide flux in endothelial cells via the chloride channel-3 mediates intracellular signaling," *Molecular Biology of the Cell,* vol. 18, pp. 2002-2012, Jun 2007.

[248] A. De Pauw, S. Demine, S. Tejerina, M. Dieu, E. Delaive, A. Kel, *et al.*, "Mild mitochondrial uncoupling does not affect mitochondrial biogenesis but downregulates pyruvate carboxylase in adipocytes: role for triglyceride content reduction," *American Journal of Physiology-Endocrinology and Metabolism,* vol. 302, pp. E1123-E1141, May 2012.

[249] A. Y. Abramov, A. Scorziello, and M. R. Duchen, "Three distinct mechanisms generate oxygen free radicals in neurons and contribute to cell death during anoxia and reoxygenation," *Journal of Neuroscience,* vol. 27, pp. 1129-1138, Jan 31 2007.

[250] M. C. Zimmennan, L. W. Oberley, and S. W. Flanagan, "Mutant SOD1-induced neuronal toxicity is mediated by increased mitochondrial superoxide levels," *Journal of Neurochemistry,* vol. 102, pp. 609-618, Aug 2007.

[251] J. Fauconnier, D. C. Andersson, S. J. Zhang, J. T. Lanner, R. Wibom, A. Katz, *et al.*, "Effects of palmitate on Ca2+ handling in adult control and ob/ob cardiomyocytes," *Diabetes,* vol. 56, pp. 1136-1142, Apr 2007.

[252] A. Iuso, S. Scacco, C. Piccoli, F. Bellomo, V. Petruzzella, R. Trentadue, *et al.*, "Dysfunctions of cellular oxidative metabolism in patients with mutations in the NDUFS1 and NDUFS4 genes of complex I," *Journal of Biological Chemistry,* vol. 281, pp. 10374-10380, Apr 14 2006.

[253] M. Rajesh, P. Mukhopadhyay, S. Batkai, G. Hasko, L. Liaudet, V. R. Drel, *et al.*, "Cannabidiol attenuates high glucose-induced endothelial cell inflammatory response and barrier disruption," *American Journal of Physiology-Heart and Circulatory Physiology,* vol. 293, pp. H610-H619, Jul 2007.

[254] K. C. Lund, L. L. Peterson, and K. B. Wallace, "Absence of a universal mechanism of mitochondrial toxicity by nucleoside analogs," *Antimicrob Agents Chemother,* vol. 51, pp. 2531-9, Jul 2007.

[255] S. Lakshminrusimha, J. A. Russell, R. H. Steinhorn, R. M. Ryan, S. F. Gugino, F. C. Morin, 3rd, *et al.*, "Pulmonary arterial contractility in neonatal lambs increases with 100% oxygen resuscitation," *Pediatric Research,* vol. 59, pp. 137-41, Jan 2006.

[256] R. A. J. Smith, R. C. Hartley, and M. P. Murphy, "Mitochondria-Targeted Small Molecule Therapeutics and Probes," *Antioxidants & Redox Signaling,* vol. 15, pp. 3021-3038, Dec 2011.

[257] K. M. Robinson, M. S. Janes, and J. S. Beckman, "The selective detection of mitochondrial superoxide by live cell imaging," *Nature Protocols,* vol. 3, pp. 941-947, 2008.

[258] Y. B. Liu and D. R. Schubert, "The specificity of neuroprotection by antioxidants," *Journal of Biomedical Science,* vol. 16, Nov 5 2009.

[259] S. Bolte and F. P. Cordelieres, "A guided tour into subcellular colocalization analysis in light microscopy," *Journal of Microscopy-Oxford,* vol. 224, pp. 213-232, Dec 2006.

[260] J. S. Beckman, A. G. Estevez, and J. R. Crow, "Superoxide dismutase and the death of motoneurons in ALS," *Trends in Neurosciences,* vol. 24, pp. S15-S20, Nov 2001.

[261] C. Batandier, E. Fontaine, C. Keriel, and X. M. Leverve, "Determination of mitochondrial reactive oxygen species: methodological aspects," *Journal of Cellular and Molecular Medicine,* vol. 6, pp. 175-187, Apr-Jun 2002.

[262] A. G. Este´ vez, N. Spear, M. Manuel, R. Radi, C. E. Henderson, L. Barbeito, *et al.*, "Nitric Oxide and Superoxide Contribute to Motor Neuron Apoptosis Induced by Trophic Factor Deprivation," *The Journal of Neuroscience,* vol. 18, pp. 923-931, Feb 1998.

[263] A. C. Rego and C. R. Oliveira, "Mitochondrial dysfunction and reactive oxygen species in excitotoxicity and apoptosis: Implications for the pathogenesis of neurodegenerative diseases," *Neurochemical Research,* vol. 28, pp. 1563-1574, Oct 2003.

[264] K. Tieu, H. Ischiropoulos, and S. Przedborski, "Nitric oxide and reactive oxygen species in Parkinson's disease," *Iubmb Life,* vol. 55, pp. 329-335, Jun 2003.

[265] M. Jerkic, M. G. Kabir, A. Davies, L. X. Yu, B. A. S. McIntyre, N. W. Husain, *et al.*, "Pulmonary hypertension in adult Alk1 heterozygous mice due to oxidative stress," *Cardiovascular Research,* vol. 92, pp. 375-384, Dec 1 2011.

[266] F. Seta, M. Rahmani, P. V. Turner, and C. D. Funk, "Pulmonary Oxidative Stress Is Increased in Cyclooxygenase-2 Knockdown Mice with Mild Pulmonary Hypertension Induced by Monocrotaline," *PLoS One,* vol. 6, Aug 5 2011.

[267] R. H. Kallet and M. A. Matthay, "Hyperoxic acute lung injury," *Respir Care,* vol. 58, pp. 123-41, Jan 2013.

[268] V. Bhandari, "Molecular mechanisms of hyperoxia-induced acute lung injury," *Front Biosci,* vol. 13, pp. 6653-61, 2008.

[269] C. Brueckl, S. Kaestle, A. Kerem, H. Habazettl, F. Krombach, H. Kuppe, *et al.*, "Hyperoxia-induced Reactive Oxygen Species Formation in Pulmonary Capillary Endothelial Cells in situ," *Am J Respir Cell Mol Biol,* Dec 15 2005.

[270] A. B. Fisher, H. J. Forman, and M. Glass, "Mechanisms of pulmonary oxygen toxicity," *Lung,* vol. 162, pp. 255-9, 1984.

[271] H. R. Rezvani, S. Dedieu, S. North, F. Belloc, R. Rossignol, T. Letellier, *et al.*, "Hypoxia-inducible factor-1alpha, a key factor in the keratinocyte response to UVB exposure," *J Biol Chem,* vol. 282, pp. 16413-22, Jun 1 2007.

[272] M. Pehar, M. R. Vargas, K. M. Robinson, P. Cassina, P. J. Diaz-Amarilla, T. M. Hagen, *et al.*, "Mitochondrial superoxide production and nuclear factor erythroid 2-related factor 2 activation in p75 neurotrophin receptor-induced motor neuron apoptosis," *J Neurosci,* vol. 27, pp. 7777-85, Jul 18 2007.

[273] L. I. Johnson-Cadwell, M. B. Jekabsons, A. Wang, B. M. Polster, and D. G. Nicholls, "'Mild Uncoupling' does not decrease mitochondrial superoxide levels in cultured cerebellar granule neurons but decreases spare respiratory capacity and increases toxicity to glutamate and oxidative stress," *Journal of Neurochemistry,* vol. 101, pp. 1619-1631, Jun 2007.

[274] M. C. Zimmerman, L. W. Oberley, and S. W. Flanagan, "Mutant SOD1-induced neuronal toxicity is mediated by increased mitochondrial superoxide levels," *Journal of Neurochemistry,* vol. 102, pp. 609-18, Aug 2007.

[275] S. Menazza and E. Murphy, "The Expanding Complexity of Estrogen Receptor Signaling in the Cardiovascular System," *Circulation Research,* vol. 118, pp. 994-1007, Mar 18 2016.

[276] X. Y. Li, P. Fang, J. T. Mai, E. T. Choi, H. Wang, and X. F. Yang, "Targeting mitochondrial reactive oxygen species as novel therapy for inflammatory diseases and cancers," *Journal of Hematology & Oncology,* vol. 6, Feb 25 2013.

[277] M. A. Aon, S. Cortassa, and B. O'Rourke, "Redox-optimized ROS balance: A unifying hypothesis," *Biochimica Et Biophysica Acta-Bioenergetics,* vol. 1797, pp. 865-877, Jun-Jul 2010.

[278] J. F. Turrens, "Mitochondrial formation of reactive oxygen species," *J Physiol,* vol. 552, pp. 335-44, Oct 15 2003.

[279] E. Cadenas, A. Boveris, C. I. Ragan, and A. O. Stoppani, "Production of superoxide radicals and hydrogen peroxide by NADH-ubiquinone reductase and ubiquinol-cytochrome c reductase from beef-heart mitochondria," *Arch Biochem Biophys,* vol. 180, pp. 248-57, Apr 30 1977.

[280] J. F. Turrens, A. Alexandre, and A. L. Lehninger, "Ubisemiquinone is the electron donor for superoxide formation by complex III of heart mitochondria," *Arch Biochem Biophys,* vol. 237, pp. 408-14, Mar 1985.

[281] Y. Liu, G. Fiskum, and D. Schubert, "Generation of reactive oxygen species by the mitochondrial electron transport chain," *Journal of Neurochemistry,* vol. 80, pp. 780-7, Mar 2002.

[282] L. Zhang, L. D. Yu, and C. A. Yu, "Generation of superoxide anion by succinate-cytochrome c reductase from bovine heart mitochondria," *Journal of Biological Chemistry,* vol. 273, pp. 33972-33976, Dec 18 1998.

[283] P. R. Rich and W. D. Bonner, "The sites of superoxide anion generation in higher plant mitochondria," *Arch Biochem Biophys,* vol. 188, pp. 206-13, May 1978.

[284] I. V. Grigolava, M. Ksenzenko, A. A. Konstantinob, A. N. Tikhonov, and T. M. Kerimov, "[Tiron as a spin-trap for superoxide radicals produced by the respiratory chain of submitochondrial particles]," *Biokhimiia,* vol. 45, pp. 75-82, Jan 1980.

[285] Y. J. Wang, Y. S. Ho, S. W. Chu, H. J. Lien, T. H. Liu, and J. K. Lin, "Induction of glutathione depletion, p53 protein accumulation and cellular transformation by tetrachlorohydroquinone, a toxic metabolite of pentachlorophenol (vol 105, pg 1, 1997)," *Chemico-Biological Interactions,* vol. 106, pp. 87-87, Aug 29 1997.

[286] Y. J. Wang, C. C. Lee, W. C. Chang, H. B. Liou, and Y. S. Ho, "Oxidative stress and liver toxicity in rats and human hepatoma cell line induced by pentachlorophenol and its major metabolite tetrachlorohydroquinone," *Toxicol Lett,* vol. 122, pp. 157-69, Jun 20 2001.

[287] W. C. Dorsey, P. B. Tchounwou, and B. D. Ford, "Neuregulin 1-Beta cytoprotective role in AML 12 mouse hepatocytes exposed to pentachlorophenol," *Int J Environ Res Public Health,* vol. 3, pp. 11-22, Mar 2006.

[288] P. Fernandez Freire, V. Labrador, J. M. P. Martin, and M. J. Hazen, "Cytotoxic effects in mammalian Vero cells exposed to pentachlorophenol," *Toxicology,* vol. 210, pp. 37-44, May 15 2005.

[289] J. Folch, M. Yeste-Velasco, D. Alvira, A. V. de la Torre, M. Bordas, M. Lopez, *et al.*, "Evaluation of pathways involved in pentachlorophenol-induced apoptosis in rat neurons," *Neurotoxicology,* vol. 30, pp. 451-458, May 2009.

[290] R. Sepehr, S. H. Audi, K. S. Staniszewski, S. T. Haworth, E. R. Jacobs, and M. Ranji, "Novel Flurometric Tool to Assess Mitochondrial Redox State of Isolated Perfused Rat Lungs after Exposure to Hyperoxia," *IEEE J Transl Eng Health Med,* vol. 1, Oct 16 2013.

[291] Y. L. Dong, P. J. Zhou, S. Y. Jiang, X. W. Pan, and X. H. Zhao, "Induction of oxidative stress and apoptosis by pentachlorophenol in primary cultures of Carassius carassius hepatocytes," *Comparative Biochemistry and Physiology C-Toxicology & Pharmacology,* vol. 150, pp. 179-185, Aug 2009.

[292] J. N. He, Y. Duan, D. P. Hua, G. J. Fan, L. Wang, Y. Liu, *et al.*, "DEXH Box RNA Helicase-Mediated Mitochondrial Reactive Oxygen Species Production in Arabidopsis Mediates Crosstalk between Abscisic Acid and Auxin Signaling," *Plant Cell,* vol. 24, pp. 1815-1833, May 2012.

[293] R. F. Feissner, J. Skalska, W. E. Gaum, and S. S. Sheu, "Crosstalk signaling between mitochondrial Ca2+ and ROS," *Frontiers in Bioscience-Landmark,* vol. 14, pp. 1197-1218, Jan 1 2009.

[294] E. Cadenas and A. Boveris, "Enhancement of hydrogen peroxide formation by protophores and ionophores in antimycin-supplemented mitochondria," *Biochem J,* vol. 188, pp. 31-7, Apr 15 1980.

[295] B. D. Fink, Y. O'Malley, B. L. Dake, N. C. Ross, T. E. Prisinzano, and W. I. Sivitz, "Mitochondrial targeted coenzyme Q, superoxide, and fuel selectivity in endothelial cells," *PLoS One,* vol. 4, p. e4250, 2009.

[296] I. Ali, S. Gruenloh, Y. Gao, A. V. Clough, J. R. Falck, M. Medhora, *et al.*, "Protection by 20-5,14-HEDGE Against Surgically-Induced Ischemia Reperfusion Lung Injury in Rats," *Annals of Thoracic Surgery,* 2011.

[297] T. Kalogeris, Y. M. Bao, and R. J. Korthuis, "Mitochondrial reactive oxygen species: A double edged sword in ischemia/reperfusion vs preconditioning," *Redox Biology,* vol. 2, pp. 702-714, 2014.

[298] M. F. Ross, G. F. Kelso, F. H. Blaikie, A. M. James, H. M. Cocheme, A. Filipovska, *et al.*, "Lipophilic triphenylphosphonium cations as tools in mitochondrial bioenergetics and free radical biology," *Biochemistry-Moscow,* vol. 70, pp. 222-230, Feb 2005.

[299] M. Kalbacova, M. Vrbacky, Z. Drahota, and Z. Melkova, "Comparison of the effect of mitochondrial inhibitors on mitochondrial membrane potential in two different cell lines using flow cytometry and spectrofluorometry," *Cytometry A,* vol. 52, pp. 110-6, Apr 2003.

[300] A. R. Khaled, D. A. Reynolds, H. A. Young, C. B. Thompson, K. Muegge, and S. K. Durum, "Interleukin-3 withdrawal induces an early increase in mitochondrial membrane potential unrelated to the Bcl-2 fammily - Roles of intracellular pH, ADP transport, and F0F1-ATPase," *Journal of Biological Chemistry,* vol. 276, pp. 6453-6462, Mar 2 2001.

[301] F. M. P. de Gannes, M. A. Belaud-Rotureau, P. Voisin, N. Leducq, F. Belloc, P. Canioni, *et al.*, "Flow cytometric analysis of mitochondrial activity in situ: Application to acetylceramide-induced mitochondrial swelling and apoptosis," *Cytometry,* vol. 33, pp. 333-339, Nov 1 1998.

[302] "National Vital Statistics Report. Deaths: Final Data for 2009.," *Centers for Disease Control and Prevention. National Center for Health Statistics.,* vol. 60, 2012.

[303] R. Lozano, M. Naghavi, K. Foreman, S. Lim, K. Shibuya, V. Aboyans, *et al.*, "Global and regional mortality from 235 causes of death for 20 age groups in 1990 and 2010: a systematic analysis for the Global Burden of Disease Study 2010," *Lancet,* vol. 380, pp. 2095-128, Dec 15 2012.

[304] R. S. Mascaretti, M. M. G. B. Mataloun, M. Dolhnikoff, and C. M. Rebello, "Lung Morphometry, Collagen and Elastin Content: Changes after Hyperoxic Exposure in Preterm Rabbits," *Clinics,* vol. 64, pp. 1099-1104, 2009.

[305] S. H. Audi, M. P. Merker, G. S. Krenz, T. Ahuja, D. L. Roerig, and R. D. Bongard, "Coenzyme Q1 redox metabolism during passage through the rat pulmonary circulation and the effect of hyperoxia," *J Appl Physiol,* vol. 105, pp. 1114-26, Oct 2008.

[306] W. S. Kunz and F. N. Gellerich, "Quantification of the content of fluorescent flavoproteins in mitochondria from liver, kidney cortex, skeletal muscle, and brain," *Biochemical medicine and metabolic biology,* vol. 50, pp. 103-10, Aug 1993.

[307] H. H. Webb and D. F. Tierney, "Experimental pulmonary edema due to intermittent positive pressure ventilation with high inflation pressures. Protection by positive end-expiratory pressure," *Am Rev Respir Dis,* vol. 110, pp. 556-65, Nov 1974.

[308] N. de Prost, J. D. Ricard, G. Saumon, and D. Dreyfuss, "Ventilator-induced lung injury: historical perspectives and clinical implications," *Ann Intensive Care,* vol. 1, p. 28, 2011.

[309] S. Arslan, T. Ersahin, R. Cetin-Atalay, and C. Gunduz-Demir, "Attributed relational graphs for cell nucleus segmentation in fluorescence microscopy images," *IEEE Trans Med Imaging,* vol. 32, pp. 1121-31, Jun 2013.

[310] T. Craciunescu, A. Murari, B. Sieglin, G. Matthews, and J. E. Contributors, "An Original Method for Spot Detection and Analysis for Large Surveys of Videos in JET," *IEEE TRANSACTIONS ON PLASMA SCIENCE,* vol. 42, pp. 1358-1366, May 2014.

[311] S. C. Pei and J. H. Horng, "Design of FIR bilevel Laplacian-of-Gaussian filter," *Signal Processing,* vol. 82, pp. 677-691, Apr 2002.

[312] F. Meyer and S. Beucher, "Morphological Segmentation," *Journal of Visual Communication and Image Representation,* vol. 1, pp. 21-46, September 1990.

[313] E. Preteux, "Watershed and skeleton by influence zones: A distance-based approach," *Journal of Mathematical Imaging and Vision,* vol. 1, pp. 239-255, 1992/09/01 1992.

[314] N. Otsu, "A Threshold Selection Method from Gray-Level Histograms," *IEEE Transactions on Systems, Man, and Cybernetics,* vol. 9, pp. 62-66, 1979.

[315] M. Ranji, Z. Ghanian, F. Atry, S. Frye, R. Pashaie, and S. Audi, "Optical Instrumentation and the Image Cytometry of Lung and Eye Injuries: Studies in the Rodent Model," in *Biomedical Optics 2014,* Miami, Florida, 2014, p. BT3A.58.

[316] J. W. Reed, C. Elliott, and E. Thorsen, "Increased lung compliance in response to a moderate hyperoxic exposure," *Undersea & Hyperbaric Medicine,* vol. 28, pp. 19-23, Spr 2001.

Appendix

Curriculum Vitae

7. Appendix: Curriculum Vitae

Education and Qualification

Ph.D., University of Wisconsin-Milwaukee September 2011-present, expected Dec 2016
Biomedical/Electrical Engineering Department GPA 4/4
Dissertation: "Quantitative Optical Studies of Oxidative Stress in Rodent Models of Retina and Lung Injuries"

Amirkabir University of Technology (Tehran Polytechnic), Tehran, Iran September 1998-May 2001
M.Sc. in RF Telecommunication Engineering, Electrical Engineering Department GPA 3.7/4 (first rank)
Thesis: "Design, Analysis and Implementation of Frequency Synthesizer at S-band"

Sharif University of Technology, Tehran, Iran Sept. 1994- Sept. 1998
B.Sc. in Telecommunication Engineering, Electrical Engineering Department GPA 3.4/4
Thesis: "Design and Implementation of 32kb/s ADPCM CODEC based on 64kb/s PCM CODEC in point to point digital radio transmission"

Research Interests

- Biophotonics, optical imaging, metabolic imaging
- Signal processing
- Image processing, structure identification, feature selection, quantification and classification
- Image segmentation and visualization
- Pattern recognition and machine learning techniques
- Biomedical imaging, medical instrumentation (Ultrasounds)
- RF, microwave and optics
- Wireless Circuit and System Design and Implementation

Software and Technical Proficiencies

- Engineering and statistics software: MATLAB, and Simulink, C++, Pspice, Protel (PCB design), Zemax, R
- Image and spectrum analysis software: Imaris, ImageJ, OPUS, Igor pro, IRidys
- Application programs: MS Office, Visio, HTML
- FPGA design and programming software: ModelSim, Altera Quartus, Eclips, SoC EDS
- RF and microwave software: Microwave Office, HP Series IV, CST Microwave STUDIO
- Spectrum and Network Analysis
- Biomedical instrumentation, imaging and image processing
- Fluorescence Microscopy, Spectroscopy, and Cryoimaging
- FTIR Microscopy, Spectroscopy, and Hyper Spectral Image Analysis
- Wireless Circuit and System Design and Implementation

Professional Experiences

Research Assistant, Biophotonics Lab, University of Wisconsin-Milwaukee **Sept. 2011-Present**
Research Project: Development of optical imaging and image processing techniques for medical diagnostics

- *Ex vivo* studies of structural changes in injured lung tissue, using SD-OCT and developing a segmentation algorithm to quantify changes in alveolar properties at different conditions for different injuries
- *In vitro* studies of cellular ROS (Reactive Oxygen Species) dynamics using fluorescence time lapse microscopy and developing a protocol to quantify changes of oxidative stress level in live cells
- Implementing image cytometry software to quantify retinopathy using fluorescence microscopy and morphometric angiogenesis parameters. Image cytometry tool is capable of segmenting vascular cells, and calculating vasculature features including: area, caliber, branch points, fractal dimension, and acellular capillaries, and classifying the healthy and injured retina

- Fluorescent imaging of NADH and FAD in cryogenic temperatures and developing image processing algorithm to evaluate tissue injuries and metabolic redox state in the tissue 3D volume quantitatively and statistically
- Design and implementation cryoimager: low temperature fluorescence imager as a system to monitor metabolism of tissue

Course Instructor, Analytical Methods in Engineering (EE234), UW-Milwaukee **2015-2016**

Teaching Assistant, Fourier Optics (EE765), University of Wisconsin-Milwaukee **Spring 2013**

Design Engineer, RSA Electronics**,** Tehran, Iran **Nov. 2009- August 2011**

Project : Design and implementation of Smart Energy and Water Meters (SEWM) and optimization of the design in order to pass the EMC/EMI standard tests.

Design Engineer and Project Manager, NRI (Niroo Research Institute), Tehran, Iran October 2002-October 2009

Project : Design and implementation of Radio MODEM,

- Design and implementation of FHSS (Frequency Hopping Spread Spectrum) MODEM
- Design and implementation of wideband and low phase noise synthesizer for DVBT application
- Design and implementation of 4.4-5GHz point to point Radio link
- Lecturer, NRI (Niroo Research Institute), Tehran, Iran October 2004-October 2006
  Courses: fiber optics, radio network design

Researcher, ITRC (Iran Telecommunications Research Center), Tehran, Iran **May 2001- Sept. 2002**

Research Assistant, Microwave/mm-wave and Wireless Communications Research Laboratory, Tehran Polytechnic

Projects : Design and implementation of MMIC chipset for Ka band LMDS (Local Multipoint Distribution System)

- Nonlinear design methodology and simulation of microwave distributed amplifiers compatible with MMIC technology for mm-wave frequencies application
- Design and nonlinear analysis of MMIC power amplifier for LMDS applications at Ka-band

Research Assistant, Advanced Research Laboratory, Tehran Polytechnic, Tehran, Iran **June 1999- May 2001**

Projects: Design, analysis and implementation of frequency synthesizer at S-band

- Design, nonlinear analysis and fabrication of VCO at S-band
- Study of "Noise and spurious responses in phase locked loop"

Teacher, high school, Tehran, Iran June 1996- May 1998

Courses: Mathematics, linear algebra, trigonometry, solid geometry

Publication

Journal Papers

J1) Zahra Ghanian, Annie Eis, Ganesh Kondouri, and Mahsa Ranji," Optical Studies of Oxidative Stress in Persistent Pulmonary Hypertension of the Newborn", submitted to American Journal of Physiology Lung Cellular and Molecular Physiolgy.

J2) Zahra Ghanian, Annie Eis, Ganesh Kondouri, and Mahsa Ranji," Quantitative Optical Studies of Oxidative Stress in Pulmonary Artery Endothelial Cells", submitted to Biophysical Journal.

J3) Zahra Ghanian, Kevin Staniszewski, Christine M. Sorenson, Nader Sheibani, and Mahsa Ranji," Quantitative assessment of retinopathy using multi-parameter image analysis", Journal of Medical Signals and Sensors, Vol. 6, No. 2, April 2016.

J4) Fahimeh Salehpour, Zahra Ghanian, Chun Yang, Nadezhda Zheleznova, Theresa Kurth, Ranjan Dash, Allen Cowley, Mahsa Ranji, " Effects of p67phox on the mitochondrial oxidative state in the kidney of Dahl salt-

sensitive rats: optical fluorescence 3-D cryoimaging", American Journal of Physiology-Renal Physiology, Vol. 309, No. 4, August 2015.

J5) Zahra Ghanian, Sepideh Maleki, Hannah Reiland, Daniel E Butz, Grazia Chiellini, Fariba Assadi-Porter, and Mahsa Ranji, "Optical imaging of mitochondrial redox state in rodent models with 3-iodothyronamine", Journal of Experimental Biology and Medicine, Vol. 239, No. 2, February 2014.

J6) Zahra Ghanian, S. Maleki, C.M. Sorenson, N. Sheibani and M. Ranji, "Optical Imaging of Mitochondrial Redox State in Rodent Model of Hereditary Hemorrhagic Telangiectasia-1 (HHT1)", Journal of Biophotonics, Vol. 7, No. 10, October 2014.

J7) Sepideh Maleki, Sandeep Gopalakrishnan, Zahra Ghanian, Reyhaneh Sepehr, Heather Schmitt, Janis Eells, Mahsa Ranji, "Optical Imaging of Mitochondrial Redox State in Rodent Model of Retinitis Pigmentosa ", J Biomed Opt, Dec 13 2012.

J8) Zahra Ghanian, A. Abdipour, A. Ghorbani, "Nonlinear Analysis, Design and Implementation of a VCO in S Frequency Band", Springer Journal on Analog Integrated Circuits and Signal Processing Volume 49, Number 2, Pages: 213- 223. http://www.springerlink.com/content/t62457508484/, October 2006.

J9) Zahra Ghanian, A. Abdipour and M. Hakkak, "Design, Graphical Optimization and Nonlinear Analysis of Power Amplifier in Ka Frequency Band", Science-Research Journal of Modarres, No.7, Pages: 35-51, May 2002.

Conference Papers

C1) Zahra Ghanian, Ganesh Kondouri, and Mahsa Ranji, " Time lapse fluorescence microscopy of Reactive Oxygen Species (ROS) performed in vitro demonstrates a major role for complex IV in ROS generation ", BMES Southeast Conference, October 23, 2015.

C2) Zahra Ghanian, Ganesh Kondouri, and Mahsa Ranji, "Time lapse microscopy of oxidative stress in lung endothelial cells", Proc. SPIE 9531-3, May 25, 2015.

C3) Zahra Ghanian, Ganesh Kondouri, and Mahsa Ranji, "Optical Studies of Oxidative Stress in Persistent Pulmonary Hypertension Cells", OSA, April 2, 2015.

C4) Zahra Ghanian, Annie Eis, Ganesh Kondouri, and Mahsa Ranji, "Optical Studies of Oxidative Stress in Pulmonary Artery Endothelial Cells", Proc. SPIE 9328, Imaging, Manipulation, and Analysis of Biomolecules, Cells, and Tissues XIII, 932807, March 2, 2015.

C5) Mahsa Ranji, Zahra Ghanian, Farid Atry, Seth Frye, Ramin Pashaei, and Said Audi, "Optical instrumentation and Image Cytometry of Lung and Eye Injuries: Studies in the Rodent Model", Proc. Biomedical Optics, http://dx.doi.org/10.1364/BIOMED.2014.BT3A.58, Miami, Florida, April 2014.

C6) Zahra Ghanian, Kevin Staniszewski, Christine M. Sorenson, Nader Sheibani, and Mahsa Ranji, " Cytometric Analysis of Retinopathies in Retinal Trypsin Digests", Proc. SPIE. 8947, Imaging, Manipulation, and Analysis of Biomolecules, Cells, and Tissues XII, 89471Y., March 04, 2014.

C7) Micheal Rogowski, Ebru Selen, Zahra Ghanian, S. Maleki, Z. Bolandnazar, F. Assadi-Porter, M. Ranji, "Metabolomics and optical imaging show tissue specific mitochondrial oxidative stress as early biomarkers of polycistic ovary syndrome," 5th Texas Tech Annual Biological Sciences Symposium (TTABSS), Texas, March 2014.

C8) Zahra Ghanian, M. MasoudiMotlagh, S. Maleki, Z. Bolandnazar, F. Assadi-Porter, M. Ranji," Optical Redox Imaging of Metabolic Dysfunction in Polycystic Ovary Syndrome," BMES Annual conference, Seattle, Oct 2013.

C9) Zahra Ghanian, C.M. Sorenson, N. Sheibani, M. Ranji," Optical Imaging of Cellular Redox State Related to Retinopathy Dysfunction in Endoglin Heterozygous (Eng+/-) Mice," UWM CEAS Research Day, April 2013.

C10) Zahra Ghanian, C.M. Sorenson, N. Sheibani and M. Ranji, "Optical Imaging of Cellular Redox State in Endoglin Heterozygous (Eng+/-) Mice", IEEE Sponsored Conferences & Symposia, Feb 2013.

C11) Zahra Ghanian, S. Maleki, S. Golpalakrishnan, R. Sepehr, J. Eells, M. Ranji, " Optical Imaging of Oxidative Stress in Retinitis Pigmentosa (RP) in Rodent Model", Proc. SPIE 8591, Optical Diagnostics and Sensing XIII: Toward Point-of-Care Diagnostics, 85910S, February 25, 2013.

C12) Zahra Ghanian, Christine Sorenson, Nader Sheibani, M. Ranji, "Optical Imaging of Oxidative Stress in Diabetic Retinopathy", BMES Oct 2012.

C13) Zahra Ghanian, "Synchronization in Frequency Hopping Spread Spectrum Systems", IPSC2004 19th International Power System Conference, Tehran, Iran. http://www.civilica.com/Paper-PSC19-PSC19_032.html, November 2004.

Honors/Awards

- Recipient of distinguished dissertation fellowship at UW-Milwaukee (campus-wide competition), 2015 - 2016
- Featured in UWM Research Report, 2014 (page11)
- Featured in Milwaukee Engineer Journal, spring 2014 (page 7)
- Ranked 1st in the PhD qualifying exam, electrical engineering, university of Wisconsin Milwaukee, 2012
- Recipient of UWM travel award to present at a leading optics conference, 2013-2015
- Chancellor's Graduate Student Award for outstanding academic achievement, 2011, 2012, 2015, and 2016
- Ranked 1st among graduate students of the Telecommunication Engineering, Electrical Engineering Department, Amirkabir University of Technology (Tehran Polytechnic), Tehran, Iran,2001
- Ranked 82th among the 350,000 participants in the nationwide 'Universities Entrance Exam', 1994
- Accepted to the first stage of Physics & Mathematics Olympiads in Iran, 1993